

## **INFORMATION TO USERS**

This manuscript has been reproduced from the microfilm master. UMI films the text directly from the original or copy submitted. Thus, some thesis and dissertation copies are in typewriter face, while others may be from any type of computer printer.

The quality of this reproduction is dependent upon the quality of the copy submitted. Broken or indistinct print, colored or poor quality illustrations and photographs, print bleedthrough, substandard margins, and improper alignment can adversely affect reproduction.

In the unlikely event that the author did not send UMI a complete manuscript and there are missing pages, these will be noted. Also, if unauthorized copyright material had to be removed, a note will indicate the deletion.

Oversize materials (e.g., maps, drawings, charts) are reproduced by sectioning the original, beginning at the upper left-hand corner and continuing from left to right in equal sections with small overlaps.

Photographs included in the original manuscript have been reproduced xerographically in this copy. Higher quality 6" x 9" black and white photographic prints are available for any photographs or illustrations appearing in this copy for an additional charge. Contact UMI directly to order.

**ProQuest Information and Learning  
300 North Zeeb Road, Ann Arbor, MI 48106-1346 USA  
800-521-0600**

**UMI<sup>®</sup>**



Study of Lambda Production  
in Au+Au Collisions at 11.5 A·GeV/c

by

Yujin Qi

A thesis submitted  
to the Faculty of Graduate Studies and Research  
in partial fulfillment of the requirements  
of the degree of

Doctor of Philosophy  
in Physics

Department of Physics  
McGill University, Montréal, Canada.  
©Yujin Qi, August 1999



National Library  
of Canada

Acquisitions and  
Bibliographic Services

395 Wellington Street  
Ottawa ON K1A 0N4  
Canada

Bibliothèque nationale  
du Canada

Acquisitions et  
services bibliographiques

395, rue Wellington  
Ottawa ON K1A 0N4  
Canada

*Your file* *Votre référence*

*Our file* *Notre référence*

The author has granted a non-exclusive licence allowing the National Library of Canada to reproduce, loan, distribute or sell copies of this thesis in microform, paper or electronic formats.

The author retains ownership of the copyright in this thesis. Neither the thesis nor substantial extracts from it may be printed or otherwise reproduced without the author's permission.

L'auteur a accordé une licence non exclusive permettant à la Bibliothèque nationale du Canada de reproduire, prêter, distribuer ou vendre des copies de cette thèse sous la forme de microfiche/film, de reproduction sur papier ou sur format électronique.

L'auteur conserve la propriété du droit d'auteur qui protège cette thèse. Ni la thèse ni des extraits substantiels de celle-ci ne doivent être imprimés ou autrement reproduits sans son autorisation.

0-612-64648-3

**Canada**

**Dedicated to my family...**

# Abstract

Lambda production in central Au+Au collisions at 11.5 A·GeV/c has been studied at forward rapidities ( $y > 2.2$ ) using the upgraded E877 experimental setup at the AGS. Lambdas are measured via the charged decay channel:  $\Lambda \rightarrow p\pi^-$  and identified from the  $p\pi^-$  invariant mass spectra with the aids of a set of pair cuts. A comprehensive Monte Carlo simulation is made to extensively study the lambda reconstruction. The details of the data analysis for lambda identification are presented. The consistence of data analysis is examined by detailed comparison of the constructed proton and pion spectra with the previous results from the E877 1993 data set. The double differential multiplicities for lambda as a function of collision centrality are presented. Lambda rapidity distribution  $dN/dy$  is also studied. A pure thermal model is used to characterize the lambda spectra. The experimental results are compared to the predictions of the RQMD model (v2.3) in its cascade version and in the mode that takes into account the effect of mean-field. We also present the first measurement of the lambda directed flow at the AGS. In spite of limited statistics, a strong positive directed flow for lambda, which is comparable to the amplitude of the proton flow, is observed at forward rapidities ( $2.8 < y < 3.4$ ) in the semi-central Au+Au collisions. The measured flow amplitude as a function of  $p_t$ ,  $v_1(p_t)$ , is in agreement with the predictions of the RQMD model.

# Résumé

La production des particules lambdas dans les collisions centrales d'Au+Au à 11.5 A·GeV/c a été étudiée aux rapidités avants ( $y > 2.2$ ) utilisant l'installation expérimentale E877 à l'AGS. Les lambdas sont mesurées par l'intermédiaire de la voie de désintégration chargée:  $\Lambda \rightarrow p\pi^-$  et identifiés grâce au spectre de masse invariante des paires ( $p, \pi^-$ ) après l'imposition d'un ensemble de conditions sur les paires afin de réduire le fond statistique. L'efficacité et l'acceptance pour la reconstruction des lambdas est étudiées par simulation Monte Carlo. La consistance de l'analyse des données est évaluée par une comparaison détaillée des spectres inclusifs de protons et de mésons pi avec les résultats obtenus précédemment par l'expérience E877 à partir des données recueillies en 1993. Les doubles multiplicités différentielles des lambdas en fonction de la centralité des collisions sont présentées. Le taux de production des lambdas en fonction de la rapidité,  $dN/dy$ , est également présentée. Un modèle thermique est employé pour caractériser les données. Les résultats obtenus sont comparés aux prévisions du modèle RQMD (v2.3) dans sa version cascade pure et en tenant compte de l'effet du champ moyen. Nous présentons la première mesure du flot transverse des lambdas à l'AGS. Malgré une statistique limitée, on observe un flot positif important comparable à l'amplitude du flot transverse observée pour les protons dans la même réaction. La dépendance du flot en fonction du moment transverse,  $v_1(p_t)$ , est en accord avec les prévisions du modèle RQMD.

# Statement of Originality

In this thesis, I have studied in detail the lambda production and the lambda directed flow at forward rapidities ( $y > 2.2$ ) in Au+Au collisions at energy of 11.5 GeV per nucleon. The data analyzed in this thesis are from the 1995 run of the E877 experiment at the Alternating Gradient Synchrotron (AGS) of the Brookhaven National Laboratory. Lambda hyperons are measured via their charged decay products — proton and negative pion pairs.

Due to the low abundance of lambda production and the limited acceptance of the E877 spectrometer, the measurement and identification of lambda hyperons are challenging and require carefully analysis. In this thesis, I have developed an effective algorithm to identify the lambda hyperons from the large background environment. This algorithm includes a comprehensive Monte Carlo kinematic simulation to study the detailed features for the lambda identification and the main corrections that allow to obtain the lambda spectra. In order to establish the validity of our data analysis, I also construct the proton and pion spectra with high statistics and perform a detailed comparison to the previous results from the E877 1993 data set.

I have studied the lambda production in terms of the double differential multiplicity distribution as a function of the collision centrality. It shows that the general features of the lambda spectra are well characterized by a pure thermal model. The rapidity distribution  $dN/dy$  is obtained from an integration of the transverse mass

I have compared the results on lambda production to the predictions of the RQMD model (v2.3) in its cascade version and also in the mode that includes the effects of mean-field. A good agreement is obtained in the measured rapidity range.

The study of lambda directed flow has been performed for the first time at the AGS. As a principal result, a strong positive directed flow of the lambdas has been clearly observed at forward rapidities ( $2.8 < y < 3.4$ ) in the semi-central Au+Au collisions. It is shown that the flow amplitude for lambdas is comparable to that of the protons in the same acceptance range. The observed transverse momentum ( $p_t$ ) dependence of the flow amplitude ( $v_1$ ) for lambda is also in agreement with the predictions of the RQMD model with a better description for the cascade mode calculations. This data provide a valuable information in the study of the medium effects of the strange particles in dense nuclear matter at the AGS energies.

# Contents

<b>1</b>	<b>Introduction</b>	<b>1</b>
<b>2</b>	<b>Physics Issues</b>	<b>6</b>
2.1	Relativistic Heavy-Ion Collisions . . . . .	7
2.1.1	General Features . . . . .	7
2.1.2	Kinematic Variables . . . . .	10
2.1.3	Space-Time Evolution of RHI Collisions . . . . .	12
2.2	Nuclear Stopping Power . . . . .	13
2.3	Phenomenology of Hadron Production . . . . .	16
2.3.1	Fireball Model . . . . .	16
2.3.2	Radial Flow . . . . .	18
2.3.3	Azimuthally Anisotropic Flow . . . . .	22
2.3.4	Hadron Yields and Strangeness . . . . .	26
2.4	Lambda Production . . . . .	29
<b>3</b>	<b>Experimental Setup</b>	<b>31</b>
3.1	Beam Definition Detectors . . . . .	32
3.2	Detectors for event characterization . . . . .	34
3.3	Forward Spectrometer . . . . .	37
3.4	Data Collection . . . . .	42

<b>4</b>	<b>Data Analysis</b>	<b>44</b>
4.1	Overview . . . . .	44
4.2	Event Characterization . . . . .	45
4.2.1	Event Selection . . . . .	46
4.2.2	$E_T$ Distribution . . . . .	49
4.2.3	Centrality Determination . . . . .	51
4.2.4	Reaction Plane Determination . . . . .	53
4.3	Track Reconstruction and Properties . . . . .	54
4.3.1	Track Finding Algorithm . . . . .	55
4.3.2	Momentum Determination and Resolution . . . . .	56
4.3.3	Charge Separation . . . . .	60
4.3.4	Particle Identification . . . . .	62
4.4	Background Reduction . . . . .	68
4.4.1	Track Matching on VTX Chambers . . . . .	68
4.4.2	VTX Cut . . . . .	71
4.5	Efficiency and Corrections . . . . .	72
4.5.1	Tracking Efficiency . . . . .	73
4.5.2	Occupancy Correction . . . . .	74
4.5.3	Acceptance Correction . . . . .	81
<b>5</b>	<b>Monte Carlo Simulation</b>	<b>86</b>
5.1	Event Generator . . . . .	87
5.2	Acceptance for $\Lambda \rightarrow p + \pi^-$ . . . . .	90
5.3	Backtracking . . . . .	92
5.4	Investigation of Pair Cuts . . . . .	95
<b>6</b>	<b>Lambda Identification</b>	<b>103</b>
6.1	Overview . . . . .	103

6.2	Single Track Selection . . . . .	105
6.3	Pair Reconstruction . . . . .	106
6.3.1	Upstream Track Reconstruction . . . . .	106
6.3.2	Decay Vertex Determination . . . . .	107
6.4	Pair Cuts . . . . .	109
6.5	Background Subtraction . . . . .	117
6.6	Corrections of Acceptance and Pair Cuts . . . . .	121
<b>7</b>	<b>Results and Discussions</b>	<b>124</b>
7.1	Proton and Pion Spectra . . . . .	124
7.1.1	Inclusive Proton Spectra . . . . .	125
7.1.2	Inclusive Pion Spectra . . . . .	129
7.2	Lambda Yield and Spectra . . . . .	133
7.3	Lambda Directed Flow . . . . .	140
7.3.1	Experimental Results . . . . .	140
7.3.2	Comparison with Protons . . . . .	142
7.3.3	Comparison with RQMD prediction . . . . .	145
<b>8</b>	<b>Summary and Conclusions</b>	<b>150</b>
<b>A</b>	<b>Data Tables</b>	<b>154</b>
<b>B</b>	<b>Reconstruction of <math>\Delta^{++}</math></b>	<b>160</b>

# List of Figures

1.1	Schematic phase diagram of nuclear matter . . . . .	2
2.1	Schematic view of the geometry for a collision between two nuclei . . . . .	8
2.2	Schematic view of a collision in the transverse plane . . . . .	9
2.3	space-time evolution of a relativistic nuclear collision . . . . .	13
2.4	Nuclear stopping scenarios . . . . .	14
2.5	Proton rapidity density for central Au+Au collisions at the AGS . . . . .	16
2.6	Rapidity distributions for central 14.6 A·GeV/c Si+Au collisions compared with isotropic thermal distributions and distributions for a longitudinally expanding source . . . . .	20
2.7	Particle spectra for central 14.6 A·GeV/c Si+Au collisions at $y = 1.3$ compared to calculated spectra for a transversely expanding source . . . . .	21
2.8	Excitation function of radial expansion . . . . .	23
2.9	Directed flows of proton and pion in semi-central Au+Au collisions . . . . .	25
2.10	Hadron yields at AGS . . . . .	27
2.11	Hadron yields at SPS . . . . .	28
2.12	The energy dependence of the $K^+/\pi^+$ ratio in central Au+Au collisions . . . . .	29
3.1	E877 experimental setup . . . . .	32
3.2	A schematic view of the TCAL . . . . .	34
3.3	A schematic view of the PCAL . . . . .	36

3.4	Schematic layout of upstream detectors of the spectrometer . . . . .	38
3.5	Zoom view of the single chevron pattern . . . . .	39
3.6	Layout of the drift chamber . . . . .	41
4.1	Typical Pulse height distributions in BSCI S2 and S4 . . . . .	46
4.2	Good event cut on the cluster number in BVERs . . . . .	47
4.3	Good event cut on the number of hits in MWPCs . . . . .	48
4.4	$dN/dE_t$ distributions and transverse energy differential cross-section for TCAL and PCAL . . . . .	50
4.5	Impact parameter and total transverse energy . . . . .	51
4.6	Centrality as a function of $E_t$ for TCAL and PCAL . . . . .	52
4.7	Bend-plane geometry of a track passing through the E877 spectrometer	57
4.8	Spectrometer momentum resolution . . . . .	60
4.9	Pulse height distribution in TOFU . . . . .	61
4.10	Scatter plot of the inverse momentum $1/p$ versus the inverse of the measured velocity $1/\beta$ . . . . .	64
4.11	Squared mass resolution as a function of momentum . . . . .	65
4.12	Particle identification cuts . . . . .	67
4.13	Track matching at vertex chambers . . . . .	70
4.14	Particle identification plot with/without vertex chamber confirmation	72
4.15	Measured Occupancy Distributions in Spectrometer . . . . .	75
4.16	Probability of track survival . . . . .	76
4.17	Correlation of the track hit on DC2, DC3 and TOFU . . . . .	78
4.18	The weight of the occupancy correction for $\pi^-$ . . . . .	79
4.19	The weight of the occupancy correction for protons . . . . .	80
4.20	Spectrometer acceptance . . . . .	84
4.21	Acceptance corrections for proton in different rapidity slices . . . . .	85

5.1	$\Lambda$ spectra from the RQMD2.3 cascade model . . . . .	88
5.2	$dN/dy$ and the inverse slope of lambda from the RQMD v2.3 in cascade mode . . . . .	89
5.3	Simulation on proton emission at lambda decay . . . . .	91
5.4	Geometric acceptances for $\Lambda \rightarrow p + \pi^-$ . . . . .	92
5.5	Geometrically detecting efficiency for lambda in the spectrometer . . . . .	93
5.6	Simulation of invariant mass of $(p, \pi^-)$ from lambda's in the spectrometer . . . . .	94
5.7	Schematic diagram illustrating $\Lambda$ decay and reconstruction . . . . .	96
5.8	Investigation of $V_z$ distributions of true pairs and mixed pairs . . . . .	97
5.9	Investigation of the extrapolated track position at the target . . . . .	99
5.10	Investigation of the track matching parameters . . . . .	100
5.11	Investigation of the reconstructed momentum vector pointing . . . . .	102
6.1	The reconstructed $V_z$ distribution from $p$ and $\pi^-$ pair tracks . . . . .	108
6.2	Pair cuts for reducing background . . . . .	110
6.3	Scattering plots of invariant mass versus the cut parameters of pair tracks pointing away from the target . . . . .	111
6.4	Scattering plot of invariant mass versus track matching cut parameters . . . . .	112
6.5	Scattering plot of invariant mass versus the cut parameters of reconstructed momentum vector pointing back to the target . . . . .	113
6.6	Invariant mass distribution of $p\pi^-$ pairs . . . . .	115
6.7	Podolanski-Armenteros Plot for lambda identification . . . . .	116
6.8	One-dimensional correlation function for $p\pi^-$ pairs. . . . .	118
6.9	Background subtraction by mixed pair method . . . . .	119
6.10	Background subtraction by linear interpolation . . . . .	120
6.11	Acceptance plot for $\Lambda$ 's after the pair cuts . . . . .	122
6.12	Acceptance corrections for lambda with pair cuts . . . . .	123

7.1	Proton transverse mass spectra for the most central Au+Au collisions	126
7.2	Proton inverse slope parameters as a function of rapidity . . . . .	127
7.3	Rapidity distribution of protons for the most central Au+Au collisions	128
7.4	Pion transverse mass spectra for the most central Au+Au collisions .	130
7.5	Pion inverse slope parameters as a function of rapidity . . . . .	131
7.6	Rapidity distribution of pions for the most central Au+Au collisions .	132
7.7	$\Lambda$ transverse mass spectra for the most central Au+Au collisions . . .	134
7.8	$\Lambda$ transverse mass spectra for the semi-central Au+Au collisions . . .	135
7.9	$\Lambda$ inverse slope parameters for $< 4\% \sigma_{geo}$ . . . . .	136
7.10	$\Lambda$ inverse slope parameters for $4 - 10\% \sigma_{geo}$ . . . . .	137
7.11	$\Lambda$ rapidity distribution for the most central Au+Au collisions . . . . .	138
7.12	$\Lambda$ rapidity distribution for the semi-central Au+Au collisions . . . . .	139
7.13	$\Lambda$ azimuthal angular distributions . . . . .	141
7.14	$v_1(p_t)$ - dependence for $\Lambda$ . . . . .	143
7.15	Proton azimuthal angular distribution . . . . .	144
7.16	Comparison of $v_1(p_t)$ data between $\Lambda$ s and protons . . . . .	146
7.17	Directed flows of proton and $\Lambda$ as a function of rapidity predicted by the RQMD model (v2.3) . . . . .	147
7.18	Comparison of $\Lambda$ flow data with the predictions of RQMD model (v2.3)	148
7.19	Comparison of $K^+$ flow data with the predictions of the RQMD model (v2.3) . . . . .	149
B.1	Reconstruction of the $\Delta^{++}$ resonance . . . . .	161

# List of Tables

1.1	The accelerators for relativistic heavy-ion physics . . . . .	4
3.1	Trigger thresholds and down-scaling factors in 1995 . . . . .	43
4.1	Definition of windows in polar angle and pseudorapidity for the determination of the reaction plane . . . . .	54
4.2	Parameters for momentum resolution of the spectrometer in 1995 . .	59
4.3	The fit parameters of the squared-mass peak for different particles . .	66
4.4	Maximum momentum cuts for different particles . . . . .	68
4.5	Spectrometer fiducial cuts . . . . .	82
4.6	The dead sections of tracking detectors . . . . .	82
7.1	Comparison of $\Lambda/p$ ratio with the predictions of the RQMD model (v2.3)	139
7.2	Comparison of directed flow parameter $v_1$ between lambda and proton for different rapidity and centrality bins . . . . .	145
A.1	Protons $\sigma_{\text{top}}/\sigma_{\text{geom}} = 4\%$ . . . . .	155
A.2	Protons $\sigma_{\text{top}}/\sigma_{\text{geom}} = 4 - 10\%$ . . . . .	156
A.3	Positive pions $\sigma_{\text{top}}/\sigma_{\text{geom}} = 4\%$ . . . . .	157
A.4	Negative pions $\sigma_{\text{top}}/\sigma_{\text{geom}} = 4\%$ . . . . .	158
A.5	Lambda $\sigma_{\text{top}}/\sigma_{\text{geom}} = 4\%$ . . . . .	159
A.6	Lambda $\sigma_{\text{top}}/\sigma_{\text{geom}} = 4 - 10\%$ . . . . .	159

# Acknowledgments

First of all I want to thank my parents for their love and support. I am deeply indebted to my brothers and sisters for sharing the responsibility to bear the big family. Without their constant support and motivation, I wouldn't be able to reach this goal. I dedicate this thesis to my family.

I would like to express my most sincere gratitude to my thesis advisor, Prof. Jean Barrette, for his financial support throughout my study at McGill. I have been inspired in many ways by his guidance and advice. This work can not be done in such a short time period without his physics insight. I am especially grateful to him for spending tremendous amount of time on reading, correcting and commenting on my thesis.

I am deeply indebted to Prof. S. K. Mark for his generous help and support. He treated me as his own student. He provided me the great opportunity for working on the *R&D* project of the pad chambers for the PHENIX experiment. Although I wouldn't write any of this work in my thesis, I have learnt a lot from the hardware experience. It certainly will benefit me in my future career. I would also like to thank Prof. J. K. P. Lee for his generous help to make my life in Montreal with a lot of memorable fun.

I pay my special thanks and respects to my fellow graduate students, Yi Dai and Kirill Filimonov. We teamed up with Thongbay Vongpaseuth from Stony Brook for

the E877 1995 data analyses. Yi Dai did most of the software update for the data reduction and carefully calibrated the TOFU detectors. His hard work is deserved a high credit. I owe my gratitude to Kirill Filimonov, who always gave me a hand whenever I needed help. I also want to thank Thongbay Vongpaseuth, without whom the analysis of the 1995 data would not have been possible. I have been benefited a lot from the numerous discussions with them. My special thanks also go to Roger Lacasse, who introduced me to the E877 data analysis, from whom I inherited a wealth of computer programs for the construction of particle spectra. I want to thank Dr. Gaosheng Wang for his help during my writing period and thank Dr. Vasile Topor Pop for proofreading my thesis.

I also wish to thank Dr. Marzia Rosati and Dr. Nick Starinski who gave me a lot help while we were working on the PHENIX experiment. Many thanks to Dr. Anders Oskarsson for his great help in testing and implementing the front-end electronic readout for the pad chambers. It was my cherished experience to have worked with them. I learned a great deal from them to do professional work. I am also grateful to the McGill technical staff Leo Nikkinen and Steve Kancani for all their help and assistance in the detector constructions.

All my friends in Montreal made the years I spent there valuable and enjoyable. It is impossible for me to mention all their names and I will just thank them all.

Finally, I want to thank the E877 spokesmen professors Peter Braun-Munzinger and Johanna Stachel to provide me the opportunity to analyze the E877 1995 data for the lambda production. I also wish to thank all the members of the E877 collaboration who have made the experiment successful.

The E877 collaboration: J. Barrette<sup>5</sup>, R. Bellwied<sup>9</sup>, S. Bennett<sup>9</sup>, R. Bersch<sup>7</sup>, P. Braun-Munzinger<sup>2</sup>, W. C. Chang<sup>7</sup>, W. E. Cleland<sup>6</sup>, M. Clemen<sup>6</sup>, J. Cole<sup>4</sup>, T. M. Cormier<sup>9</sup>, Y. Dai<sup>5</sup>, G. David<sup>1</sup>, J. Dee<sup>7</sup>, O. Dietzsch<sup>8</sup>, M. Drigert<sup>4</sup>, K. Filimonov<sup>5</sup>, S. C. Johnson<sup>7</sup>, J. R. Hall<sup>9</sup>, T. K. Hemmick<sup>7</sup>, N. Herrmann<sup>2</sup>, B. Hong<sup>2</sup>, Y. Kwon<sup>7</sup>, R. Lacasse<sup>5</sup>, Q. Li<sup>9</sup>, T. W. Ludlam<sup>1</sup>, S. K. Mark<sup>5</sup>, R. Matheus<sup>9</sup>, S. McCorkle<sup>1</sup>, J. T. Murgatroyd<sup>9</sup>, D. Miśkowiec<sup>2</sup>, E. O'Brien<sup>1</sup>, S. Panitkin<sup>7</sup>, P. Paul<sup>7</sup>, T. Piazza<sup>7</sup>, M. Pollack<sup>7</sup>, Y. J. Qi<sup>5</sup>, C. Pruneau<sup>9</sup>, M. N. Rao<sup>7</sup>, E. Reber<sup>4</sup>, M. Rosati<sup>5</sup>, N. C. daSilva<sup>8</sup>, S. Sedykh<sup>7</sup>, U. Sonnadara<sup>6</sup>, J. Stachel<sup>3</sup>, E. M. Takagui<sup>8</sup>, S. Voloshin<sup>3</sup>, T. B. Vongpaseuth<sup>7</sup>, G. Wang<sup>5</sup>, J. P. Wessels<sup>3</sup>, C. L. Woody<sup>1</sup>, N. Xu<sup>7</sup>, Y. Zhang<sup>7</sup>, C. Zou<sup>7</sup>

<sup>1</sup> Brookhaven National Laboratory, Upton, NY 11973

<sup>2</sup> Gesellschaft für Schwerionenforschung, 64291 Darmstadt, Germany

<sup>3</sup> Universität Heidelberg, 69120 Heidelberg, Germany

<sup>4</sup> Idaho National Engineering Laboratory, Idaho Falls, ID 83402

<sup>5</sup> McGill University, Montreal, Canada

<sup>6</sup> University of Pittsburgh, Pittsburgh, PA 15260

<sup>7</sup> SUNY, Stony Brook, NY 11794

<sup>8</sup> University of São Paulo, Brazil

<sup>9</sup> Wayne State University, Detroit, MI 48202

# Chapter 1

## Introduction

Relativistic heavy ion physics is an interdisciplinary field that has emerged from particle physics and nuclear physics. Its subject is the study of bulk matter consisting of strongly interacting particles (hadrons/partons), commonly referred to as nuclear matter [1]. Although nuclear matter is unlike the ordinary matter of our every day experience, its physical properties can be described in similar fashion in term of equation of state (EOS). The equation of state describes how matter responds to changes in temperature, pressure and density. The theoretically predicted phase diagram for nuclear matter is schematically shown in Fig. 1.1. Nuclear matter in the ground state behaves like a liquid droplet: the constituent nucleons can move freely within the droplet, seldom escaping it. With a low energy excitation a liquid-vapor phase transition is expected to occur. At somewhat higher excitation, nucleons are excited into baryonic resonance states such as ( $\Delta$ ,  $N^*$ ), along with accompanying particle production ( $\pi$ ,  $K$ ,  $\Lambda$ , etc). In heavy-ion collisions, such excitation is expected to create hadronic matter. This region has been accessible in heavy ion studies at the AGS accelerator at Brookhaven National Laboratory (BNL) and at the SPS accelerator at CERN. If further heated and/or compressed, another phase transition

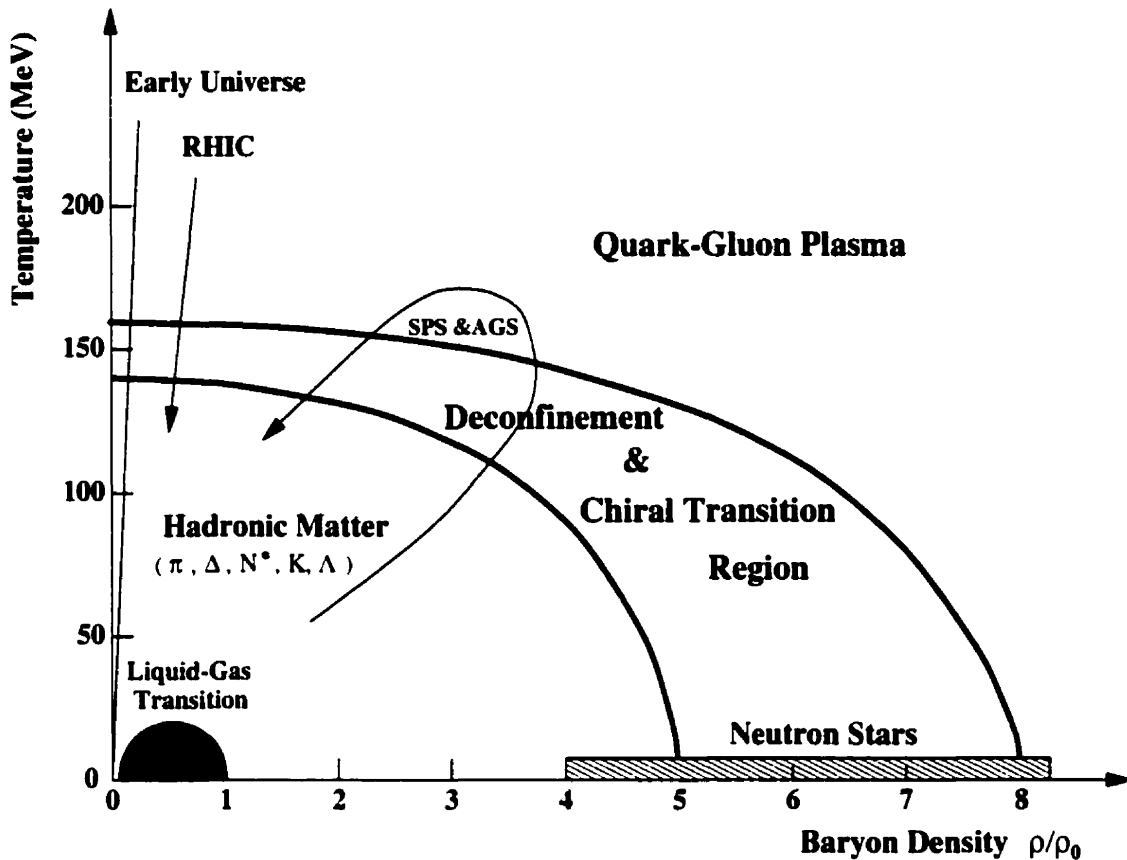


Figure 1.1: Schematic phase diagram of nuclear matter (from [1]).

from the hadronic matter to the quark-gluon plasma (QGP) may occur, where the individual hadrons are likely to lose their identity and quarks and gluons become deconfined [2]. Searching for the QGP state becomes the major driving force of the study of relativistic heavy-ion collisions.

Studying these phenomena is of cross-disciplinary interests [3], because

- exploring quantum chromodynamics (QCD) under extreme conditions could provide insight into the nature of quark confinement and QCD vacuum [4, 5], therefore advance our understanding of the strong interaction.
- hot and dense nuclear matter existed in early stages of the evolution of the

universe. It is believed that the early universe underwent the quark-hadron phase transition a few microseconds after the Big Bang explosion. The general nucleosynthesis is also of interest in cosmology.

- in astrophysics, the nuclear matter equation of state governs neutron star collapse and supernova expansion dynamics. The region of high baryon densities and very low temperatures is important for various aspects of the stellar evolution.

The primary motivation to use relativistic heavy-ion collisions is to create and study QGP in controlled laboratory conditions. The endeavor of experiments so far has been mainly focused on two aspects:

- **Assess the initial conditions for QGP formation:** according to the lattice QCD calculations [6], the critical conditions for the QGP phase transition are reached at a critical temperature  $T_c \sim 150$  MeV. It corresponds to a critical energy density  $\epsilon_c \sim 1\text{-}3$  GeV/fm<sup>3</sup>. Experimental verification of these initial conditions is an important topic in heavy-ion research.
- **Search for signals of QGP phase transition:** there are many proposed “signatures” for QGP [7, 8, 9], such as direct photon and lepton probe,  $J/\psi$  suppression, strangeness enhancement, etc. None of them is an unambiguous observable for the QGP state and many of them can be produced by secondary particle interactions, too. The signals of QGP always have to compete with the backgrounds from the hot hadronic gas phase, even they are modified by the final-state interactions in the hadronic phase. Of great concern is our ability to recognize when a QGP has been formed. Many experimental projects at AGS and SPS have been devoted to this research.

The systematic study of relativistic heavy-ion collisions began in early 1980s.

Table 1.1: The accelerators for relativistic heavy-ion physics

Accelerator Facility	Laboratory	Heaviest Beam	Highest Energy (A · GeV)	Available
BEVALAC	LBL	$A = 57$	2.1	1982
SIS	GSI	$^{197}\text{Au}$	1	1988
AGS	BNL	$^{28}\text{Si}$	14.6	1986
		$^{197}\text{Au}$	11.5	1992
SPS	CERN	$^{32}\text{S}$	200	1986
		$^{208}\text{Pb}$	158	1994
RHIC	BNL	$^{197}\text{Au}$	100x100	1999
LHC	CERN	$^{208}\text{Pb}$	3150x3150	2005

The existing and future experimental facilities involved in the relativistic heavy-ion research are listed in Table 1.1. The progress in this field has been achieved and reported in a series of Quark Matter proceedings [10]. So far no unambiguous QGP signal has been obtained yet. The majority of the observed effects can be explained by conventional hadron scenarios. However a threshold effect in the anomalous  $J/\psi$  suppression for central Pb+Pb collisions has been observed at the SPS [11] recently. This implies that the QCD phase transition may be reached in these collisions. The search and study of QGP will be continuing in the more powerful colliders — the RHIC at BNL later this year and the LHC at CERN in 2005.

After decades of experiments, what has become clear from the hadronic observables are:

1. large degree of stopping power occurs in the colliding system [12, 13]. A state of matter with high baryon density up to several times the normal nuclear density has been formed in the initial stage of heavy colliding systems at the AGS and

SPS [14, 15]. This implies that a baryon-rich QGP may have been formed in those systems.

2. collective expansion is superimposed on the random thermal motion among the particles involved in the collisions [16]. As a consequence of large stopping, tremendous pressure is built up in the core of the collision, which leads to certain kinds of collective motions in releasing the pressure. The study of the flow patterns provides a sensitive probe to search for new phases or exotic states of nuclear matter, which are supposed to be reflected in the equation of state.
3. Some thermal and chemical equilibration has been reached as visible in the final states obtained at the AGS and SPS energies [16, 17].

This thesis will examine hadronic data from Au+Au collisions at AGS at 11.5 GeV/nucleon and mostly focuses on the production of lambda hyperon. An experimental overview of the hadronic physics in relativistic heavy-ion collisions will be presented in chapter 2. The E877 experimental setup is briefly described in chapter 3. The details of data analysis procedure will be given in chapter 4. It covers the event selection and characterization as well as an extensive discussion of track reconstruction, selection, correction and particle identification. In chapter 5 we will explore the analysis of lambda hyperon. A Monte Carlo simulation studying lambda decay and reconstruction was performed. Then the details of the lambda identification will be discussed in chapter 6. The results and discussions will be displayed in chapter 7. Summary and conclusions are given in chapter 8.

## Chapter 2

### Physics Issues

In relativistic heavy-ion (RHI) collisions the system created is a rapidly evolving multi-particle entity and the experimental observables correspond to an integral over the complete space-time history of the reaction until freeze-out. In principle, hadrons, in bound quark states, cannot directly probe the deconfined QGP state. Even in the absence of a QGP state, strongly interacting hadrons only probe the early stages of the nucleus-nucleus collisions indirectly. Why do we still wish to measure and understand the hadronic observables from the RHI collisions? The main reasons are as follows:

- Hadrons (protons, pions and kaons) are the most abundantly produced particles in RHI collisions and they are the easiest for experiments to measure.
- Hadrons carry away most of the energy from the collision region. They are very important for inferring the energy density and dynamics of the system.
- Hadronic spectra provides an important information on the thermalization and collective expansion of the evolving system. One can use it to extract some thermodynamic variables such as temperature and pressure as well as flow parameters.

- The study of the flow patterns of hadrons is expected to reveal changes that hot and dense matter might undergo in the course of RHI collisions [19].
- Hadronic correlations can provide the space-time configuration (“geometry”) of the system evolution.
- Any theoretical models describing RHI collisions must be able to reproduce the hadronic data. Thus hadronic observables are a very important test for the theories.

In this chapter, we will overview these hadronic physics issues of RHI collisions from the experimental point of view. We first introduce some basic concepts and kinematic variables used in the context of relativistic heavy-ion physics, then we describe nuclear stopping and discuss the phenomenology on hadron production in different aspects of thermal and collective behaviours. At last we will briefly discuss the strangeness production and introduce to the subject of this thesis — lambda production in Au+Au collisions at AGS energy.

## 2.1 Relativistic Heavy-Ion Collisions

### 2.1.1 General Features

Heavy ions, with large enough energies, can be considered as classic particles because their *De Broglie* wavelength is much smaller than the typical nuclear sizes. In fact, at relativistic energies even the nucleons can generally be considered as classic particles. Together with the short range of the nuclear interaction, this implies that a simple geometrical model can characterize the collisions between two nuclei (see Fig. 2.1). The impact parameter  $b$  separates the nucleons into *participants* with primary nucleon-nucleon collisions, and *spectators* which proceed with little pertur-

bation along the original direction. The total reaction cross section ( $\sigma_{geo}$ ), number of participants (centrality) and related kinematic quantities are usually calculated from the simple geometrical considerations.

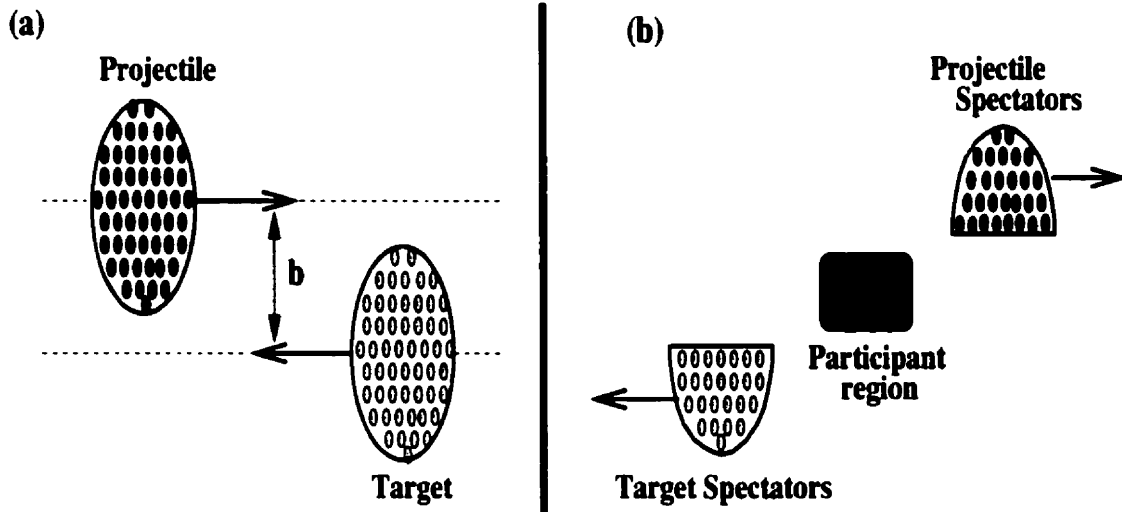


Figure 2.1: Schematic view of the geometry for a collision between two nuclei in the center-of-mass frame. (a) depicts the pre-collision condition, projectile and target collide with impact parameter  $b$ . (b) after the collision, projectile and target spectators continue while the participant build up the reaction zone.

The impact parameter  $\vec{b}$ , which is defined as the transverse distance between the centra of the colliding system, is a two-dimensional vector. If there is no deformation and polarization of target and projectile nuclei, the impact parameter  $\vec{b}(b, \psi_r)$  determines the collision geometry. In experiment, the collisions between heavy ions are characterized in terms of centrality and the reaction plane angle ( $\psi_r$ ).

The centrality is related to the violence of the collision. According to the geometrical model, the centrality quantifies the overlap between the projectile and the target nuclei, i.e. the size of participant zone. For a symmetric reaction system (assuming sharp edges), the relationship between the centrality and the impact parameter is

given by

$$\frac{\sigma_{top}}{\sigma_{geo}} = \frac{\int_0^b db'b'}{\int_0^{2R} db'b'} = \left(\frac{b}{2R}\right)^2 \quad (2.1)$$

where  $R$  is the radius of the nucleus. Unfortunately, the impact parameter is not directly measurable. We have to use other measurable quantities such as the total transverse energy  $E_t$  to infer the centrality. Detail descriptions about the centrality determination in ES77 experiment will be discussed in section 4.2.

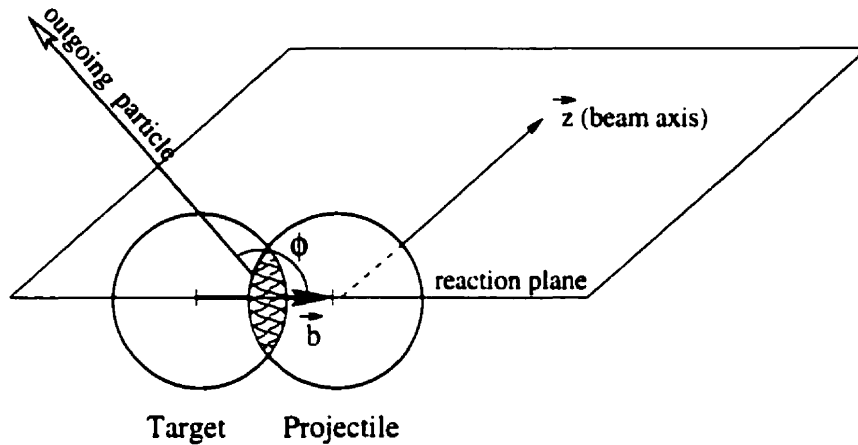


Figure 2.2: Schematic view of a collision in the transverse plane.

In the collision of two nuclei, the azimuthal asymmetry of the collision is defined relative to the reaction plane angle  $\psi_r$ . A schematic view of a collision in the transverse plane is shown in Fig. 2.2. The reaction plane is defined by the beam axis  $\vec{z}$  and the impact parameter vector  $\vec{b}$ . In the transverse direction,  $\phi$  is the azimuthal angle of an outgoing particle, measured with respect to the direction of the impact parameter. Flow is present if particle emission is not isotropic. The azimuthal anisotropy can be quantified by general Fourier expansion [20] of the azimuthal distributions of the produced particles. The detailed descriptions of the reaction plane determination as performed in the ES77 experiment can be found in [21, 22].

### 2.1.2 Kinematic Variables

The heavy-ion collisions discussed in this thesis involve very energetic ions. A description in terms of relativistic quantities is therefore needed. Since the direction transverse to the beam is essentially Lorentz invariant, a convenient choice is in terms of coordinates longitudinal and transverse with respect to beam axis. The z-axis is along the beam direction. Thus the rapidity variable  $y$  is introduced as the longitudinal variable:

$$y = \frac{1}{2} \ln \left( \frac{E + p_z}{E - p_z} \right) \quad (2.2)$$

where  $E$  is the total energy and  $p_z$  is the longitudinal component of the momentum. The rapidity coordinate is additive in Lorentz transformations which allows for an easy comparison of rapidity distribution  $dN/dy$  in different frames. A Lorentz transformed rapidity  $y'$  is related to the rapidity  $y$  in a moving frame as

$$y' = y + y_0 \quad (2.3)$$

where

$$y_0 = \frac{1}{2} \ln \left( \frac{1 + \beta}{1 - \beta} \right) \quad (2.4)$$

is the rapidity of the moving system with the speed of the inertial frame,  $\beta$ , so that the rapidity distribution such as  $dN/dy$  is simply shifted by  $y_0$  and thus has its shape unchanged when changing reference frame.

With this definition, we can easily separate target-like from projectile-like particles in fixed target experiments. For example, Au+Au collision at 11.5 A · GeV/c in the laboratory reference frame, the target rapidity is located at  $y = 0$  and projectile (beam) rapidity at  $y = 3.2$ . The rapidity region which corresponds to the center of mass is often called mid-rapidity and is located at  $y_{cm} = 1.6$ . In the ultra-relativistic limit  $p \gg m$ , where the rest mass of the particle is negligible, the rapidity  $y$  is

approximately equal to the pseudo-rapidity  $\eta$  defined as:

$$\eta = -\ln\left[\tan\left(\frac{\theta}{2}\right)\right] \quad (2.5)$$

where  $\theta$  is the polar angle between the momentum vector  $\vec{p}$  and the z-axis.

In the direction perpendicular to the beam or z-axis, the transverse momentum  $p_t$  and transverse mass  $m_t$  are very important transverse variables defined as:

$$p_t = \sqrt{p_x^2 + p_y^2} \quad (2.6)$$

$$m_t = \sqrt{p_t^2 + m^2} \quad (2.7)$$

where  $m$  denotes the rest mass of the particle. The  $p_t$  of a produced particle is often small compared to the longitudinal momentum  $p_z$ .

The total transverse energy  $E_t$  is another useful quantity to describe the centrality of collisions as well as the energy flow closely related to the energy density produced in the collisions. It is defined as

$$E_t = \sum_i E_i \sin \theta_i \quad (2.8)$$

where the summation is performed over all particles,  $\theta_i$  is the polar angle of the  $i^{\text{th}}$  particle relative to the beam axis.

To describe the particle production in high energy physics, we often use the invariant differential cross section,  $E \frac{d^3\sigma}{d^3p}$ . In terms of rapidity ( $y$ ) and transverse momentum ( $p_t$ ) or transverse mass ( $m_t$ ), together with these identities:

$$E = m_t \cosh(y), \quad p_z = m_t \sinh(y), \quad \frac{dp_z}{E} = dy \quad (2.9)$$

the invariant differential cross section can be expressed as:

$$E \frac{d^3\sigma}{d^3p} = E \frac{1}{p_t} \frac{d^3\sigma}{dp_t dp_z d\phi} = \frac{1}{p_t} \frac{d^3\sigma}{dp_t dy d\phi} = \frac{1}{m_t} \frac{d^3\sigma}{dm_t dy d\phi} \quad (2.10)$$

If the distribution is azimuthally symmetric, integrating over  $\phi$  gives a prefactor  $\frac{1}{2\pi}$ . The 3-dimensional distribution reduces to 2-dimensional one

$$E \frac{d^3\sigma}{d^3p} = \frac{1}{2\pi} \frac{1}{m_t} \frac{d^2\sigma}{dm_t dy} \quad (2.11)$$

### 2.1.3 Space-Time Evolution of RHI Collisions

The theoretically predicted space-time evolution of a relativistic nuclear collision is shown in Fig. 2.3. Due to the effect of Lorentz contraction, the colliding nuclei are shown like “pancake” in the center-of-mass frame. Soon after the collision, the energy density reaches a maximum and may even be enough to make the formation of the QGP possible [7, 23]. After a certain proper time has passed, local equilibrium is achieved and the laws of hydrodynamics become applicable [7]. The plasma then expands, and therefore its temperature eventually drops below the critical transition temperature  $T_c$ . At this point, hadrons start to “crystallize” out of the QGP phase, a process in which the system goes from the large number of degrees of freedom (partons) of QGP to the smaller number available in the hadronic phase.

At this stage, the system exists in the *mixed phase*, where hadron gas coexists with QGP. The source continues to evolve into the expansion stage of the hadron gas with rescattering of many-body hadrons. The expansion still continues until the *freeze-out*, where interactions cease due to the low density. So the particles can be considered in their *final state*.

The hadronic observables are sensitive probes for the dynamics of these collisions. Disregarding the spectators, let focus on the participant region only. The nuclear stopping and some important thermodynamic variables such as temperature and pressure can be inferred from the hadronic observables.

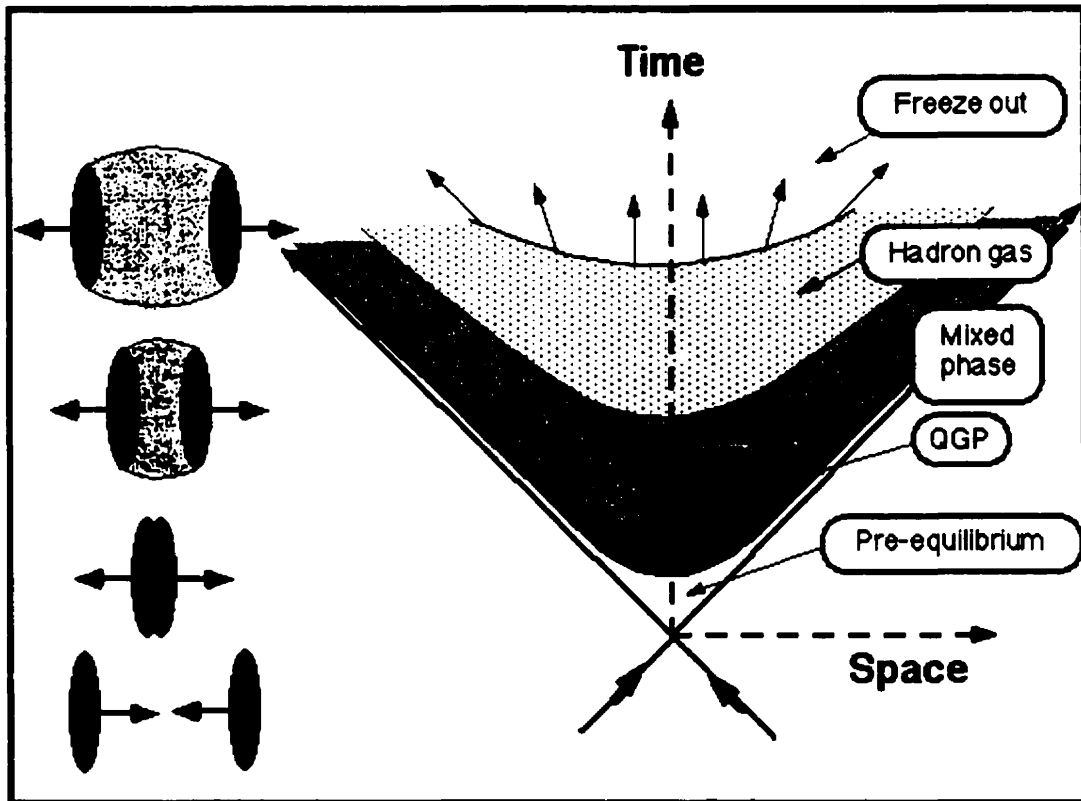


Figure 2.3: The theoretically predicted space-time evolution of a relativistic nuclear collision (from [23]).

## 2.2 Nuclear Stopping Power

The nuclear stopping power is defined as the degree to which the energy of relative motion of the colliding nuclei is transformed into other degrees of freedom. It determines the amount of energy and volume, therefore the energy density, deposited in the reaction zone. The mechanism of energy deposition is dependent on the energy, via nucleon-nucleon collisions as well as hard scattering on the parton level. At AGS energies, soft nucleon-nucleon collisions are dominant processes for energy deposited in the reaction zone.

There exist two extreme regime regarding the nuclear stopping [3]: the *full stopping regime* where baryons stemming from the colliding nuclei are fully stopped and forming baryon rich matter in the reaction zone, and the *transparency regime* where the initial baryon contents from the projectile and target will continue without being slowed down considerably. Two models has been developed to describe the stopping scenarios: Landau model for the full stopping [24], and the Bjorken model for nuclear transparency [25]. The two types of nuclear stopping scenarios are sketched in Fig. 2.4.

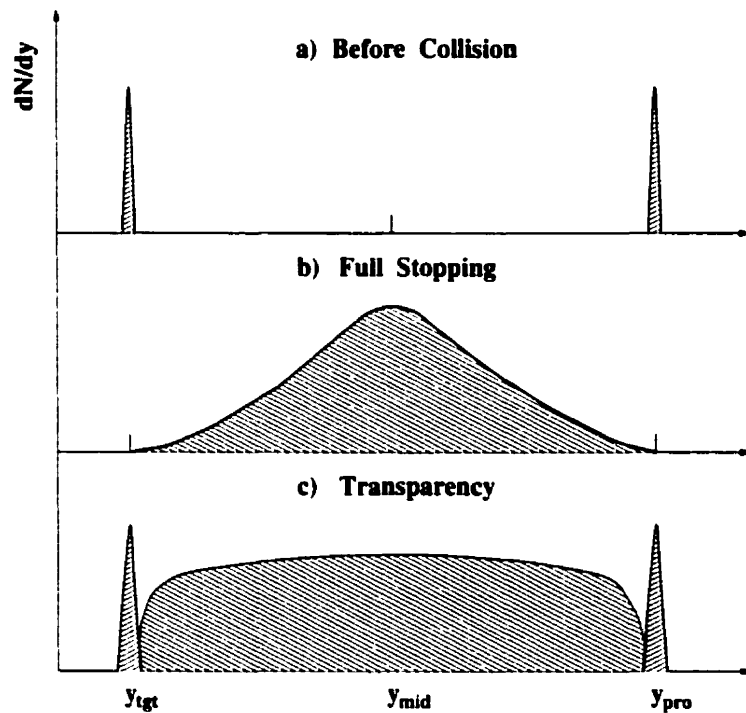


Figure 2.4: Nuclear stopping scenarios: a) before the collision; b) full stopping; c) transparency

The two regimes lead to essentially different physics. In the full stopping scenario, which has been examined in AGS and SPS energies, the energy is deposited in a baryon-rich environment in mid-rapidity region. These reactions provide a tool to

study very highly excited baryon-rich matter, or eventually baryon-rich QGP. Such baryon-rich plasma is expected in the dense inner core of neutron stars. In the transparent scenario, that RHIC and LHC are expected to reach, the energy density is deposited in a relatively baryon-free mid-rapidity region, where baryon-free QGP may form. The high temperature and low baryon density matter is believed to have existed in the early universe before hadrons were formed.

The nuclear stopping power can be inferred from the measurements of the transverse energy  $E_t$  production and its spatial distribution in the central collisions. The amount of transverse energy after the collision provides an indication of the energy transformed into particle production. The measured transverse energy densities  $dE_t/d\eta$  in central Au+Au collisions at the AGS [12] and Pb+Pb collisions at the SPS [13] are up to 200 and 450 GeV per unit pseudorapidity, respectively. Using Bjorken's formula [25] we can estimate the energy density  $\epsilon$  in the fireball formed in the collisions to be about 1.3 and 3 GeV/fm<sup>3</sup> [26]. These values indicate the energy deposited in the reaction zone has reached the critical energy density predicted by the lattice QCD calculations. In interpreting these values, one must however keep in mind that these values are highly model dependent, which simply take the total measured transverse energy and divides by the estimated volume of the system derived from Bjorken longitudinal expansion. The actual energy density changes rapidly as the system evolves during the collision process.

Another type of information on the nuclear stopping power is the determination of the final-state proton rapidity distributions. This has been performed at both the AGS and SPS. Fig. 2.5 shows the distribution of protons in central Au+Au collisions at the AGS, resulting from the combination of data of two experiments [14, 27, 28]. The measured  $dN/dy$  distribution of protons peaks at mid-rapidity and a width significantly narrower than that observed from Si+Au system [30, 31]. This implies the stopping power is indeed extremely large and the baryon stopping is very close

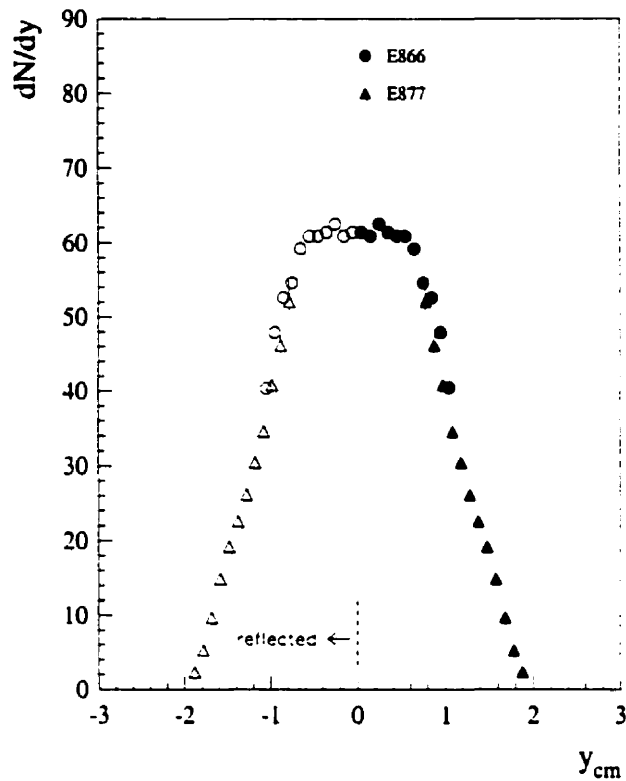


Figure 2.5: Proton rapidity density for central Au+Au collisions at the AGS at  $\sim 11$  GeV/c. The figure is taken from [29]. The open symbols are reflections of the measured points about midrapidity.

to full stopping in Au+Au system. A similar difference is also observed for the net proton rapidity distributions in Pb+Pb and S+S collisions at SPS energy [32, 15].

## 2.3 Phenomenology of Hadron Production

### 2.3.1 Fireball Model

The *fireball* model [33] was the first attempt to explain the measured particle spectra in RHI collisions. In such approach, the hadronic matter is assumed to be globally

thermalized by the end of the reaction, the particle emits from a purely thermal source, called as a *fireball*. The number of particles of a given species produced into an element of phase space, with Boltzmann approximation, is given by

$$\frac{d^3 N}{d^3 p} \propto e^{-(E-\mu)/T} \quad (2.12)$$

where  $T$  is the temperature of the source.  $E$  is the center-of-momentum energy associated with  $d^3 p$ , and  $\mu$  is the chemical potential. Expressed in terms of the invariant multiplicity, rapidity and transverse mass, it becomes

$$\frac{d^2 N}{m_t dm_t dy} = N_B(y) \frac{m_t}{m} \exp\left(-\frac{m_t - m}{T_B(y)}\right) \quad (2.13)$$

where  $m$  is the mass of the particle.  $N_B$  is the normalization and  $T_B$  is the inverse slope parameter.  $T_B(y) = T / \cosh(y - y_{cm})$  if the “fireball” is stationary. Through this thesis, expression (2.13) will be used to fit all the transverse mass spectra as a first order approximation. The fitting involves two parameters:  $N_B$  and  $T_B$ . Our interest is focus on the shape of the spectra, i.e. extracting the inverse slope parameter  $T_B$ .

The integration of Eq. (2.13) over  $m_t$  gives out the expected rapidity distribution  $dN/dy$ ,

$$\frac{dN}{dy} = \int_m^\infty \frac{d^2 N}{m_t dm_t dy} dm_t = N_B m T_B(y) \left(1 + 2\frac{T_B(y)}{m} + 2\frac{T_B^2(y)}{m^2}\right) \quad (2.14)$$

If the fireball is stationary, i.e. it emits isotropically, one can expects from Eq. (2.14)

$$\frac{dN_{iso}}{dy} \propto m^2 T (1 + 2\chi + 2\chi^2) \exp(-1/\chi), \quad (2.15)$$

where  $\chi = T / (m \cosh(y - y_{cm}))$ .

This simple model provides a good description for the general behavior of the particle spectra produced in RHI collisions. It actually has been used as a base to the analysis of many experimental data. However, the experimental particle spectra

in both longitudinal and transverse, can not completely be fitted by Eq. (2.13) and (2.15), even considering the contributions of the resonance decays. There exist a few features of the experimental spectra incompatible with the assumption of the stationary fireball: (1) an appearance of a “shoulder arm” in the transverse momentum spectra of identified particles [34]; (2) a quasi-linear dependence of the average kinetic energy on the particle mass (or charge) [35]; and (3) much wider  $dN/dy$  distributions than the isotropic prediction from Eq. (2.15) [36]; (4) the observation of azimuthal anisotropy of particle emission [37, 20] All these features provide an experimental evidence for the existence of collective flow (radial, longitudinal and transverse) in the RHI collisions.

### 2.3.2 Radial Flow

The radial flow arises from the radial expansion of the hot and dense fireball. It is present in the freeze-out stage. Therefore its effect is directly visible from the shape of the measured hadronic spectra in the central collisions. Some phenomenological models have been developed to explain the shape of those spectra.

The blast-wave model was first introduced to describe the radial expansions of the fireball [38], which is driven by the shock waves produced after nuclear matter has been compressed and heated in RHI collisions. It assumed that the kinetic energy of collective expansion comes from the the initial thermal energy. The energy distribution in the center-of-mass for particle emitted from a thermally equilibrated and radially expanding fireball, characterized by a temperature  $T$  and a radial flow velocity  $\mathcal{J}_r$ , can be described by [38]

$$\frac{dN}{dE d\Omega} = \frac{8\pi e^{\mu/T}}{(2\pi\hbar)^3} \exp\left(\frac{-\gamma E}{T}\right) \left[ \left(\gamma + \frac{T}{E}\right) \frac{\sinh \alpha}{\alpha} - \frac{T}{E} \cosh \alpha \right] \quad (2.16)$$

where  $E$  and  $p$  are the total energy and momentum of the particle in the center of mass.  $\gamma = (1 - \mathcal{J}_r^2)^{-1/2}$ , and  $\alpha = \gamma \mathcal{J}_r p / T$ .

In the original blast-wave model, the radial expansion of the fireball was assumed to be spherically symmetric. This model can explain the experimental data well at the Bevalac/ SIS energies (around 1 A-GeV/c) [38, 34]. However, it becomes improper at higher energy regime simply because of the significant Lorentz contraction. At the AGS energies ( $\sim 11$  A GeV), the Lorentz contraction factor is about 5:1 and becomes 10:1 at SPS energies. This effect leads to non-spherical collective expansion. A cylindrically symmetric fireball was introduced to describe the radial expansion at the AGS and SPS energies [36, 16]. Decoupling the collective expansion into longitudinal and transverse flow becomes necessary and also provides a convenient way to compare experimental results with theoretical predictions [16].

The longitudinal flow can be deduced from the rapidity distribution analysis on the experimental data from the AGS and SPS. The boost-invariant longitudinal expansion model was originally postulated by Bjorken [25]. A phenomenological model [36] modified the boost-invariant scenario by restricting the boost angle  $\eta$  to the interval  $(\eta_{min}, \eta_{max})$ . The rapidity distribution is then the integral over the uniformly distributed thermal sources (2.15) boosted individually by  $\eta$ :

$$\frac{dN}{dy} = \int_{\eta_{min}}^{\eta_{max}} d\eta \frac{dN_{iso}}{dy}(y - \eta) \quad (2.17)$$

A comparison of the measured rapidity distributions for central 14.6 A-GeV/c Si+Au collisions with isotropic thermal distributions at  $T=0.12$  GeV and distributions for a source at the same temperature expanding longitudinally with a mean velocity  $\langle J_l \rangle = 0.52c$  are shown in Fig. 2.6 (from [16]). The agreement between the measured distributions and the model with a longitudinal flow is remarkably good for all particle species.

In the same phenomenological approach, the transverse mass distributions are given by

$$\frac{dN}{m_t dm_t} \propto \int_0^R r dr m_t I_0 \left( \frac{p_t \sinh \rho}{T} \right) K_1 \left( \frac{m_t \cosh \rho}{T} \right) \quad (2.18)$$

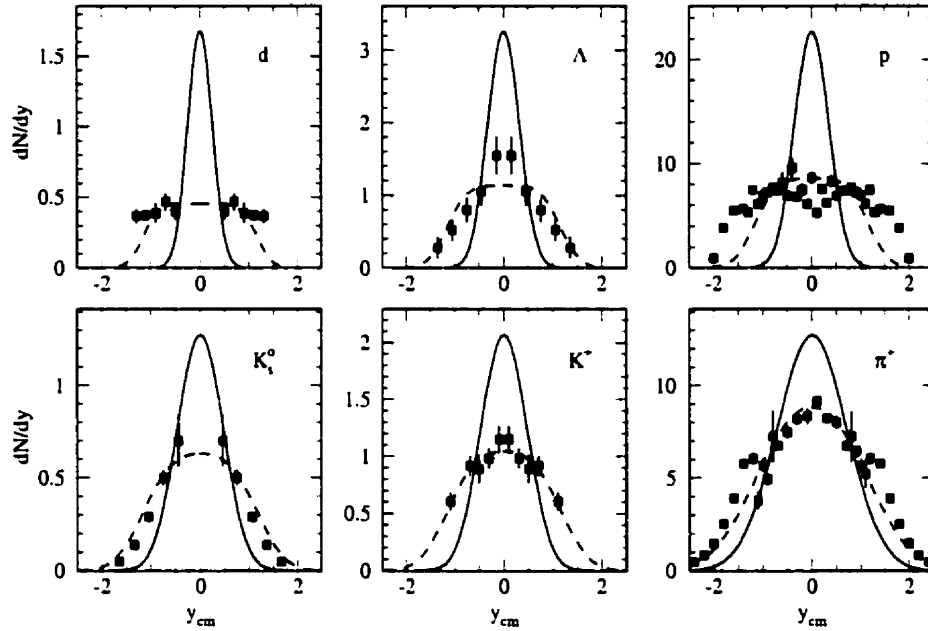


Figure 2.6: Rapidity distributions for central 14.6 A-GeV/c Si+Au collisions compared with isotropic thermal distributions at  $T=0.12$  GeV (solid lines) and distributions for a source at the same temperature expanding longitudinally with a mean velocity  $\langle \beta_t \rangle = 0.52c$  (dashed lines) (from [16]).

where  $R$  is the radius of the fireball.  $I_0, K_1$  are modified Bessel functions and  $\rho = \tanh^{-1} \beta_t$ .  $\mathcal{J}_t(r) = \mathcal{J}_s \left( \frac{r}{R} \right)^\alpha$  with  $\alpha = 1$ . Two free parameters, the temperature  $T$  and the surface transverse velocity  $\mathcal{J}_s$ , determine the shape of the  $m_t$  spectra. In general, the fits to the experimental spectra show a strong anti-correlation of these two parameters. Temperatures in the range from 100 to 200 MeV together appropriate flow parameters can well describe the experimental data. Fig. 2.7 shows such fits of the transverse mass spectra in Si+Au collisions at 14.6 A-GeV/c. A good agreement between the data and calculations is consistent with two sets of fitting parameters:  $\langle \beta_t \rangle = 0.39$  (0.33) $c$  at fixed temperatures  $T = 0.12$  (0.14) GeV. Similar analysis of the SPS data yields that the maximum transverse velocities are 0.41c and 0.6c with a

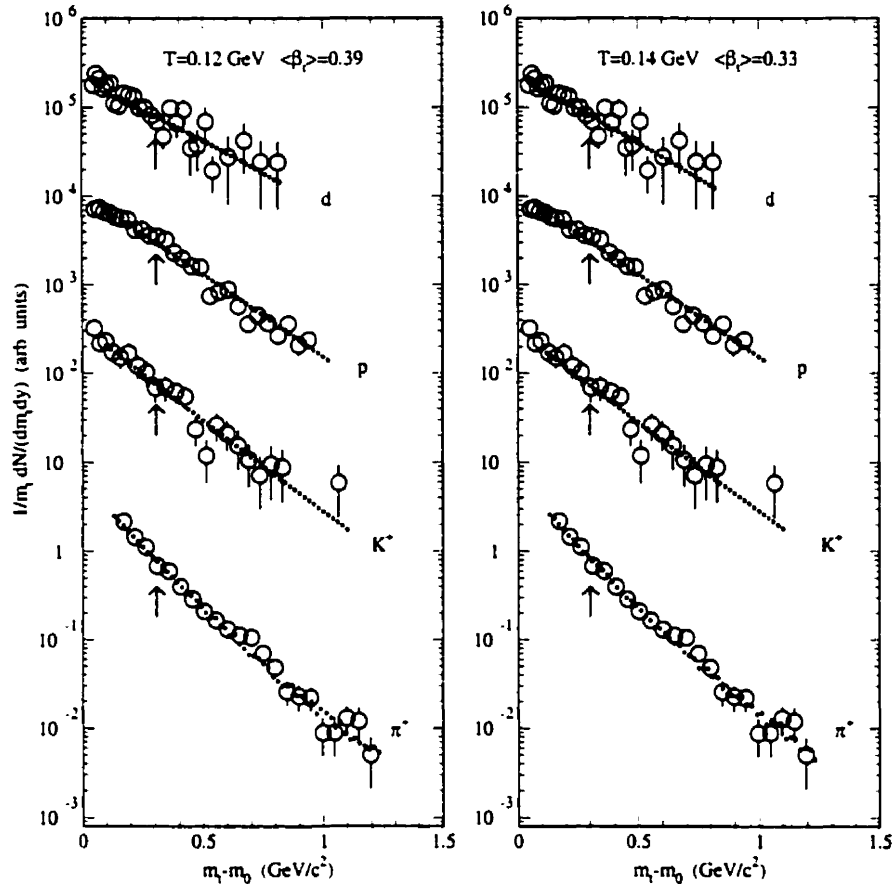


Figure 2.7: Particle spectra for central 14.6 A·GeV/c Si+Au collisions at  $y = 1.3$  compared to calculated spectra for a source at  $T = 0.12$  GeV expanding transversely with a mean velocity  $\langle\beta_t\rangle = 0.39c$  (left) and a source at  $T = 0.14$  GeV and  $\langle\beta_t\rangle = 0.33c$  (right). The arrows indicate the beginning of the fit region (from [16]).

fixed temperature  $T \sim 140$  MeV for S+S and Pb+Pb collisions, respectively. These values correspond to average transverse flow velocities of  $0.27c$  and  $0.4c$  [39]. One can see that there is some flexibility in the fitting procedures which results in a trade-off in the values of the two parameters. How to resolve this ambiguity in the value of  $(T, \beta_s)$  is still under studies.

In summary, all above phenomenological models on the collective expansion of the fireball can be extended to a consistent hydrodynamical descriptions. When two heavy nuclei collide with each other, the collision zone is highly compressed and heated. The compression and heating build up the high pressure gradients which induces additional collective motion (flow) superimposed on the thermal motion at the stage of expansion. The observed particle velocity has then two components: the thermal random velocity and the collective flow velocity. The random thermal motion is determined by the thermal temperature, which is common for all particles. The collective flow velocity is assumed to be the same for all particles so that the collective kinetic energy is then dependent on the particle mass: particle with heavy mass carry more collective energy. As a results, the shapes of all measured hadronic spectra can be well described in this approach.

To date, the shape of the observed hadronic spectra from the Bevalac/SIS energies to the AGS and SPS energies can be well described in the hydrodynamical approach. Fig. 2.8 presents the excitation function of the extracted temperature and flow velocity parameters with respect to the bombarding energies [39]. The effect of resonance formation and decay is neglected in this picture. Both quantities seem to saturate around  $E_{beam} \approx 10 \text{ A}\cdot\text{GeV}$ .

### 2.3.3 Azimuthally Anisotropic Flow

Unlike radial flow, the azimuthally anisotropic flow is developed early in the course of a nucleus-nucleus collision [40]. It carries out the memory of the collision geometry and principally reflects the non-equilibrium aspects of the collisions.

The measurement of the azimuthally anisotropic flow requires the definition of a reaction plane, which is defined by the impact parameter vector and the incident beam direction (Fig. 2.2). The reaction plane can be determined by directivity method [41],

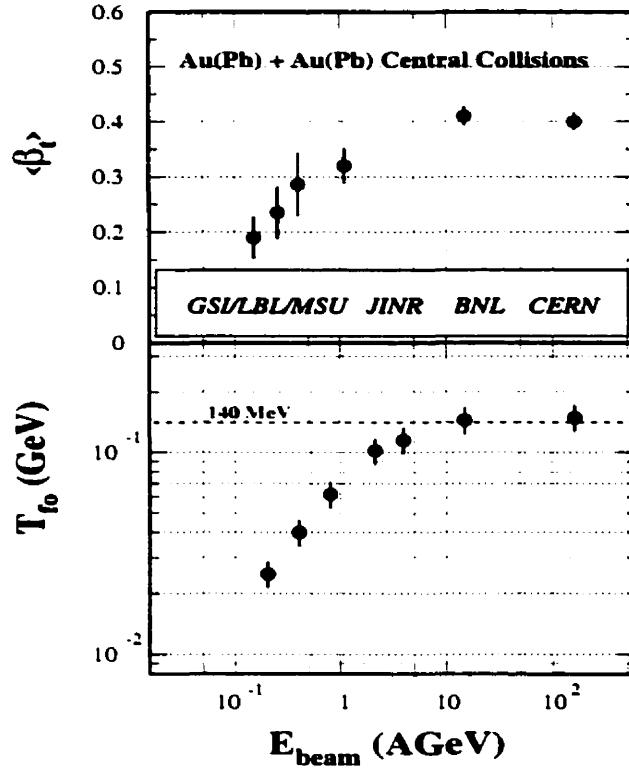


Figure 2.8: Compilation of the freeze-out temperature  $T_{f_0}$  and average collective flow velocity  $\langle \beta_t \rangle$  as a function of beam energy. The figure is taken from [39].

or by transverse energy method [20]. The directivity method requires  $4\pi$  coverage of detectors to provide the momentum three vectors of identified particles in the final state. The E877 experiment uses the transverse energy distribution measured by its nearly  $4\pi$  covered calorimeters to reconstruct the reaction plane event-by-event. A brief description of the reaction plane determination will be given in following chapter, fully detailed descriptions can be found in [21, 22].

Once the reaction plane is defined, the azimuthal anisotropies of particle emissions can be quantified by mean of Fourier expansions [20]. Thus the azimuthally asymmetric distribution with respect to the reaction plane can be expressed in a form

of Fourier series:

$$E \frac{d^3 N}{d^3 p} = \frac{d^3 N}{p_t dp_t dy d\phi} = \frac{1}{2\pi} \frac{d^2 N}{p_t dp_t dy} \left( 1 + \sum_{n=1}^{\infty} 2v_n \cos(n(\phi - \psi_r)) \right) \quad (2.19)$$

where  $\psi_r$  represents the reaction plane angle and the sine terms vanish due to the reflection symmetry with respect to the reaction plane. The values of Fourier coefficients  $v_n$  characterize the azimuthal anisotropies. They are given by

$$v_n = \langle \cos(n(\phi - \psi_r)) \rangle. \quad (2.20)$$

where the brackets denotes an average value in a given kinematic window. The first Fourier coefficient  $v_1$ , which quantifies the *directed flow*, is determined by  $\langle p_x/p_t \rangle$  in a certain  $p_t$  and rapidity window. The sign of  $v_1$  indicates if this flow component is oriented along (+) or opposite to (-) the impact parameter vector. The second Fourier coefficient  $v_2$  represents the ellipticity of the particle distribution, referred as *elliptic flow*. A positive  $v_2$  indicates the major axis of the ellipse-like distribution lies in the reaction plane and is called *in-plane* flow. A negative  $v_2$  is for the case of the major axis perpendicular to the reaction plane and is commonly known as *squeeze-out*.

Nucleons are the major carriers of the flow signal. The proton directed flow has been extensively studied in a broad energy regimes. At AGS energy, the directed flow signals of proton and pion as a function of particle rapidity and transverse momentum have been also well studied by E877 experiment [42]. The rapidity dependence of the mean transverse momentum in the reaction plane  $\langle p_x \rangle$  is presented in Fig. 2.9. The proton exhibits a strong positive directed flow with a characteristic “S-shaped” dependence on rapidity in the semi-central Au+Au collisions. The charged pions exhibit an opposite but weak directed flow signal. These data are in good agreement with the predictions of the Relativistic Quantum Molecular Dynamics (RQMD) model [43] if the mean-field effects are taken into account.

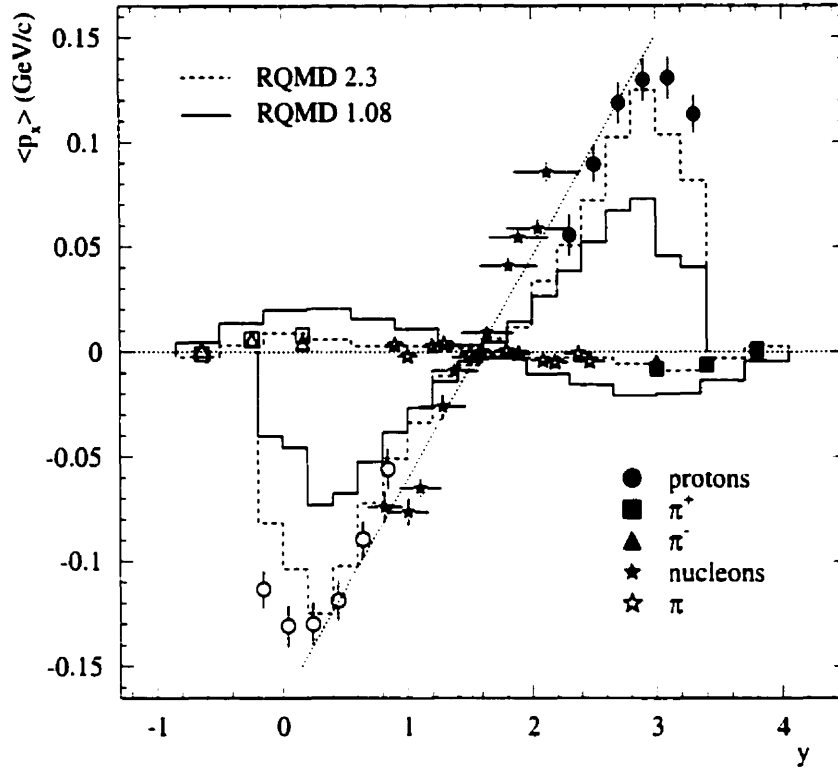


Figure 2.9: Mean  $\langle p_x \rangle$  of proton and pion transverse momentum onto the reaction plane as a function of rapidity in semi-central ( $\sigma_{top}/\sigma_{geo} = 9 - 13\%$ ) Au+Au collisions at AGS energies. Figure is taken from [42].

Unlike the flow of nucleons, the collective flow of strange particles carries distinctly different information. Due to their large mean-free path in nuclear matter, strange particles are predicted to be a sensitive probe of the dense nuclear medium [44, 45]. At Bevalac/SIS energies, both the EOS collaboration [46] and the FOPI collaboration [47] found that the  $\Lambda$  flow follows the flow of protons in light colliding systems. In contrast, the  $K^+$ , which are predominantly produced in association with the  $\Lambda$ 's,

show very little flow [47]. The in-medium effect has been introduced to describe the observed flow phenomena of kaon and lambda [44, 45]. The calculations of relativistic transport model indicate that the final-state interactions, especially the propagations in their mean-field potentials, lead to the significant difference between the  $K^+$  and the  $\Lambda$  flow [48]. At the AGS energies, the latest results on kaon flow [49, 50] shows that both  $K^+$  and  $K^-$  have a weak and negative flow signal. The directed flow of lambda hyperon will be presented in this thesis.

### 2.3.4 Hadron Yields and Strangeness

Particle ratios of hadron production can be employed to evaluate the degree of chemical equilibrium of the system. Assuming that the particles are emitted from locally thermalized source with a temperature  $T$ , the particle yield is expected to be given by [16]

$$\rho_i^0 = \frac{g_i}{2\pi^2} \int_0^\infty \frac{p^2 dp}{\exp[(E_i - \mu_b B_i - \mu_s S_i)/T] \pm 1} \quad (2.21)$$

where  $g_i$  is the spin-isospin degeneracy of particle  $i$ ,  $E_i$ ,  $B_i$  and  $S_i$  are its total energy in the local rest frame, baryon number and strangeness, and  $\mu_b$  and  $\mu_s$  are the baryon and strangeness chemical potentials.

Fig. 2.10 shows the systematics of the relative abundances of the produced hadrons observed at the AGS [17, 29]. The experimental data are compared to the model calculations from Eq. (2.21), and yield  $\mu_B = 540$  MeV and  $T = 120 - 140$  MeV with the system in nearly complete equilibrium. Similar analysis of the Pb+Pb data at the SPS, shown in Fig. 2.11, yield  $T = 170$  MeV and  $\mu_B = 280$  MeV with the system in chemical equilibration at the freeze-out stages [51].

The production of strange particles in nucleus-nucleus collisions is of particular interest as the heavy strange quarks do not exist prior to the collisions. It is predicted to be enhanced if a chiral phase transition occurs in dense and baryon-rich system.

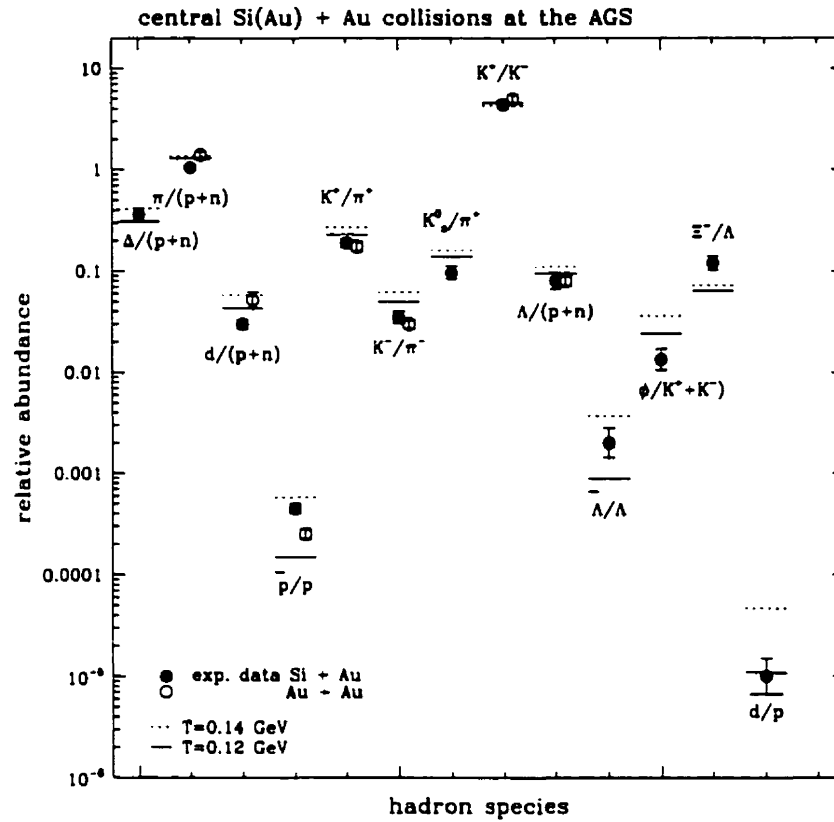


Figure 2.10: Hadron yield for central 14.6 A·GeV/c Si+Au and 11 A·GeV/c Au+Au collisions at the AGS compared to a thermal model calculation for two temperatures. Figure from [17].

Experimentally the strangeness enhancement has been observed at all available beam energies [52, 53]. At low (SIS) and intermediate (AGS) beam energies, the kaon to pion ratio in central Au+Au collisions increases with the number of the participating nucleons (centrality) while the  $K^-/K^+$  ratio is independent of the centrality of the collisions [54, 55].

Recently the preliminary excitation function of the  $K^+$  production in central Au+Au collisions has been reported [56, 57]. The  $K^+$  yields, which is expressed in

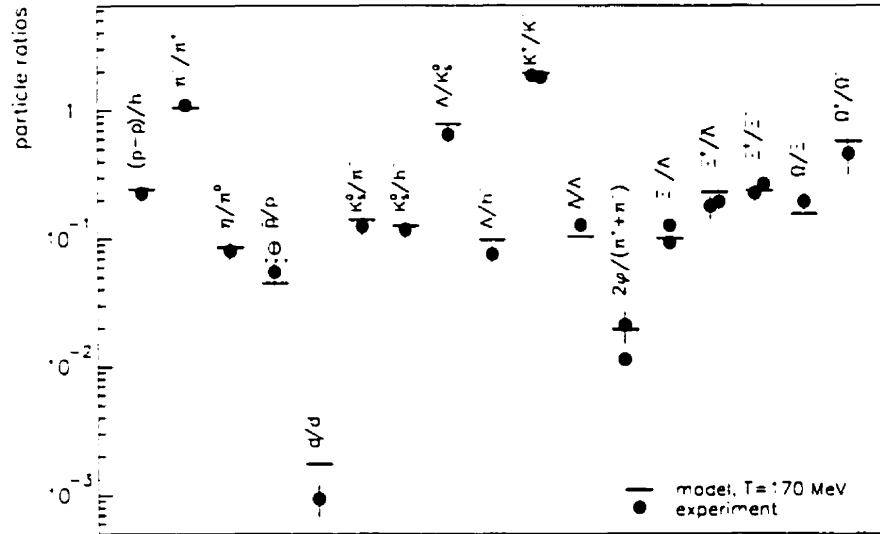


Figure 2.11: Hadron yield for central Pb+Pb collisions at 158 A-GeV/c at the AGS compared to a fit with a thermal model. Figure from [26].

terms of the ratio  $K^+/\pi^+$ , are plotted versus  $\sqrt{s}$  and shown in Fig. 2.12. The ratio increases steadily from near 3% at 2 A-GeV to 19% at 10.7 A-GeV. This observed energy dependence is in good agreement with predictions from the RQMD cascade model (v2.3) [43]. It seems that multiple secondary collisions, such as  $\Delta + N \rightarrow K\Lambda N$  etc. are responsible for the enhanced production of strangeness in the dense and baryon-rich fireballs. The basic argument is that at a highly dense baryon matter the mean-free path ( $\lambda = 1/\rho\sigma$ ) of hadrons becomes smaller than the typical size of a hadron so that the hadron can collide several times per 1 fm/c [56]. There is no consistent evidence for kaon in-medium properties at AGS energies [56].

However, the measured  $K^+/\pi^+$  from central Pb+Pb collisions at 158 A-GeV ( $\sqrt{s} = 17.2$  A-GeV) from the NA49 experiment [58, 59] is about 0.145, which is significantly below what is found in the measurement at the highest AGS energy and

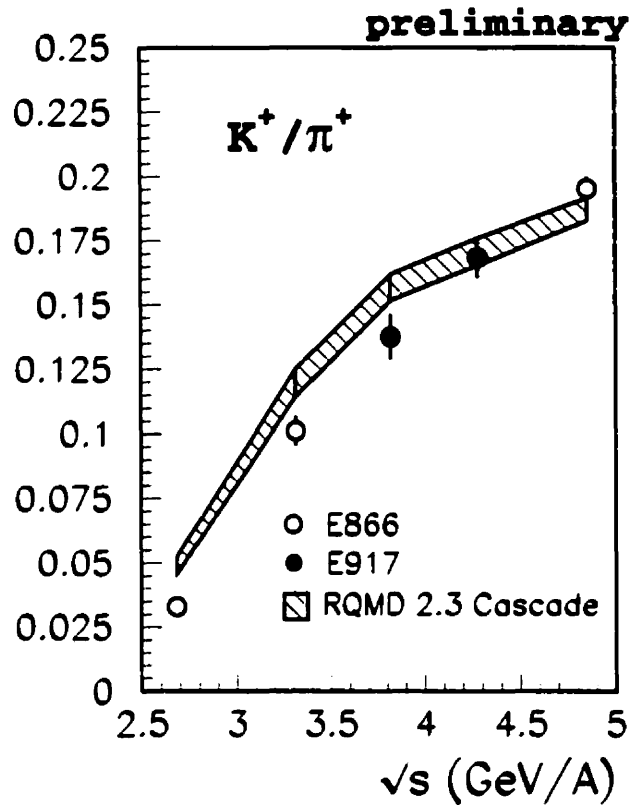


Figure 2.12: The energy dependence of the  $K^+/\pi^+$  ratio in central Au+Au collisions. Errors are statistical only. The hatched area correspond to predictions from the RQMD cascade model. The figure is taken from [57].

prompts the question: at which energy is the maximum reached and whether this might originate from a change of the kaon production mechanism.

## 2.4 Lambda Production

The object of this thesis is to study lambda production in central Au+Au collisions at the AGS. As discussed above, the results on kaon production from the E866 experiment have shown that the multiple secondary collisions play a major role in the

enhanced kaon production at the AGS energies [55, 56]. Since strangeness is conserved in strong interactions, lambda production is mainly associated with kaons. Therefore the data on lambda production are expected to complement the data on kaons.

At the AGS energies, nucleon-nucleon collisions play a main role in heavy-ion collisions. The open channels for  $\Lambda$  production are  $NN \rightarrow \Lambda KN$ ,  $NN \rightarrow \Lambda KN\pi$ , and  $NV \rightarrow \Sigma^{\circ}KV$  followed by  $\Sigma^{\circ} \rightarrow \Lambda\gamma$ . In a baryon-rich system, the lambda production can be enhanced by multiple secondary collisions, such as  $\pi + N \rightarrow K\Lambda$  and  $\Delta + N \rightarrow K\Lambda V$ , etc.

Strange particle production is expected to be a sensitive probe on the degree of equilibrium achieved in heavy-ion collisions [7]. Studying lambda spectra has several advantages over studying the spectra of protons and pions. Due to the suppression of the strangeness production in hadronic processes, lambda spectra should not have a colder component from the spectator as observed in the proton spectra [28]. Also unlike the  $\pi$  mesons the influence of baryon resonances on the shapes of lambda is expected to be negligible.

The measurement of the azimuthal anisotropies in lambda hyperon production is especially interesting as it is predicted to be sensitive to the in-medium properties of lambda hyperon in the dense nuclear matter [48]. At Bevalac/SIS energies, taking an attractive lambda potential into account, the experimental data of lambda flow can be well described. At higher energies (AGS and SPS), there is no data on lambda flow reported so far. We expect our data on lambda flow to provide valuable information for further studies of this physics issue.

## Chapter 3

# Experimental Setup

Experiment E877 is a fixed target experiment at the Alternating Gradient Synchrotron (AGS) of the Brookhaven National Laboratory (BNL). The goal of the E877 experiment is the study of the reaction mechanism of ultra-relativistic heavy ion collisions with heavy Au beams at energies around 11 GeV per nucleon. The data taking started in 1993 and continued until 1995. The data analyzed in this thesis are from the central Au+Au collisions at 11.5 GeV/nucleon taken in the winter of 1995.

A schematic view of the E877 experimental setup is illustrated in Fig. 3.1. It is an upgrade of the E814 apparatus to handle the large multiplicities of tracks produced in Au+Au collisions. The detector system can be divided into three sections according to their functions: 1) beam definition detectors; 2) a near  $4\pi$  coverage of calorimeters for global event characterization; 3) forward spectrometer for charged particle tracking and identification. Throughout the rest of the text, we employ a right handed coordinate system, with the longitudinal  $z$  direction along the beam direction, and the transverse  $x$  direction being vertical in Fig. 3.1.

In this chapter we will outline these detectors following above classification and justify their utilities as they were used in 1995 run. At last we will briefly discuss the

data collection of E877 experiment.

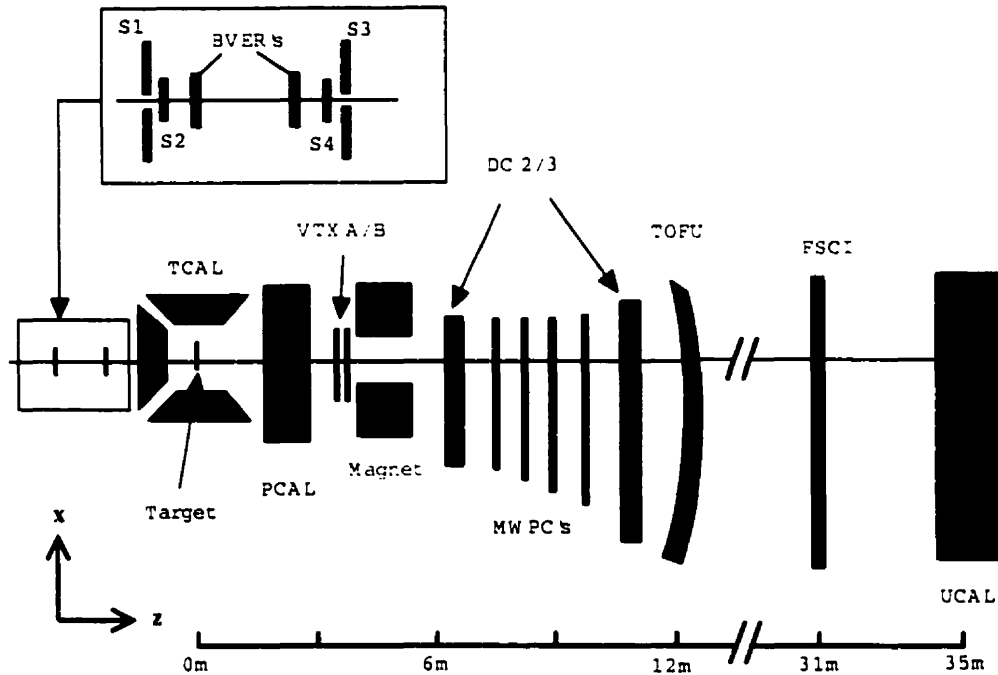


Figure 3.1: The E877 experimental setup for the 1995 run. Au beam is incident from the left.

### 3.1 Beam Definition Detectors

Since the momentum of a track in spectrometer is measured relative to the beam particle position and orientation at the target while the time-of-flight of a track is also relative to the time of collision, it is very important to measure accurately the beam profile on the target and provide a highly precise time reference. The beam definition detectors fulfill these tasks.

The group of beam definition detectors consists of four beam counters (S1-S4) and two beam vertex detectors(BVERs), shown on the inset of Fig. 3.1. They are

located upstream of the target. The beam counters are used to define a valid beam trigger and also provide the start time for the time-of-flight measurement while the BVER detectors are used to measure the incident beam trajectory.

- **Beam Scintillator Counters(BSCIs):** The four scintillator counters S1, S2, S3 and S4 together define a good beam profile at the target. This is achieved by using two donut-shaped counters (S1 and S3) as veto detectors. The S2 and S4 counters are slightly larger than the holes in S1 and S3. Thus a valid beam trigger is defined as the coincidence  $\overline{S1} \cdot S2 \cdot \overline{S3} \cdot S4$ . More details about the BSCIs can be found elsewhere [60, 61].

In the 1995 run, the S2 and S4 two scintillators were replaced by a set of Cherenkov counters equipped with fast phototubes to overcome the radiation damage from the heavy-ion beam. It has provided stable pulse height as a start signal to the time-of-flight measurement and better time resolution (45 psec). More details about the Cherenkov counters can be found in [61].

The pulse heights produced by an incident beam in S2 and S4 have been used to reject the double-beam events in the global event selection. This will be discussed in section 4.2.

- **Beam Vertex Detectors(BVERs):** Although the BSCI detectors provide a good-beam profile at the target, a higher precision of measurement on the beam particle position and orientation on the target is required in the determination of track momenta. Two silicon micro-strip wafers located between S2 and S4 are used for this purpose.

In the 1995 run, the BVERs were upgraded double-side silicon wafers with 200  $\mu\text{m}$  pitch in both the  $x$  and  $y$  axes. This allowed to measure the coordinates of beam particles in two dimensions and infer their position at the target

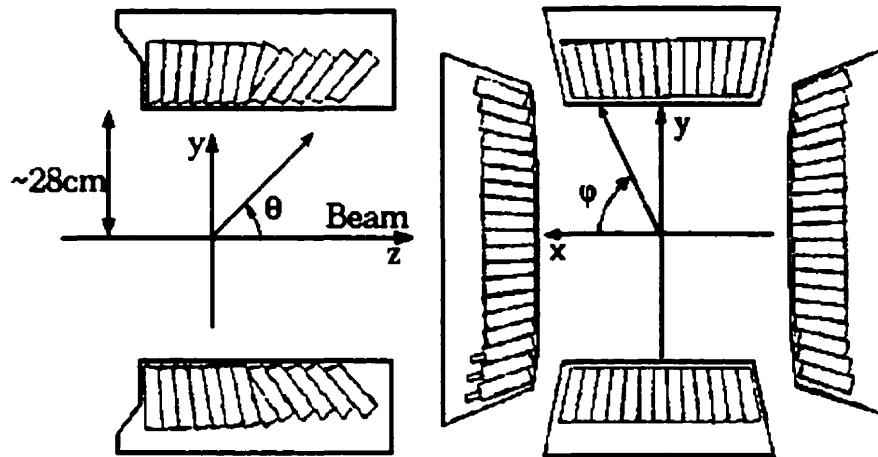


Figure 3.2: Side (left) and end (right) views of the TCAL.

with  $300\mu\text{m}$  position and  $60\mu\text{rad}$  angular resolution. The tracking efficiency throughout the run was better than 90%. More details on the BVERs upgrade and performance can be found in [21].

## 3.2 Detectors for event characterization

One of the main features of E877 setup is its nearly  $4\pi$  coverage of calorimeters, which consist in three parts: the target calorimeter (TCAL), the participant calorimeter (PCAL) and the uranium calorimeter (UCAL). The first two calorimeters are located in the target region and used to provide the global event characteristics, such as the centrality of the event and the reaction-plane orientation of the collision. Detailed discussions of the determinations of the centrality and reaction plane of the collision will be given in next chapter. Here we briefly describe these calorimeters.

- **Target Calorimeter (TCAL):** The TCAL is a set of four walls of electromagnetic calorimetry surrounding the target completely in the azimuthal direction. It consists of 832 NaI(Th) crystals which surround the target with a polar an-

gle coverage of  $48^\circ < \theta < 135^\circ$  (or  $-0.5 < \eta < 0.8$  in pseudo-rapidity). Each crystal has a depth of 13.8 cm, or about 5.3 radiation length (0.34 hadronic interaction length in equivalence). The signals from the crystals are readout by vacuum photodiodes that have a very stable response. The energy calibration was done using cosmic rays in 1993. More details on the TCAL can be found in L.S. Waters' PhD thesis [62].

The transverse energy measured by TCAL was used as the secondary triggers for coarse online event selection because of its high segmentation and stable performance. However, its relatively short radiation length limits its usefulness in large centrality event selection and the reaction plane determination.

- **Participant Calorimeter (PCAL):** The PCAL is a finely segmented Lead/Iron/Scintillator sampling calorimeter with a polar angle coverage of  $1^\circ < \theta < 47^\circ$  (or  $0.83 < \eta < 4.7$  in pseudorapidity). It consists of 16 azimuthal sections, 8 radial towers, and 4 depth sections and make a total of 512 cells in the whole device schematically shown in Fig. 3.3. Each cell is readout by wavelength shifting fibers guiding the light to photomultiplier tubes outside. A full description of the detector can be found in [63, 64, 65].

The PCAL was carefully recalibrated cell by cell with  $^{60}\text{Co}$   $\gamma$  source [66] in the 1995 run. Because its high segmentation and much lower energy leakage, the PCAL is used as the basis of the centrality measurement and the study of the reaction plane.

- **Uranium Calorimeter (UCAL):** The UCAL is a U/Cu/ scintillator sampling calorimeter, placed furthest downstream of the target at approximately 35 meters. It is designed to measure the energy of the forward particles, especially neutrons, with a resolution of about  $\Delta E/E \simeq 50\%/\sqrt{E}$ . It is composed of 20 modules lined up horizontally (perpendicular to the beam), and each

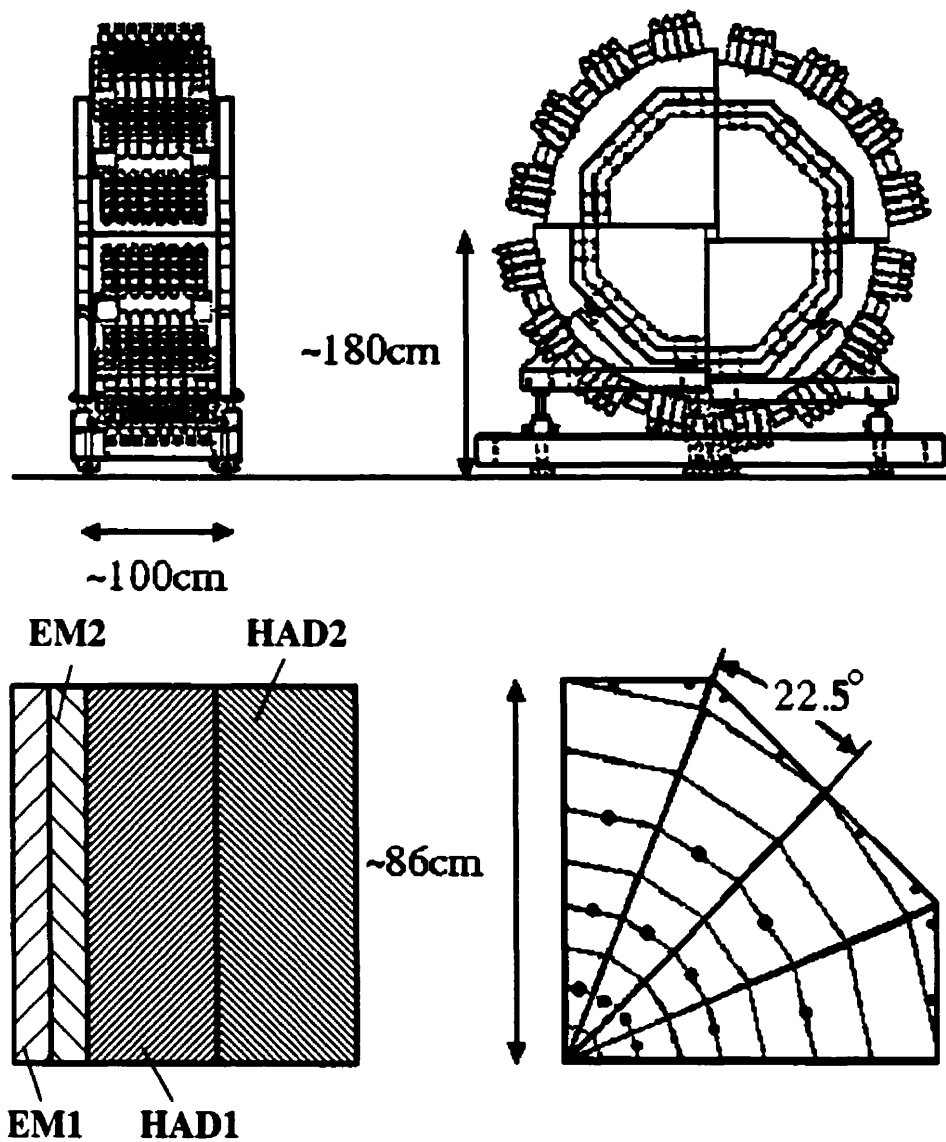


Figure 3.3: Side (upper-left) and end (upper-right) views of the PCAL along with schematic representations of the segmentation directly beneath.

module is segmented into 24 towers of  $10 \times 10 \text{ cm}^2$  cross sectional area. This results in an angular coverage relative to the target of  $-5.2^\circ < \theta_x < 1.3^\circ$  and  $-0.98^\circ < \theta_y < 0.98^\circ$ . A detail description of the detector can be found in [68]. It has not been used in the present analysis.

### 3.3 Forward Spectrometer

The other main component of the 877 experimental setup is its zero degree spectrometer. It is designed to identify charged hadronic particles ( $p, \pi^\pm, K^\pm$  and  $d$ ) and study their emission spectra down to very low transverse momentum ( $p_t$ ), even including  $p_t \sim 0 \text{ GeV}/c$ . The spectrometer is composed of a collimator, analyzing magnet, the upstream vertex chambers, the drift chambers, the multiwire proportional chambers, and the time-of-flight hodoscope. Below is a brief description of each component of the spectrometer.

- **Collimator:** The collimator, installed inside the PCAL opening, defines the geometric acceptance of the spectrometer. It has an opening of  $-115 \text{ mrad} < \theta_x < 15 \text{ mrad}$ , and  $-21 \text{ mrad} < \theta_y < 21 \text{ mrad}$ . The opening is asymmetric relative to the incident beam axis to maximize the acceptance in  $p_t$ .
- **Vertex Chambers (VTXA/B):** For the 1995 run, two identical highly segmented cathode pad detectors were instrumented and installed between the PCAL/collimator and the spectrometer magnet, shown in Fig. 3.4. They provide a precise measurement of the x-coordinate of the track before it is bent by the magnetic field. The addition of this upstream tracking information in 1995 run allows to reconstruct the decay vertices of the short lived particles such as  $\Lambda$ 's and improve the signal-to-background ratios for particle identification in the study of the rare particles such as kaons and antiprotons. The active area

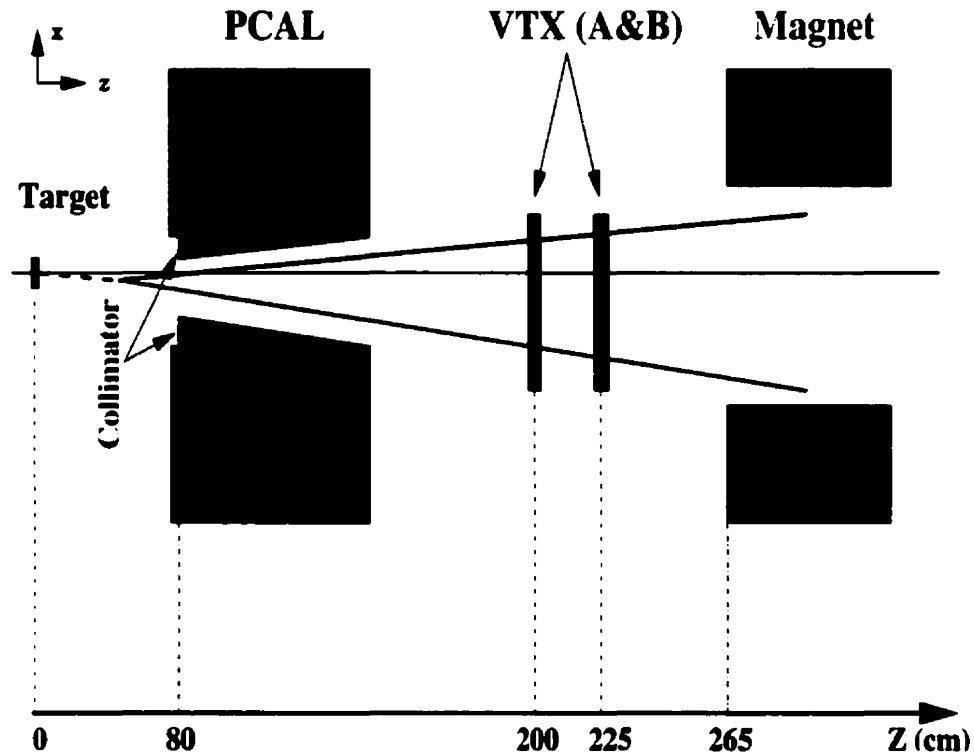


Figure 3.4: Schematic layout of upstream detectors of the spectrometer.

of each pad chamber consists of 10 rows of chevron shape pads with each row having 53 chevron shape pads and one anode wire placed above. The geometry of the chevron pad is shown in Fig. 3.5. The position resolution along the  $x$ -direction is about  $300 \mu\text{m}$ , the  $y$  resolution is determined by the wire spacing (5 mm). In the chevron-pad cathode plane, a  $1.9 \text{ cm} \times 2.8 \text{ cm}$  rectangle hole in the active region was made for the beam passage. This “beam hole” could affect the measurements of particles at low transverse momentum when the VTX chambers are included in the data analysis. A detailed description of the design, implementation and performance of the vertex chambers is given in [69].

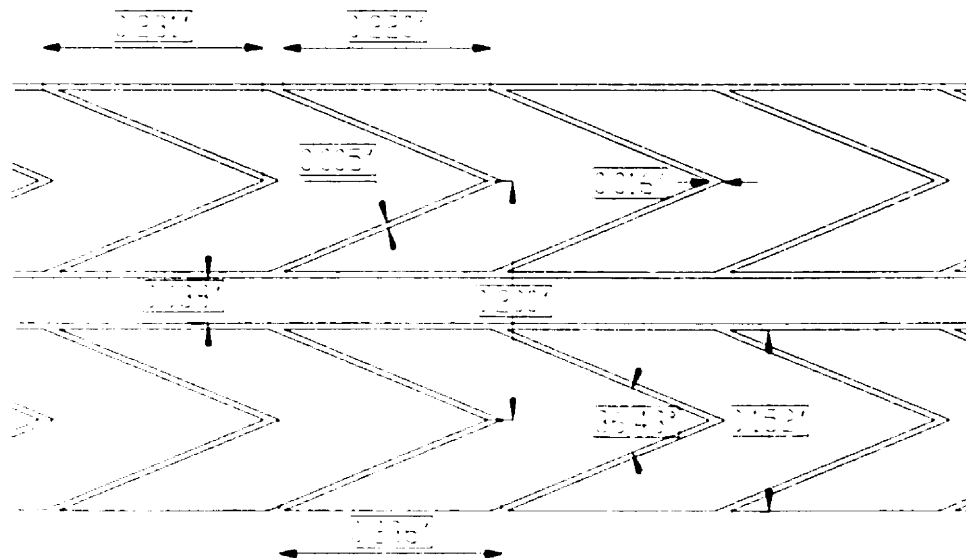


Figure 3.5: Zoom view of the chevron pattern geometry used in the vertex chambers. The dimensions are given in inches.

- **Magnet:** The analyzing dipole magnet is located 3 meters downstream of the target. Its field is perpendicular to the spectrometer plane and can be operated in either positive or negative polarity to selectively favor negatively or positively charged particles. The magnet is capable of generating a maximum field of  $\sim 2.2$  T and has an effective length of 1.045 m . In the 1995 run, a field value of  $-0.3353$  T was used which provided a better acceptance for negatively charged particles.
- **Drift Chambers (DC2/DC3):** Two drift chambers provide high resolution position measurements of the charged tracks. They are located at 5.4 m and 11.5 m downstream of the target. Both detectors are built in same fashion except that DC3 is twice as large as DC2. Each chamber is made up of a high resolution drift section and a low resolution pad plane. The drift section is composed of six parallel planes of alternating anode and cathode wires separated

by an aluminized mylar cathode sheet. A schematic layout of a section of the drift chambers is shown in Fig. 3.6. The anode wire spacing is 6.35 mm in DC2 and 12.7 mm in DC3. The mylar and the cathode wires are held at negative voltage while the anode are grounded. The signal from the anode wires provides the drift time measurements, from which we can deduce the distance traveled by an avalanche, hence determine the track position. Typically, the position resolution in the bending plane of the magnet is about  $300 \mu\text{m}$  ( $500 \mu\text{m}$ ) for DC2 (DC3). The cathode plane of each chamber is segmented into chevron-shaped pads running along the wire direction (perpendicular to the bending plane of the magnet). The pad plane is divided according to the expected particle multiplicity into several density regions. The  $y$ -coordinate of the track is reconstructed with a resolution depending on the pad density region: 2-15 mm in DC2 and 4-36 mm in DC3. For more detailed information regarding the drift chambers see [70].

- **Multiwire Proportional Chambers (MWPCs):** The four multiwire proportional chambers are installed between DC2 and DC3 to aid the tracking ability of the drift chambers and improve the the pattern recognition of the tracking system in the high multiplicity environment of Au+Au collisions. Each MWPC consists of a number of vertically strung anode wires spaced 5.08 mm apart. Each wire is instrumented with only a discriminator and, therefore, this detector has a position-resolution equal to the wire spacing. The detection efficiency of MWPCs is about 97% with three out of four planes required for track confirmation. In the fall of 1995, the MWPCs were also implemented with tracking trigger system to provide simple on-line tracking [71]. A detailed description of the MWPCs construction and operation can be found in [60].

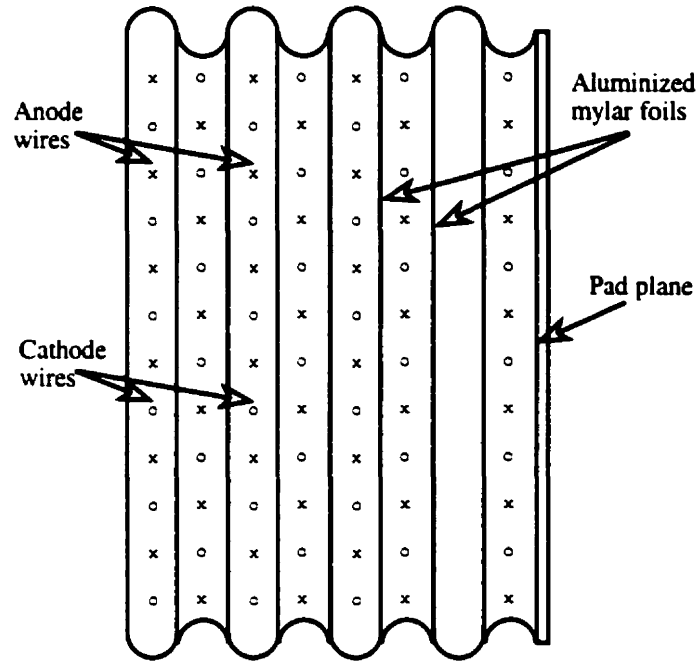


Figure 3.6: Layout of the drift chamber and pad plane.

- Time-of-Flight Hodoscope (TOFU):** The high granularity time-of-flight hodoscope provides a high precision measurement of the time-of-flight of the particle in the spectrometer. It is installed immediately behind the last tracking chamber (DC3). The hodoscope wall is comprised of about 150 scintillator slats having a full coverage of the projection area of the collimator aperture. Each slat is 70 cm long and 15 cm thick. The whole wall is divided into two density regions accommodating a higher occupancy of tracks near the beam. The high density section around beam is made of 39 slats with a width of 10 mm, and the rest of the hodoscope wall is assembled with wider (17 mm) slats. The photons produced in each scintillator are readout by two fast photomultipliers mounted on both ends. The overall time-of-flight resolution is about 85 ps. The pulse height information from both photomultipliers represents the energy loss of the particle in the scintillator and hence is used to determine the charge of

the particle. Besides charge and TOF measurements, a complementary vertical position of the track with a resolution of 1.8 cm is obtained by measuring the time difference between the photomultiplier signals at both ends of the counter. A complete description of the design, assembly and performance of the time-of-flight hodoscope is given in [28, 61].

- **Forward Scintillator (FSCI):** The FSCI is another time-of-flight hodoscope wall placed at about 31 meters downstream from the target. It consists of 39 vertical plastic scintillator slats, each 10 cm wide. The time-of-flight resolution of the forward scintillators is about 350 ps. The measurements from this detector have not been used in this analysis. More detail information about this detector can be found in [72].

### 3.4 Data Collection

The data from all detectors are collected in event-by-event mode. An event corresponds to a nuclear reaction. The data flow is controlled by the online trigger system. E877 experiment used a multilevel trigger system: beam trigger, pre-trigger, level-1 trigger and level-2 trigger. During the 1995 run, there were about 50 K beam particles per spill ( $\sim 1$  sec length every  $\sim 3.5$  sec) passing the beam trigger, which is defined by the logic of  $\overline{S1} \cdot S2 \cdot \overline{S3} \cdot S4$  from BSCI detectors. The thickness of the gold target is  $980 \text{ mg/cm}^2$  corresponding to about 2% of the Au interaction length. Thus there were about 1000 beam-target inelastic interactions in each spill. A pre-trigger requires a minimal energy (about 1 GeV) deposition in PCAL together with the presence of the beam trigger. The pre-trigger also issues the *START* signal for data sampling on each detector. The level-1 trigger serves as an "after-protection" to reject an event where another beam particle presents within  $1\mu\text{s}$  after this event.

The level-2 trigger analyzes each event that has passed above online selections, and decide if the event is interesting enough to write to tape or should be quickly discarded in order to liberate the precious DAQ time for those more interesting events. The level-2 trigger is based on the transverse energy (equivalent to the collision centrality) measured by TCAL and PCAL. Three preset thresholds are applied to the transverse energy  $E_t$  measurements, referred as TCAL1,2,3 and PCAL1,2,3. Since the higher of the centrality the more rare are the events, a down-scaling was employed to favor the more central events. The reconstruction of the unbiased  $E_T$  distributions will be discussed in the next chapter. In 1995 run, the TCAL1, PCAL1 and PCAL2 triggers were not used. The thresholds and downscale factors for the triggers used are listed in Table 3.1.

Table 3.1: Trigger thresholds and down-scaling factors in 1995.

	Beam Trigger	Pre-trigger	TCAL2	TCAL3	PCAL3
$E_t$ threshold (GeV)	0	2.8	5.5	12.5	240.
Downscale	4096	100	14-50	1	1
Centrality (%)	100	~ 50	~ 30	~ 10	~ 10

In 1995, the DAQ system of E877 experiment was substantially enhanced in both hardware and software so that it was able to handle up to  $\sim 200$  events per beam spill compared to  $\sim 60$  events per spill in 1994. The overall data statistics of 1995 run is nearly 5 times that of 1994 run. Detailed descriptions of the E877 trigger and data acquisition system can be found in [73, 71].

# Chapter 4

## Data Analysis

In this chapter we will discuss details of the offline data reduction and reconstruction. First we introduce the general procedure of the E877 data analysis, then we fully describe the event selection and characterization as well as the track reconstruction and properties. We have to understand well the properties of the spectrometer before moving on the  $\Lambda$ 's reconstruction. Thus the track finding algorithm, momentum determination and resolution, particle identification, background, occupancy and acceptance corrections as well as the estimation of the tracking efficiency will be discussed in detail.

### 4.1 Overview

The data presented here are from the last run of the E877 experiment in 1995. This was a long run lasting over two months. With an enhanced data acquisition system, we collected about 80 millions Au+Au events stored in event-by-event mode on nearly 400 8-mm magnetic tapes. The total amount of data exceeds 1000 GB. To cope with such huge amounts of data, a set of data reduction scheme has been developed. The data reduction procedure was done in two steps named STEP1 and STEP1.5.

STEP1 is the main data reduction/reconstruction package. It is used to unpack data from tape, calibrate the raw data on from each detector, implement the track finding algorithm and momentum determination, and output the reduced data in CWN ntuple format [75]. After this, the 1000 ~ 1600 GB of raw data is reduced to 54 GB of ntuple files.

The first ntuples, by design, contain as much information as possible so as to allow case studies for certain phenomena. It results in a large ntuple, which has 131 variables. We call it "fat" ntuple. The fat ntuples are still not convenient for daily physics analysis. To solve this the secondary data reduction package, STEP1.5 was therefore developed. In STEP1.5, the PCAL/TCAL transverse energies were calibrated into physics observables for each event, such as centrality and reaction plane orientation. Fine tuning of the time-of-flight measurement and the mass determination for particle identification were also done in STEP1.5. Occupancy correction from close track inefficiency were also included. Some event and track cuts have been simplified as flag bits. Thus the fat ntuple was reduced to lean ntuple, which only contains 50 variables. The total amount of lean ntuples is about 22 GB which can all be store in hard disks and is used for physics analysis.

## 4.2 Event Characterization

A collision between projectile and target nuclei is defined as an event in the experiment. As described in section 2.2, the initial conditions in heavy-ion collisions determine the properties of a collision, which can be characterized in terms of geometric overlap (centrality) and the azimuthal orientation (reaction plane angle). The study of particle production and azimuthal distribution dependence on centrality is an important probe of the dynamics of heavy-ion reactions. In the E877 experiment, the two global observables are deduced from the measurements of the transverse en-

ergy. In this section we will first present the general event selection, then discuss centrality and reaction-plane orientation determinations.

### 4.2.1 Event Selection

Although the online beam trigger selects events corresponding to good beam particles, it is not ensured that all the sampled events are good for physics analysis. A good event is one in which there is only one beam particle colliding with the target and producing a set of traceable tracks. We have to set more stringent selection criteria for event characterization in the offline data analysis. In particular, two types of unwanted events are eliminated from the data analysis, one is the *double-beam* events and the other is “blast” events.

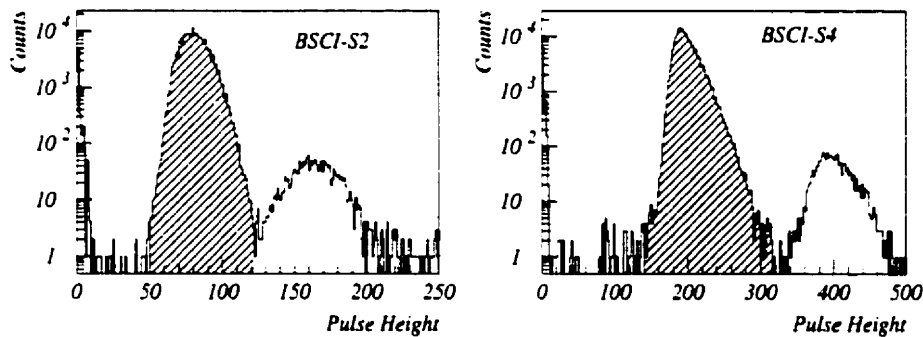


Figure 4.1: Typical pulse height distributions in BSCI S2 and S4. The hatched areas indicate the ranges for selecting good beam particles.

A *double-beam* event occurs when two incident beam particles arrive too close together in time. It can be removed by imposing certain cuts on the signals from the beam definition detectors. Fig. 4.1 presents the pulse height spectra produced by incident beam particles in BSCI S2 and S4. The spectra show a double hump.

The hatched hump corresponds to single beam particle whereas the second hump at higher pulse height corresponds to *double-beam* particle. In the analysis, we require the pulse height falling within the hatched range.

The *double-beam* particle also results in multiple clusters in the BVER detectors. A cluster is defined as a group of adjacent strips being fired [21]. Thus the number of clusters in each BVER detector was required to be equal to one in order to avoid ambiguities in the determination of the beam direction and suppress double beam events (see Fig. 4.2). There is evidently a strong correlation between the double beam events as identified in the various beam detectors.

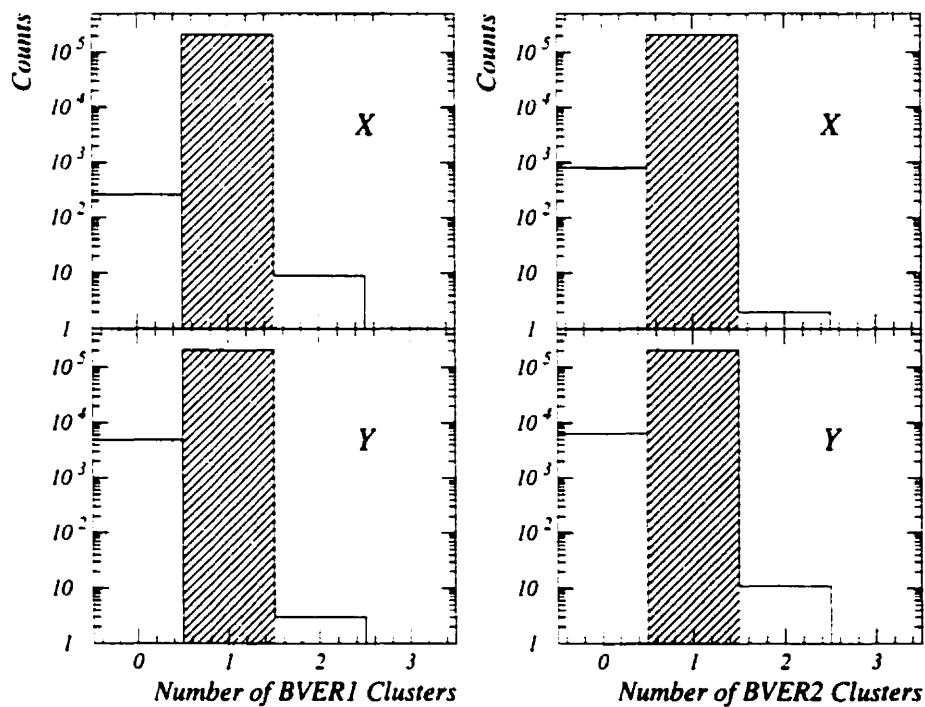


Figure 4.2: The number of clusters in the two BVERs in x and y directions. The hatched areas show the accepted events as single beam particle collision.

A “blast” event produces excessive track multiplicity in the forward spectrometer. The exact cause of this problem is not known but it can be due to those beam particles that do not interact with target, and could produce a large number of  $\delta$  rays entering the spectrometer. To remove the “blast” events, the number of hits in each MWPC was required to be less than 40 (see Fig. 4.3). There is a strong correlation between the hit multiplicity in each MWPC.

Combining all these event selection cuts, only about 85% of all events are kept as good events for physics analysis.

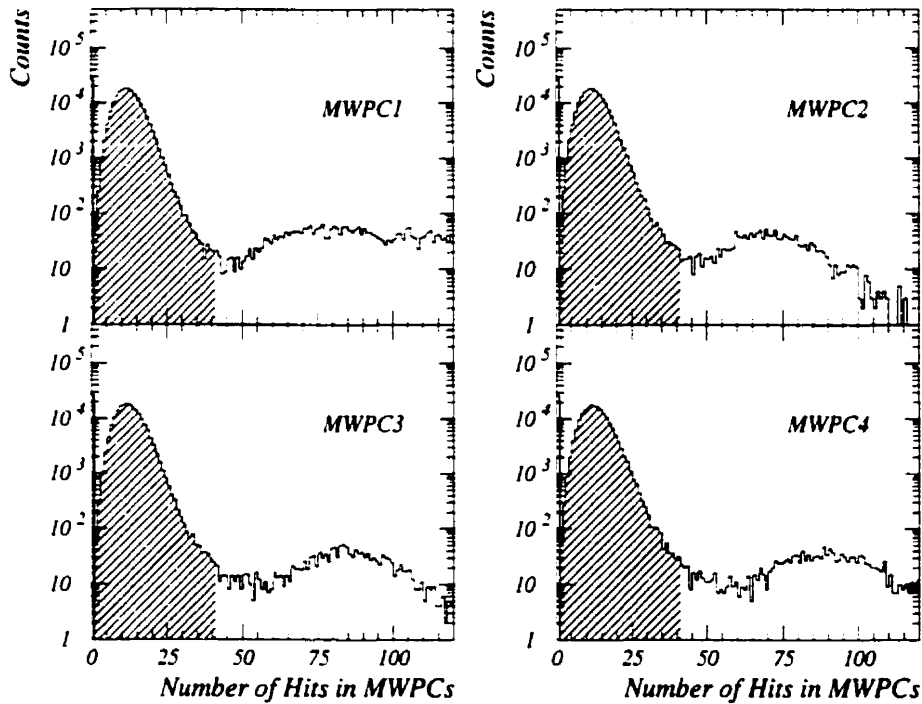


Figure 4.3: The number of hits in 4 MWPCs. The hatched areas indicate “non-blast” events. see text for explanation.

### 4.2.2 $E_T$ Distribution

Since the E877 experiment used a multilevel trigger scheme with down-scaling technique in the data sampling, it leads to a biased  $E_t$  distribution from the raw data. Thus, the process of deducing the centrality from the  $E_t$  is divided into two steps, first reconstructing the unbiased  $E_t$  distribution and the differential cross-section for  $E_t$  production, then inferring the centrality of the collision by using geometry model to estimate the total interaction cross-section.

The raw  $dN/dE_t$  distributions for TCAL and PCAL are shown in Fig. 4.4(a). They show step structure due to down-scaling factors in the triggers. The overall distributions are from logical ORs of all available triggers. The TCAL  $E_t$  trigger thresholds, down-scale and approximate fraction of cross-section are listed in Table 3.1. During the experimental run in 1995, the TCAL2 trigger down-scaling factor was changed from time to time, the others were kept constant. The data for TCAL3 and PCAL3 were not down-scaled since it is for the most central collisions in which we are interested.

The unbiased distribution of  $dN/dE_t$  can be reconstructed by combining the up-scaled distributions from beam trigger, pre-trigger and two TCAL  $E_t$  triggers in different  $E_t$  regions as shown in Fig. 4.4(b). TCAL3 covers the most central events, TCAL2 covers the mid-central events, the pre-trigger is for peripheral events and beam trigger is for the far peripheral events, which are difficult to reconstruct because of very low  $E_t$  production and the limits of the calorimeters. So the low  $E_t$  portion of  $dN/dE_t$  distribution has large uncertainties.

With the unbiased distribution of  $dN/dE_t$ , the absolute differential cross-section for  $E_t$  production can be obtain by

$$\frac{d\sigma}{dE_t} = \frac{1}{\rho_{tgt} \cdot \delta_{tgt} \cdot N_{beam}} \cdot \frac{dN}{dE_t}, \quad (4.1)$$

where  $\delta_{tgt} = 980 \text{ mg/cm}^2$  and  $\rho_{tgt} = 3.06 \times 10^{18} \text{ Au/mg}$  are the thickness and density

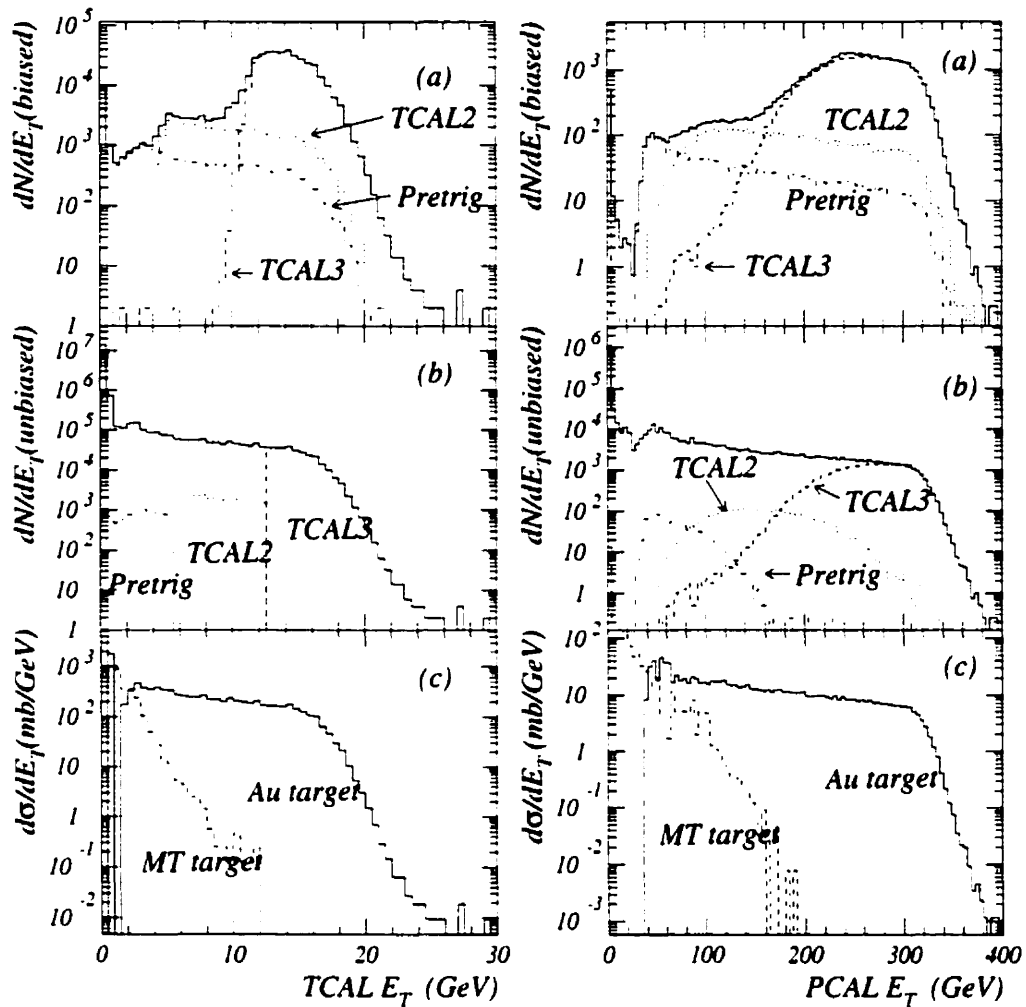


Figure 4.4: (a) Scaled down  $dN/dE_t$  distributions for TCAL and PCAL. (b) Unbiased  $dN/dE_t$  distributions for TCAL and PCAL after up-scaling correction. (c)  $E_t$  differential cross-section for Au target (solid line) and empty target (MT, dashed line). The solid line is the corrected  $d\sigma/dE_t$  after subtracting the MT target cross-section.

of the Au target, respectively.  $N_{beam}$  is the number of beam particles measured by the beam counters. In order to obtain the correct cross-sections, we have to subtract

the contribution from non-target interactions, which was measured with no target in place (Fig. 4.4(c)).

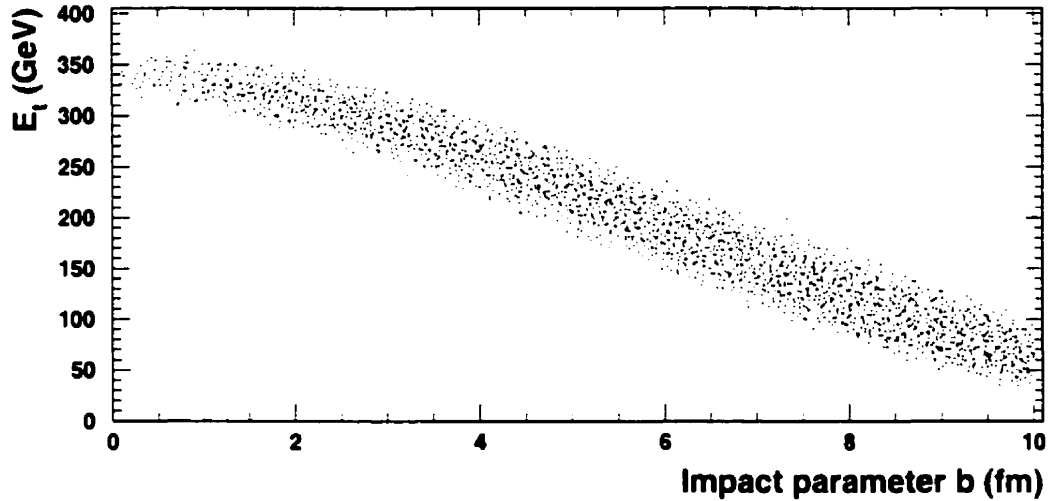


Figure 4.5: Calculated relation between impact parameter and total transverse energy from the RQMD model (v2.3) in cascade mode.

### 4.2.3 Centrality Determination

Centrality is one of the event characterizing observables, which quantifies the overlap of projectile and target nuclei, or violence of the collision. The geometric relationship between centrality and the impact parameter is described in Eq. 2.1. Unfortunately, the impact parameter is not directly measurable. However, it can be inferred from other measurable variables. Using a model as a guide, we can conclude that there is a strong anti-correlation between the impact parameter and the total transverse energy  $E_t$  ( Fig. 4.5). We thus can deduce the centrality of the collision from the total transverse energy measured by the calorimeters, the target calorimeter (TCAL) or the participant calorimeter (PCAL).

In theory, we can directly determine the centrality of the collisions from the  $d\sigma/dE_t$  distributions. However, due to the incomplete measurements of the  $d\sigma/dE_t$

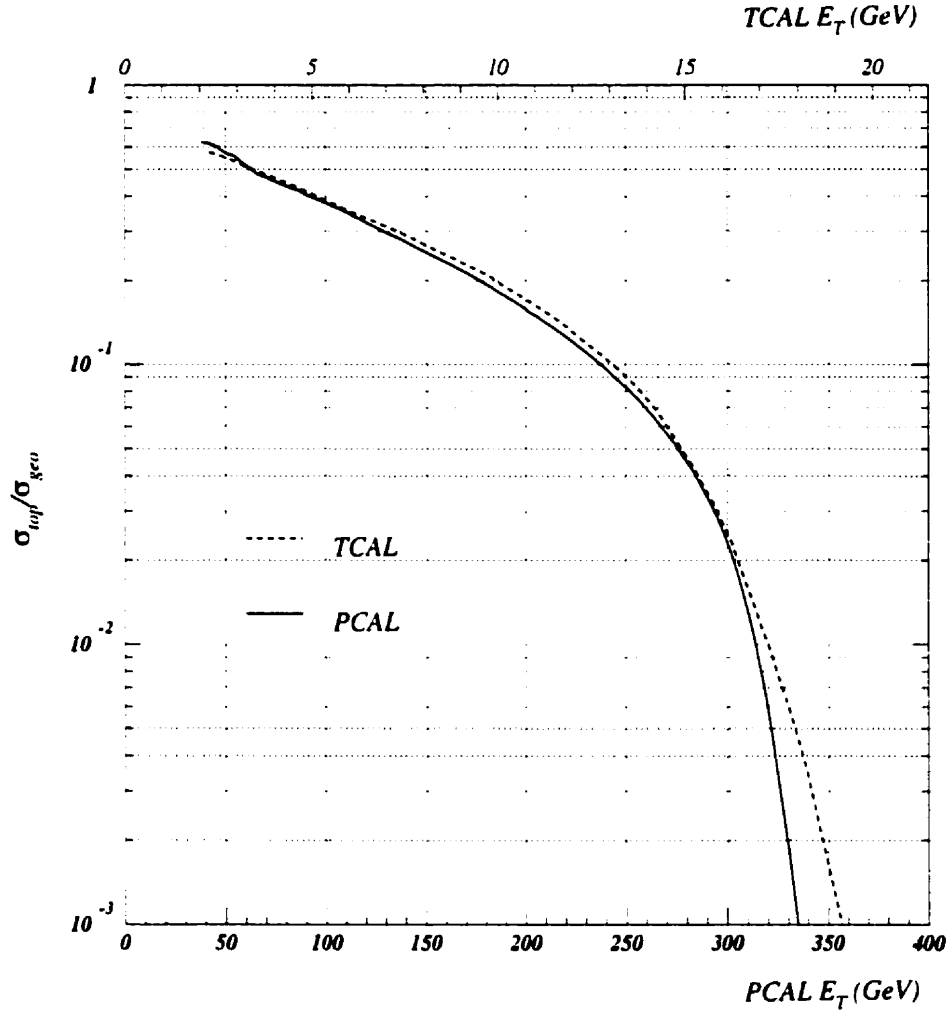


Figure 4.6: Centrality as a function of  $E_t$  for TCAL and PCAL.

distribution at low values of  $E_t$ , this distribution does not correspond to the total reaction cross-section. Instead, we use the calculated geometric cross-section  $\sigma_{geo}$ . Thus, the centrality of a collision is defined by the ratio of the most central interaction cross section  $\sigma_{top}$  to the geometric cross section  $\sigma_{geo}$ , given by

$$\frac{\sigma_{top}}{\sigma_{geo}}(E_t) = \frac{1}{\sigma_{geo}} \cdot \int_{E_t}^{\infty} \frac{d\sigma}{dE'_t} dE'_t. \quad (4.2)$$

where  $\sigma_{geo} = \pi(2R)^2$  with  $R = 1.2A^{1/3}$  and  $A=197$  for Au+Au collision. The determined centrality as a function of  $E_t$  measured in TCAL and PCAL is shown in Fig. 4.6.

Both calorimeters show consistent dependence, with PCAL being more sensitive in selecting the most central events. The relation between  $E_t$  and the centrality was done for each run to take into account run-to-run variations in the calibrated calorimeter energy scale.

In the present data analysis, the centrality cut is directly imposed on the  $\sigma_{top}/\sigma_{geo}$  instead of  $E_t$  in order to overcome the run-to-run variations of  $E_t$ .

#### 4.2.4 Reaction Plane Determination

The analysis of anisotropic transverse collective flow requires the determination of the reaction plane, which is defined by the impact parameter vector and the beam axis. The reaction plane orientation is measured using the energy deposition in the PCAL and TCAL calorimeters. Each calorimeter cell is used to construct the direction of the reaction plane by defining the following components of the transverse energy directivity vector  $\vec{D}_{E_t} = (D_x, D_y)$ :

$$D_x = \sum_{j=1}^N E_t^j \cos \phi_j^{lab}. \quad (4.3)$$

$$D_y = \sum_{j=1}^N E_t^j \sin \phi_j^{lab}. \quad (4.4)$$

where  $j$  is the index of the  $\phi$  section of the calorimeter and  $\phi_j^{lab}$  corresponds to its azimuthal angle measured in the laboratory frame.

The polar coverage of the two calorimeters is divided into four windows. The definition of windows in polar angle and pseudorapidity is given in Table 4.2.4. The reaction plane angle is independently determined in each window for every event and

Table 4.1: Definition of windows in polar angle and pseudorapidity for the determination of the reaction plane.

Window Name	TCW1	PCW2	PCW3	PCW4
$\theta_{lab}$	[117°, 53°]	[48°, 28°]	[28°, 15°]	[15°, 1°]
$\eta$	[-0.5, 0.7]	[0.8, 1.4]	[1.4, 2.0]	[2.0, 4.5]

given by:

$$\psi_r = \arctan\left(\frac{D_y}{D_x}\right). \quad (4.5)$$

The reaction plane resolution is evaluated by studying the correlation of  $\psi_r$  obtained in different windows. Details of this procedure can be found in [21, 22].

Ideally, the distribution of the directivity  $\vec{D}_E$  is supposed to be isotropic because of the randomness of the collisions geometry orientation. Consequently, a flat distribution in  $dN/dv_r$  is expected. However, due to non-uniform coverage and dead towers in the calorimeters, the measured  $dN/dv_r$  distributions are distorted. Thus a correction procedure to flatten the measured reaction plan distribution on an event-by-event basis has been developed. The detailed descriptions of the flattening techniques can be found in [21, 22].

### 4.3 Track Reconstruction and Properties

Since our data analysis for lambda production is performed on the reduced data (lean ntuples), we have to understand well the data reduction processes, especially the track reconstruction and properties in order to perform the lambda reconstruction from the secondary proton and pion tracks. In this section we will discuss in detail the track reconstruction in the data reduction packages and analyze track properties. First we introduce the track finding algorithm and momentum determination. The

momentum resolution of the E877 spectrometer will be modeled. Then we describe particle identification and background reduction in great detail, in which the role of VTX detectors will be discussed. The response of the VTX chambers will be modeled, too. The efficiency and corrections are given in the last section.

### 4.3.1 Track Finding Algorithm

The trajectories of the charged particles entering the spectrometer are reconstructed by the tracking software called "QUANAH", which is based on a tree-climbing algorithm. The principle of QUANAH will be briefly outlined here and more detail descriptions can be found in [30].

The track reconstruction starts with combining the wire hits in the wire planes of the drift chambers (DC2 and DC3) into *elements*, which give the x-information of particle hit. An element requires hits in at least 3 out of 6 wire-planes in a chamber. The neighboring elements are not allowed to share more than one hit wire. Each element is projected to the segmented pad-cathode plane of the chamber to look for pad hits called *clusters*, which give the y-information of particle hit. The clusters must associated with the closest wire plane *elements*.

Next, all possible combinations of linear paths connecting the *elements* in DC2 and DC3 are tested. Now the information from MPWC detectors is added into the testing to reject those combinations which along the path do not have associated hits in at least 3 out of 4 MWPCs. The remaining good combinations are stored as line *segments*. The segments that point back through the magnet aperture are promoted *candidates*. The candidates are further inspected if they have shared hits in the drift chambers or TOFU. Those that have such sharing are eliminated. Finally, the surviving candidates become *tracks*.

This method of track finding fails when the occupancy in the tracking detectors

(DC2/3, MWPCs) becomes too large. The occupancy increases with centrality. It was found that the tracking reconstruction efficiency of Quanah dropped rapidly with increasing centrality when the PCAL  $E_t < 150$  GeV [76, 66]. So we choose PCAL  $E_t > 150$  GeV (equivalent the centrality less than  $< 26\%$  of the geometric cross section) as the threshold for Quanah to start tracking in STEP1 data reconstruction. The estimation of the Quanah tracking efficiency will be discussed later in this chapter.

### 4.3.2 Momentum Determination and Resolution

The *track* reconstructed by QUANAH actually is just a portion of the particle trajectory downstream of the spectrometer magnet. In the basic implementation of QUANAH, determining the complete track is based on two assumptions; that the track originates from the target and that the track follows a circular trajectory in the analyzing magnetic field. The first assumption is fine for those particles like  $p, d, \pi^\pm$  and  $K^\pm$  directly produced in the collisions, but not good for the short-lived particles such as  $\Lambda$ . The effects of these assumptions on  $\Lambda$ 's reconstruction will be study in the next chapter. The second assumption requires to correct for the fringe effect of the magnetic field. It can be accurately accounted for by using an effective length slightly greater than the physical length of the magnet [76],  $\int_{-\infty}^{+\infty} B' \cdot dl = B \cdot L$ , where  $L$  is the effective length of the magnetic field  $B$ .

With these assumptions, we can make the following statements (see Fig. 4.7):

$$R(\sin \theta' - \sin \theta) = -L \quad (4.6)$$

$$x = z_1 \tan \theta \quad (4.7)$$

$$x' - x = R(\cos \theta' - \cos \theta), \quad (4.8)$$

where  $R$  is the radius of the circular curvature projected onto the bend plane;  $\theta$  and  $\theta'$  are the angles of the trajectory with the beam axis ( $z$ ) before and after the

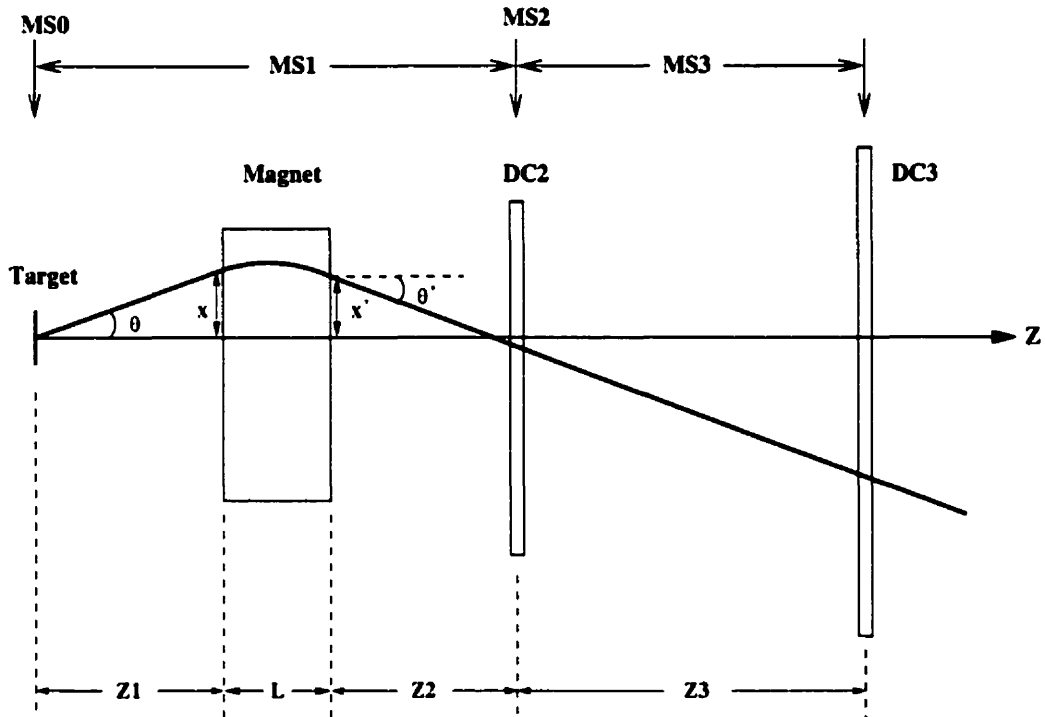


Figure 4.7: Bend-plane geometry of a track passing through the E877 spectrometer. The plot shows the projection on the  $x$ - $z$  plane.

magnet respectively.  $R > 0$  designates the case that a positively charged particle is deflected in the  $-x$  direction. In principle,  $R$  and  $\theta$  can be analytically determined from Eq. (4.7) and Eq. (4.8) with the measured values of  $x'$  and  $\theta'$ . They were actually numerically calculated using an iterative method. The rigidity of each track is then given by

$$\text{Rigidity} = \frac{p_{xz}}{Z} = eRB, \quad (4.9)$$

where  $p_{xz} = \sqrt{p_x^2 + p_z^2}$ ,  $Z$  is the charge of the particle and  $e$  stands for the unit charge.

With  $p_{xz}$  known, the momentum components of a track are obtained by

$$p_x = p_{xz} \sin(\theta - \theta_0) \quad (4.10)$$

$$p_z = p_{xz} \cos(\theta - \theta_0) \quad (4.11)$$

$$p_y = p_{xz} \tan(\phi - \phi_0) \quad (4.12)$$

where  $(\theta_o, \phi_o)$  are the incident beam angles on the target determined by the BVER detectors.  $\phi$  is the out-of-plane angle (between the trajectory and the bend-plane).

### • Momentum Resolution

The momentum resolution  $\sigma_p$  of the spectrometer is limited by the finite position resolution of the tracking detectors and multiple scattering of the particles. In principle, it can be written as

$$\left(\frac{\sigma_p}{p}\right)^2 = \left(\frac{\sigma_{p\theta}}{p}\right)^2 + \left(\frac{\sigma_{pMS}}{p}\right)^2 \quad (4.13)$$

where  $\sigma_{p\theta}$  is due to the finite position resolution of the tracking system, and  $\sigma_{pms}$  comes from multiple scattering.

Using the single bend model and the small angle approximation (see Fig. 4.7), the momentum of a track in the spectrometer is given by

$$p = \frac{0.3BL}{\theta' - \theta} \quad (4.14)$$

thus

$$\frac{\sigma_p}{p} = \frac{p}{0.3BL} \sigma_\theta \quad (4.15)$$

Where  $\sigma_\theta$  is the angular resolution of track.

Applying simple geometric relations, we can obtain  $\sigma_{p\theta}$  as

$$\sigma_{p\theta}^2 = \frac{4.06 \cdot 10^{-4} \sigma_{DC2}^2 + 8.84 \cdot 10^{-5} \sigma_{DC3}^2}{(BL)^2} \quad (4.16)$$

The multiple scattering effects of the spectrometer can be divided in four contributions ( $MS_0, MS_1, MS_2, MS_3$ ), shown in Fig. 4.7. Using Gaussian approximation, the small angle multiple scattering is given by [77]

$$\sigma_{\theta_{ms}} = \frac{0.0136Z}{\beta p} \cdot MS \quad (4.17)$$

where  $p$  is the particle's momentum in unit of GeV/c,  $\beta$  is particle's velocity in unit of  $c$ , and  $Z$  is the charge of the particle in unit of  $e$ .  $MS$  describes the thickness of the scattering medium which the particle traverses, given by

$$MS = \sqrt{\frac{x}{X_0}} \left( 1 + 0.038 \ln\left(\frac{x}{X_0}\right) \right) \quad (4.18)$$

Thus, we can parameterize the Eq. 4.13 as

$$\left(\frac{\sigma_p}{p}\right)^2 = (C_1 p)^2 + \left(\frac{C_2}{\beta}\right)^2 \quad (4.19)$$

where

$$C_1 = \frac{\sigma_\theta}{0.3BL} \quad (4.20)$$

$$C_2 = \frac{0.0136Z}{0.3BL} \sqrt{\frac{x}{X_0}} \left( 1 + 0.038 \ln\left(\frac{x}{X_0}\right) \right) \quad (4.21)$$

the  $C_1$  and  $C_2$  constants describe the intrinsic angular resolution and multiple scattering of the spectrometer. The values of the parameters containing in the evaluation of the resolution are summarized in Table 4.3.2.

Table 4.2: Parameters for momentum resolution of the spectrometer in 1995

$B$ (T)	$L$ (m)	$\sigma_{xdc2}$ (cm)	$\sigma_{xdc3}$ (cm)	$MS_0$	$MS_1$	$MS_2$	$MS_3$	$C_1$ $(GeV/c)^{-1}$	$C_2$
1.045	0.3353	0.030	0.060	0.27	0.91	0.083	0.044	0.0025	0.023

The momentum resolution achieved with the tracking system has been extensively studied [78, 73]. The results of three different calculations are compared in Fig. 4.8. a simple Monte-Carlo model (solid lines), an analytical calculation (dashed lines) and Gaussian fits performed on particles tracked after propagation in a detailed model of the spectrometer using GEANT (dots). The three results are found to be

quite consistent and show that the resolution is mainly determined by the multiple scattering in the spectrometer materials. The transverse momentum resolution is found to be approximately constant at  $\Delta p_x \sim 6$  MeV/c when the particle momentum is less than 4 GeV/c. The longitudinal momentum resolution varies from  $\Delta p_z/p \sim 0.02$  to 0.04 depending on particle type.

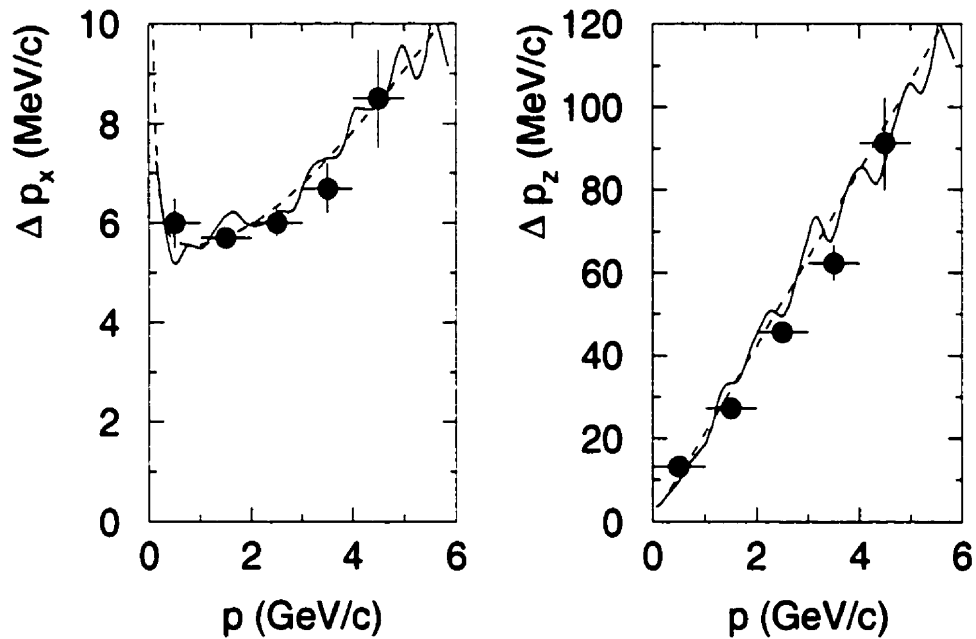


Figure 4.8: Spectrometer momentum resolution. The momentum resolution in  $p_x$  and  $p_z$  are plotted as a function of total momentum for pions. Figure taken from [78].

### 4.3.3 Charge Separation

The time-of flight hodoscope performs measurements of not only the time-of-flight but also the pulse height of the charged track. The pulse height (PH) produced by a particle traversing a scintillator is expressed as

$$PH = \sqrt{ph_1 \cdot ph_2} \quad (4.22)$$

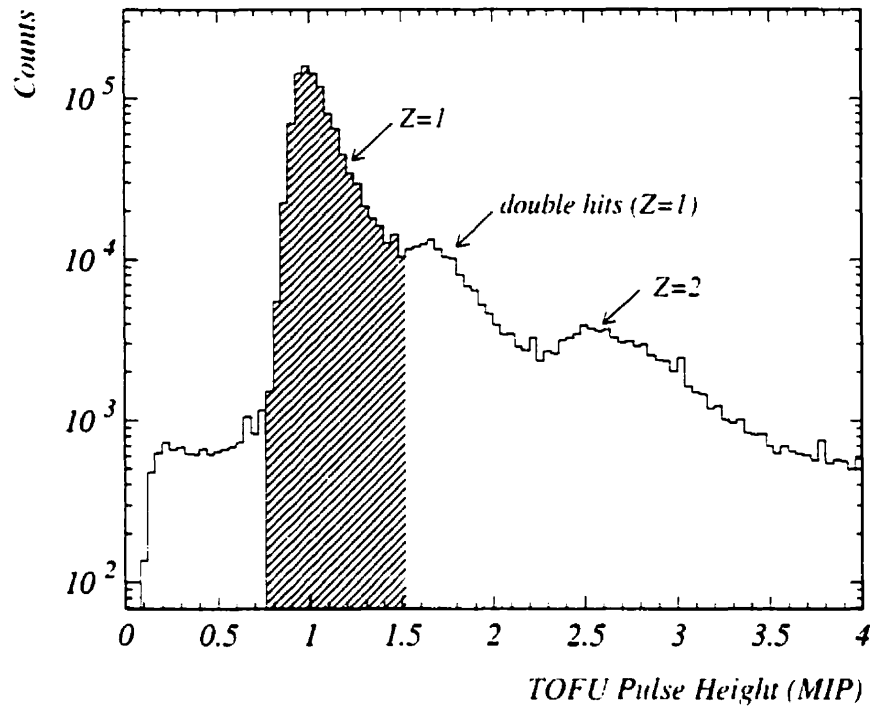


Figure 4.9: Pulse height distribution in TOFU. The pulse height is normalized to the unit of minimized ionization particle (MIP). The shaded region is the selection range of single charged tracks.

where  $ph_1$  and  $ph_2$  are the individual photomultiplier pulse heights at both ends of the scintillator. The total pulse height (PH) is directly proportional to the deposited energy,  $\Delta E$ . The energy deposit per unit of length ( $dE/dx$ ) is described by the Bethe-Bloch formula [79]. It is proportional to

$$\frac{dE}{dx} \propto \frac{z^2}{\beta^2} \quad (4.23)$$

For relativistic particle,  $\beta$  is close to  $c$ . Thus the pulse height distribution is simply proportional to  $z^2$ . The feature of pulse height distribution was used to make a coarse

separation of the charge state of a track.

A typical pulse height distribution is shown in Fig. 4.9. The distribution has been normalized by the peak pulse height of a minimized ionization particle (MIP). The first peak at 1.0 MIP corresponds to the detection of single  $Z = 1$  particles, the second peak at 1.6 MIP corresponds to the pile-up of two  $Z = 1$  particles, and the third peak at 2.4 MIP corresponds to the detection of  $Z = 2$  particles. In the present analysis, a cut on the pulse height distribution in a range from 0.75 to 1.5 was used to select single charged track.

#### 4.3.4 Particle Identification

A simultaneous measurement of the momentum and the time-of-flight of each track allows the identification of particle species. In this section we first introduce the TOF measurement, then describe the particle identification by square mass, and last discuss the mass resolution and PID cut.

##### • Time-of-flight Measurement

The time-of-flight hodoscope wall was designed to achieved a high precision of time-of-flight (TOF) measurement. The TOF of a particle from target to a hodoscope counter is expressed as:

$$\text{TOF} = \frac{(t_{top} + t_{bottom})}{2} - t_{start} - T_0 \quad (4.24)$$

where  $t_{top}$  and  $t_{bottom}$  are the stop times measured by the top and bottom phototubes of the hodoscope counter,  $t_{start}$  is the start time measurement given by the beam counters, and  $T_0$  is the time offset to be determined for each counter of the hodoscope. The start time resolution provided by the beam counters was carefully analyzed and estimated to be better than 25 ps [21]. The time offsets  $T_0$  were obtained by analyzing

the mean of the time distribution for each slat. The shifts from the mean value were determined and corrected for during the ntuple production stage.

To achieve the best possible resolution, all the time measurements need to be carefully calibrated. A number of different corrections were also taken into account. A complete description of the calibration procedure and performance can be found in [28]. An average time resolution of 85 ps has been obtained over the entire hodoscope wall.

### • Mass resolution

Combining the measurements of momentum and time-of-flight for each track, the species of a particle can be identified by its squared mass  $m^2$

$$m^2 = p^2 \left( \frac{1}{\beta^2} - 1 \right) = p^2 \left\{ \left( \frac{TOF}{L} \right)^2 - 1 \right\} \quad (4.25)$$

where  $p$  is the measured momentum, TOF is the time-of-flight,  $L$  is the flight path length determined from the tracking information. In Fig. 4.10 we show a scattering plot of the inverse momentum  $1/p$  versus the inverse of the measured velocity  $1/\beta$  for  $Z=1$  particles produced in central Au+Au collisions. The bands represent different particles separated according to their masses. The resolution is good at low momenta and gradually deteriorates with increasing momentum.

According to the Eq. (4.25), the experimental resolution of mass measurement is limited by the momentum resolution and the time resolution of time-of-flight. Using the parameterizing momentum resolution (Eq. 4.13), the total mass resolution can be approximated by [80]

$$\sigma_{m^2}^2 = 4m_0^4 \left( \frac{\sigma_p}{p} \right)^2 + \frac{4p^4}{\beta^2} \left( \frac{\sigma_{TOF}}{L} \right)^2 \quad (4.26)$$

where  $C_3 = \sigma_{TOF}/L$ .

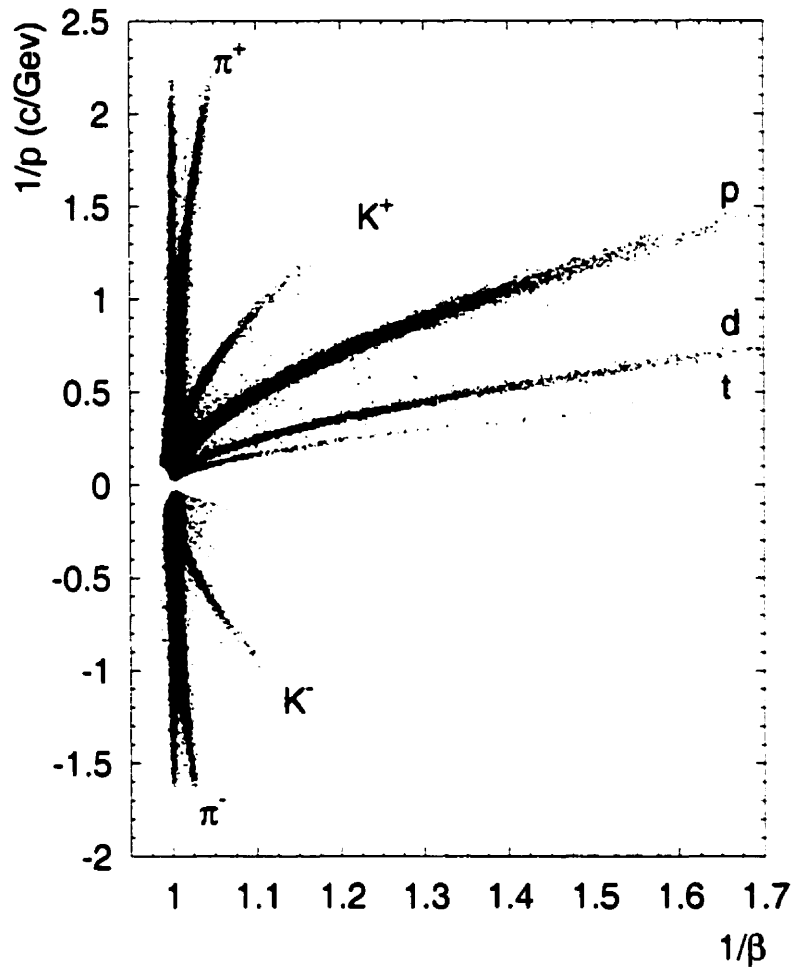


Figure 4.10: Scatter plot of the inverse momentum  $1/p$  versus the inverse of the measured velocity  $1/\beta$  for  $Z=1$  particles produced in central Au+Au collisions at 11.5 GeV/c. The figure is taken from [61].

To study the various contributions, the distribution of  $m^2$  versus  $p$  was sliced into many momentum windows. For each slice, the squared mass distribution was fitted with Gaussian. The extracted widths of  $m^2$  as a function of momentum for

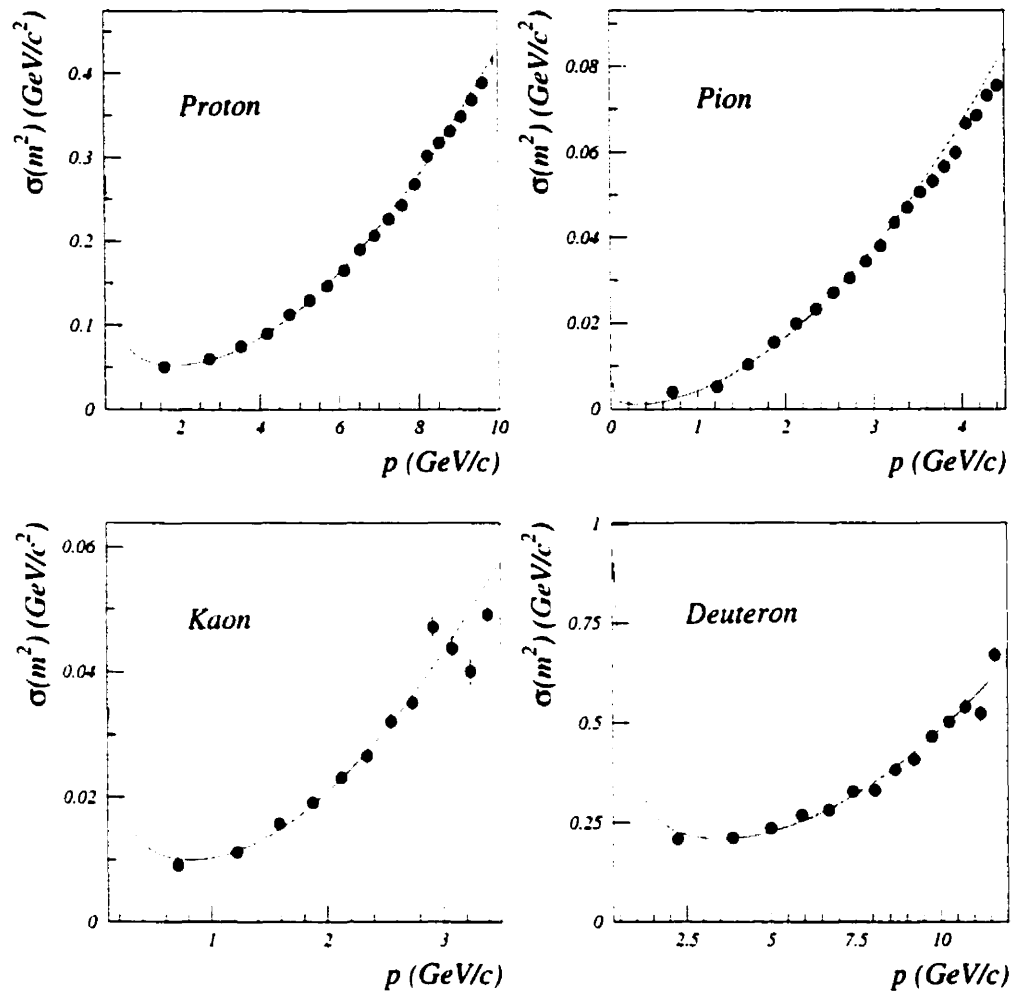


Figure 4.11: Squared mass resolution as a function of momentum for for proton, pion, kaon and deuteron. The solid-line is the fitting with Eq. (4.26). The figure is taken from [21] and represents the standard offline definition of the particle identification for E877.

different particle species is shown in Fig. 4.11. The dependence of the widths of  $m^2$  on momentum was fitted with Eq. (4.26). The  $C_1$  parameter was fixed at the estimated value of  $0.0025 (\text{GeV}/c)^{-1}$  (see Table 4.3.2). The values of the fit parameters are

summarized in Table 4.3 for each particles.

Table 4.3: The fit parameters of the squared-mass peak for different particles. Eq.( 4.26) was used in the fitting with  $C_1$  fixed.

Particle	$C_1(\text{GeV}/c)^{-1}$	$C_2(\text{GeV}/c^2)$	$C_3(c^{-1})$	$\sigma_{TOF}(ps)$
Proton	0.0025	0.027	0.0021	84
Pion	0.0025	0.025	0.0021	84
Kaon	0.0025	0.017	0.0021	85
Deuteron	0.0025	0.026	0.0020	80

#### • PID Cuts

The assignment of the particle identification (PID) for a track was performed by making two dimensional cuts in the momentum versus squared mass distribution. The basic selection criteria is

$$|m^2 - m_i^2| < 1.5\sigma_{m^2} \quad (4.27)$$

where  $m^2$  is the measured squared mass,  $m_i^2$  is the peak value of the  $m^2$  distribution for that particle and  $\sigma_{m^2}$  is calculated from Eq. 4.26 for each particle species. The cuts are displayed in Fig. 4.12. In addition, we also require  $m^2$  is  $2.5\sigma_{m^2}$  from the neighboring particle species. As shown in Fig. 4.12, the particle identification becomes ambiguous even fail in the high momentum region. So we also impose the maximum momentum cuts, which are summarized in Table 4.4. In the present data analysis, the maximum momentum cuts for proton and  $\pi^+$  are set relatively high so that some contaminations are present. In order to remove these contaminations, some extra cuts have been added (see Fig. 4.12). The PID cut efficiency will be discussed in the last section of this chapter.

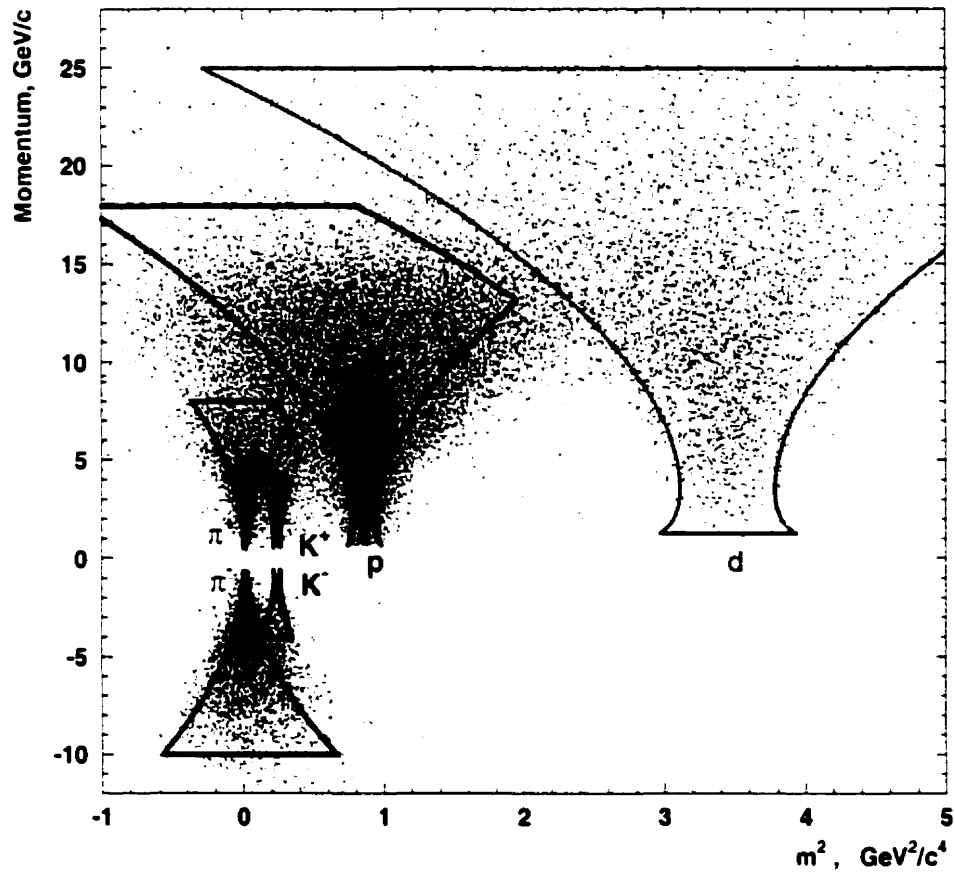


Figure 4.12: Scattering plot of momentum versus squared mass with PID cuts shown by solid lines.

Table 4.4: Maximum momentum cuts for different particles.

particle	$\pi^+$	$\pi^-$	$K^+$	$K^-$	$p$	$d$
$p_{max}$ , GeV/c	8.7	10.0	4.5	4.5	18.0	25.0

## 4.4 Background Reduction

The quality of the particle identification can be improved using the tracking information from the upstream VTX detectors. Especially for studying the low-yield particle production such as kaon and antiproton, the background reduction become indispensable. In this section, we will discuss how to use these additional tracking information to improve the signal-to-background ratio for particle identification.

### 4.4.1 Track Matching on VTX Chambers

The two vertex pad chambers provide the upstream tracking information between the target and the magnet. We can use this information either to remove the background tracks not originating from the target or to reconstruct the secondary decay vertices of short lived particles such as  $\Lambda$ 's. Here we will discuss its background reduction function. Its second function will be discussed in the next chapter.

In principle, a position information from the vertex chambers should be associated with each track. The difference between a track calculated position and its measured position in VTXA and VTXB is given by

$$dx^{(i)} = x^{(i)} - (z^{(i)} \cdot \tan \theta + x_{tgt}) \quad i = A, B \quad (4.28)$$

$$dy^{(i)} = y^{(i)} - (z^{(i)} \cdot \tan \phi + y_{tgt}) \quad i = A, B \quad (4.29)$$

where  $(x^{(i)}, y^{(i)})(i = A, B)$  represents the position measured by VTX- $i$ ,  $z^{(i)}$  ( $i = A, B$ ) is the  $z$  position of the VTX- $i$  with respect to the target,  $\theta$  is the emission angle of a

reconstructed track in the  $x$ - $z$  plane,  $\phi$  is the out-of-plane angle,  $x_{tgt}$  and  $y_{tgt}$  is the  $(x, y)$  position of the incident beam particle at the target.

The VTXA dx versus the VTXB dx shows a strong correlation seen in Fig. 4.13(a). To parameterize this correlation, we rotate the data from  $(dx_{VTXA}, dx_{VTXB})$  to another set of orthogonal axes  $(dx_{narrow}, dx_{wide})$ :

$$dx_{narrow} = \cos\alpha \cdot dx_{VTXB} - \sin\alpha \cdot dx_{VTXA} \quad (4.30)$$

$$dx_{wide} = \sin\alpha \cdot dx_{VTXB} + \cos\alpha \cdot dx_{VTXA} \quad (4.31)$$

where  $\alpha$  is the rotation angle to make the observed band vertical. The rotation angle  $\alpha$  is about  $47.5^\circ$ . Thus the observed correlation between VTXA\_dx and VTXB\_dx is decoupled into two components. The narrow component shows a nearly constant width with respect to momentum (Fig. 4.13(b)), which mainly due to the intrinsic x resolution of the chambers while the wide component exhibits a broad distribution with very strong momentum dependence (Fig. 4.13(c)) which indicates the dominant influence from the multiple scattering in the E877 spectrometer. The  $dx_{narrow}$  and the  $dx_{wide}$  are divided into momentum slices. The distribution in each slice is then fitted to the sum of three Gaussians. The main and highest Gaussian peak is the true random distribution of error in cluster properly associated to the given track. The other Gaussians are very broad and correspond to a random distribution of uncorrelated hits. The widths of the main Gaussian are then parameterized as a function of  $1/p$ , typical momentum dependence of multiple scattering. The fit results are shown in Fig. 4.13(d). The fit parameters are:

$$\sigma_{narrow} = 227.7 + 75.0/p \quad (4.32)$$

$$\sigma_{wide} = 344.5 + 2379.4/p \quad (4.33)$$

The x resolution of the vertex chambers is around  $230\mu m$ . Then we can rotate back to the  $(dx_{VTXA}, dx_{VTXB})$  axes and parameterize the responses of the VTX detectors

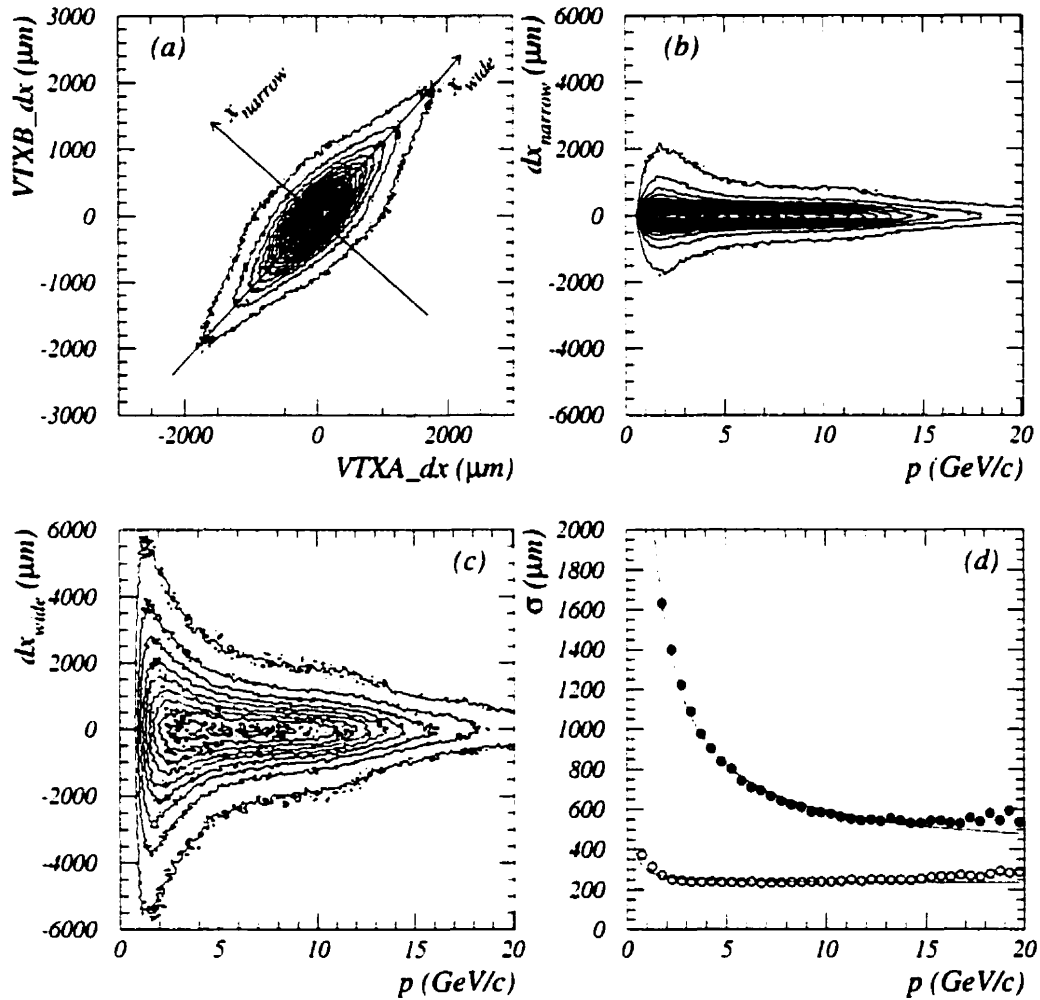


Figure 4.13: Track matching at vertex chambers. (a) shows the correlation between the measured VTXA dx and VTXB dx; (b) and (c) show the contour plots of the decoupled  $dx_{\text{narrow}}$  and  $dx_{\text{wide}}$  versus momentum of track the  $x_{\text{narrow}}$  and  $x_{\text{wide}}$ ; (d) presents the momentum dependences of the  $dx_{\text{narrow}}$  width (open circles) and  $x_{\text{wide}}$  width (solid circles).

by

$$\sigma_{VTXA} = \sqrt{(\sigma_{wide} \sin \alpha)^2 + (\sigma_{narrow} \cos \alpha)^2} \quad (4.34)$$

$$\sigma_{VTXB} = \sqrt{(\sigma_{wide} \cos \alpha)^2 + (\sigma_{narrow} \sin \alpha)^2} \quad (4.35)$$

Thus for any given track with momentum  $p$ , we can calculate the  $\sigma_{VTXA}$  and  $\sigma_{VTXB}$ .

#### 4.4.2 VTX Cut

The track matching cuts on the vertex detectors, called VTX cuts, are performed by requiring the track associations (VTXA dx and/or VTXB dx) falling within a number of  $\sigma_{VTXA}$  and/or  $\sigma_{VTXB}$ . The application of these cuts reduces a lot backgrounds due to tracks not originating from the target. This is illustrated in Fig. 4.14. On the left panel, the raw data is presented. The right plot shows the same data requiring the VTX cut from either of the two VTX chambers. It is clear that the VTX cut has significantly reduced the background tracks which do not fall in any of the mass bands so that the separation between pion and kaon becomes significantly better. Therefore the VTX cut is definitely needed to study the rare particle production such as kaon and antiproton. Nevertheless, the VTX cut also discards of a lot good tracks because there exists dead areas for beam passages in both chambers and particles passing these regions do not have any VTX information. These dead zones are most harmful for the low  $p_t$  particles. It can completely cut off the low  $p_t$  particles around the beam rapidity. In order to keep the low  $p_t$  coverage of the forward spectrometer, we don't impose any VTX cuts on the analysis of protons and pions since they are most abundant production and the background relatively small.

Since the VTX cut not only discards background tracks, but also throws away good tracks, the justification of VTX cut has to be evaluated. This depends on the statistics needed and the level of background that can be tolerated. It is also

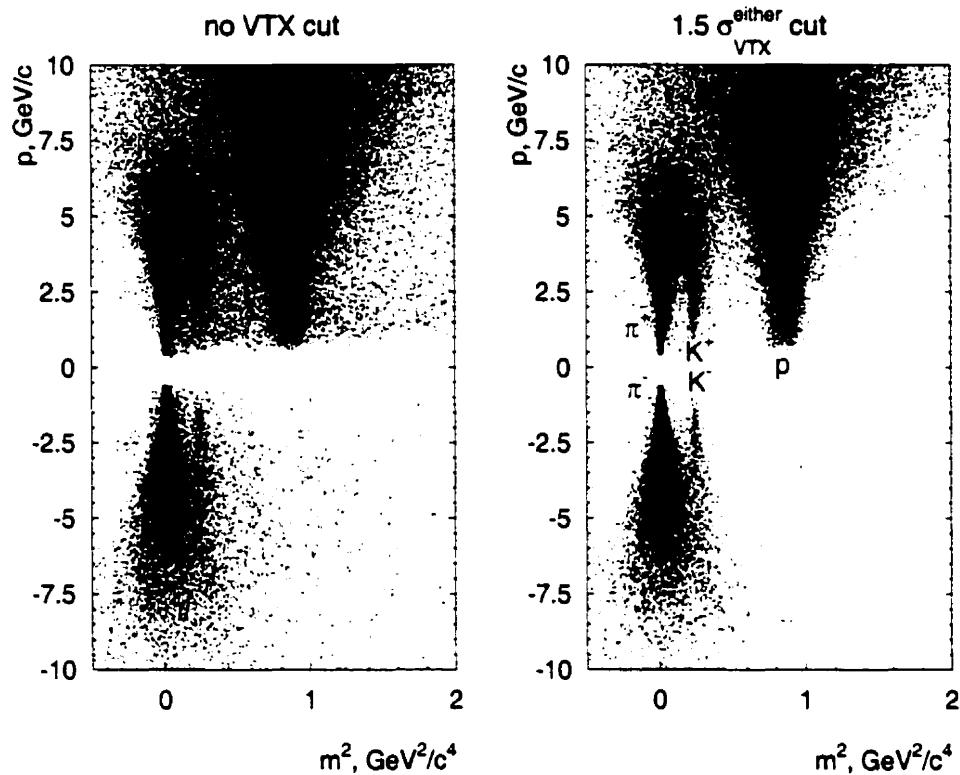


Figure 4.14: Particle identification plot without vertex chamber confirmation (left panel) and with  $1.5\sigma_{VTX}^{\text{either}}$  cut applied to confirm the track (right panel).

dependent of the specific physics analysis being performed. More details can be found in [76, 66, 21].

## 4.5 Efficiency and Corrections

Since a variety of cuts have been applied during the data analysis, we have to estimate the efficiency of each cut. Some correction procedures have to be added into the data analysis in order to obtain absolute cross section. In this section, we discuss the tracking efficiency and the corresponding corrections.

### 4.5.1 Tracking Efficiency

The tracking efficiency was estimated as:

$$\epsilon_{track} = \epsilon_{cham} \cdot \epsilon_{TOFU} \cdot \epsilon_{rec} \cdot \epsilon_{pid} \quad (4.36)$$

where

- $\epsilon_{cham}$  : detection efficiency of the tracking chambers;
- $\epsilon_{TOFU}$  : TOFU pulse height cut efficiency;
- $\epsilon_{rec}$  : Quanah reconstructing efficiency;
- $\epsilon_{pid}$  : particle identification efficiency.

The detection efficiency of the tracking chambers,  $\epsilon_{cham}$ , was extensively discussed in [73, 74]. The estimated  $\epsilon_{cham}$  is better than 99% for single track in the effective fiducial volume of the detectors. The effect of dead regions in the detectors are included in the acceptance correction. However, in the environment of multiple tracks, the large occupancy introduces a momentum dependent particle detection inefficiency due to the inability of detectors to reconstruct all the particle tracks that overlap within their finite spatial resolution. A correction for this tracking inefficiency, called *occupancy correction*, will be discussed in the following subsection.

The TOFU detector was constructed so as to maximize the efficiency for detecting particles. Slats were arranged to have a small overlap to eliminate any possible gap in the scintillator coverage while keeping to a minimum the fraction of particles hitting more than one slat. So the detecting efficiency of TOFU is near 100%. The inefficiency of TOFU comes from the imposed pulse-height cut, which has been discussed in section 4.3.3. The efficiency of pulse-height cut was carefully studied in [28, 82] and found to be about  $0.95 \pm 0.01$  for the cut range from 0.75 to 1.5 MIPS used in the analysis.

The track reconstructing efficiency in QUANAH strongly depends on the occupancy of track in the E877 spectrometer. For a larger occupancy, the track finding algorithm has more fail possibility. To keep up high efficiency of track reconstruction, the collimator of the E877 spectrometer had an opening to give an average of 6 particles into the acceptance per event. The QUANAH's reconstructing efficiency for single track was estimated better than 95% [66, 81].

The efficiency of the PID cut  $\epsilon_{pid}^{cut}$  is evaluated using a Gaussian approximation as

$$\epsilon_{pid}^{cut} = \int_{m_{min}^2}^{m_{max}^2} \frac{1}{\sqrt{2\pi}\sigma_m^2} \exp\left\{-\frac{(m^2 - m_0^2)^2}{2\sigma_m^2}\right\} dm^2 \quad (4.37)$$

where  $m_0$  is the mean mass of the particle,  $\sigma_m^2$  is the momentum-dependent resolution of squared mass  $m^2$ ,  $m_{min}^2$  and  $m_{max}^2$  are the momentum-dependent cut values on the measured  $m^2$ .

### 4.5.2 Occupancy Correction

When the hits of two passing particles on the tracking detectors are closer than the granularity of the detector, the position of each individual hit will not be resolved. Thus tracking inefficiency are introduced. This inefficiency is directly related to the distribution of particles in the detectors. The corresponding correction is thus called the *occupancy correction*. Several approaches to the occupancy correction have been developed in the data analysis history of E877 [28, 74, 83, 21]. They are designated for the specific physics aim of each particular analysis. In the present data analysis, the procedure for occupancy correction is an update from that developed by Roger Lacusse [28]. Some improvements are made such as introducing a centrality dependence and using the raw slat hit distribution in TOFU instead of the calculated position distribution which needs aids of DC2 and DC3.

The occupancy distributions in DC2, DC3 and TOFU are shown in Fig. 4.15. As expected the distributions across the face of DC2, DC3 and TOFU slats are not

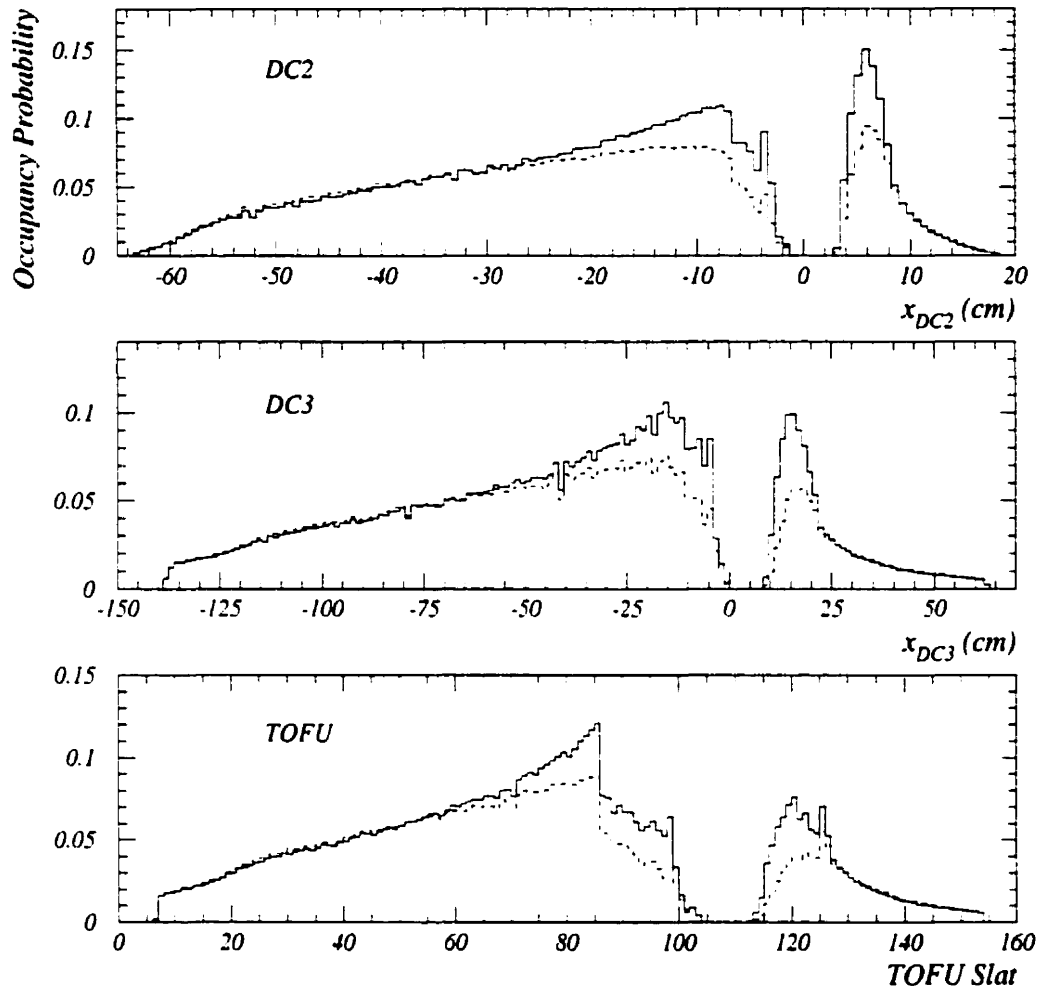


Figure 4.15: Measured Occupancy Distributions in DC2, DC3 and TOFU. The solid line denotes the 4-10% centrality, the dash line represents the 0-4% centrality.

uniform but are highly position and thereby momentum dependent. Particles with higher momentum are less deflected by the magnetic field and trend to concentrate close to the beam region. So large occupancy is around the beam hole region. It is also centrality dependent. Thus the probability of missing tracks is not only momentum

dependent but also depends on centrality.

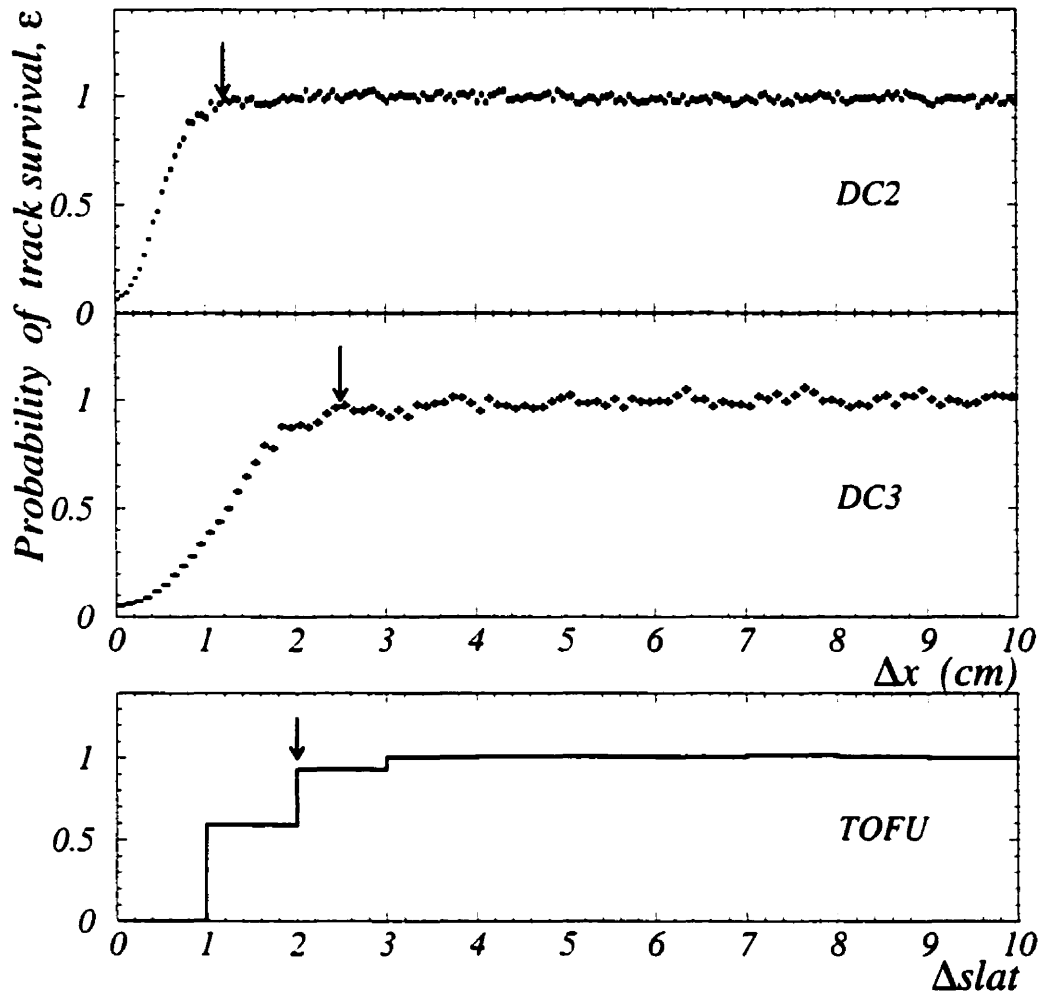


Figure 4.16: Probability of track survival as a function of track separation in DC2, DC3 and TOFU. The arrows indicate the minimum separation cuts in the pair analysis.

Since a detector has a finite granularity, it results in a limited ability at resolving close hits. This is illustrated in Fig. 4.16, where the response of DC2, DC3 and TOFU detectors to close hits is plotted as a function of hit separation. The efficiency

of resolving close tracks diminishes when the separation is less than a certain distance, 1.2 cm in DC2, 2.5 cm in DC3 and 2 slats in TOFU. From the distribution of surviving probability, we can estimate the number of missing tracks  $N_i^{\text{tracks}}$  around a given track

$$N_i^{\text{tracks}} = \int_{-l}^l T_i \cdot (1 - \varepsilon_i) dx_i, \quad (4.38)$$

where  $T_i$  denotes the track distribution,  $\varepsilon_i$  is the survival probability of a track,  $l$  is the minimum cut distance on track separation. Thus a weight factor  $W_i$  for each track is given by

$$W_i = 1 + \int_{-l}^l T_i \cdot (1 - \varepsilon_i) dx_i. \quad (4.39)$$

$W_i$  accounts for the correction of the missing tracks.

A track is missed in a detector is also possibly missing in the other detectors. In order to avoid the overcorrection, the correlation of tracking inefficiency in these detectors has been studied. Considering a two-detector system and a track at position  $x_1$  in detector 1 and  $x_2$  in detector 2, the number of tracks missed in detector 2 that were already missed in detector 1 is given by

$$S_{1 \times 2} = \int_{-l}^l C_{12} \cdot (1 - \varepsilon_2) dx_2 \quad (4.40)$$

where  $C_{12}$  is the distribution of positions  $x_2$  in detector 2 for tracks at  $x_1$  in detector 1, or  $x_1$  vs  $x_2$ . The major correlations are illustrated in Fig. 4.17. As expected there is a very close correlation between DC3 and TOFU since they are close to each other.

The overall occupancy correction for the spectrometer is given by

$$\begin{aligned} W &= [1 + N_{\text{DC2}}^{\text{tracks}}] \\ &\cdot [1 + N_{\text{DC3}}^{\text{tracks}} - S_{\text{DC2} \times \text{DC3}}] \\ &\cdot [1 + N_{\text{TOFU}}^{\text{tracks}} - S_{\text{DC2} \times \text{TOFU}} - S_{\text{DC3} \times \text{TOFU}} + S_{\text{DC2} \times \text{DC3} \times \text{TOFU}}] \quad (4.41) \end{aligned}$$

The calculated occupancy correction factors for  $\pi^-$  are shown in Fig. 4.18 as a function of transverse momentum and rapidity in two centrality bins. As expected

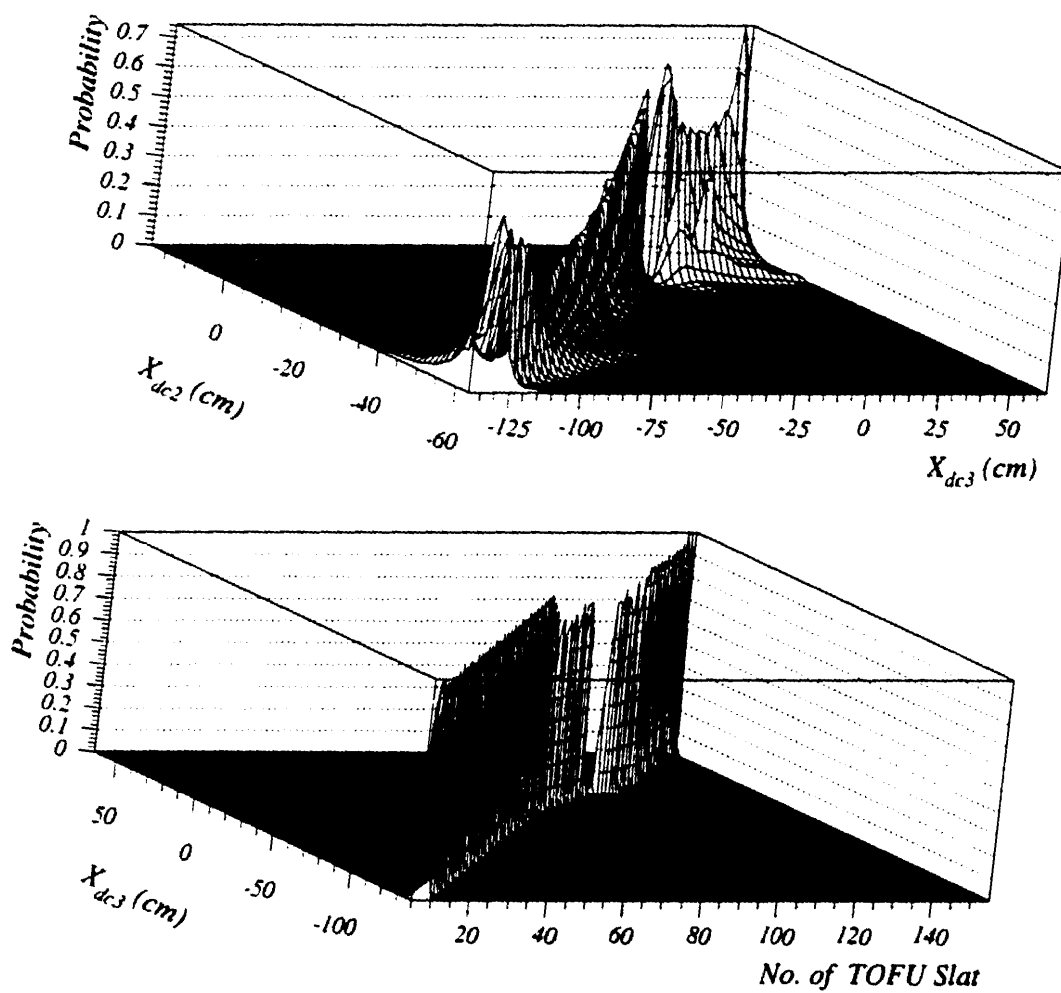


Figure 4.17: Correlation of the track hits on DC2, DC3 and TOFU. (a) correlation between DC2 and DC3; (b) correlation between DC3 and TOFU.

the effect of the correction is more important at low  $p_t$  and high rapidity, where tracks tend to concentrate around the beam trajectory in the higher occupancy region of the spectrometer. The effect of centrality on the correction for  $\pi^-$  is very small except

for the high rapidity.

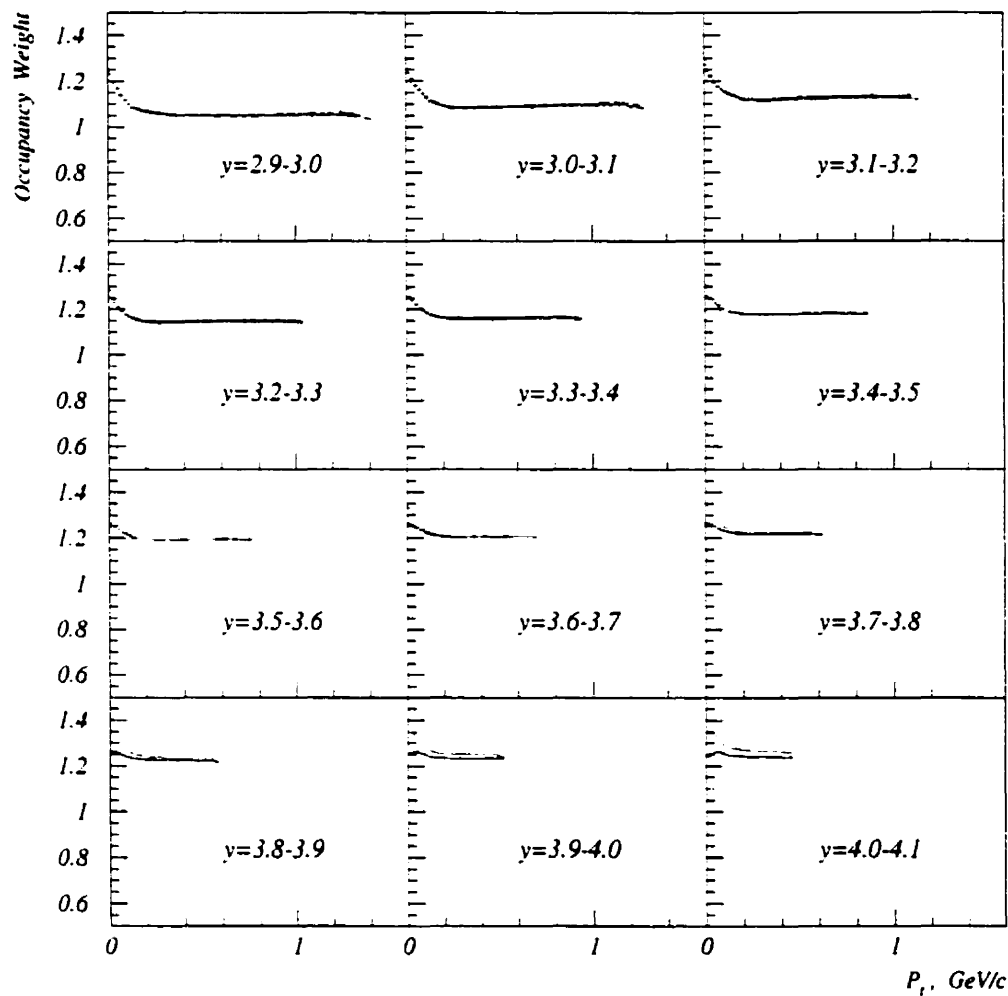


Figure 4.18: Magnitude of the occupancy correction for  $\pi^-$  as a function of transverse momentum and rapidity. The solid line denotes the 0-4% centrality. The dashed line represents the 4-10% centrality.

The occupancy correction factors for protons are shown in Fig. 4.19. As expected

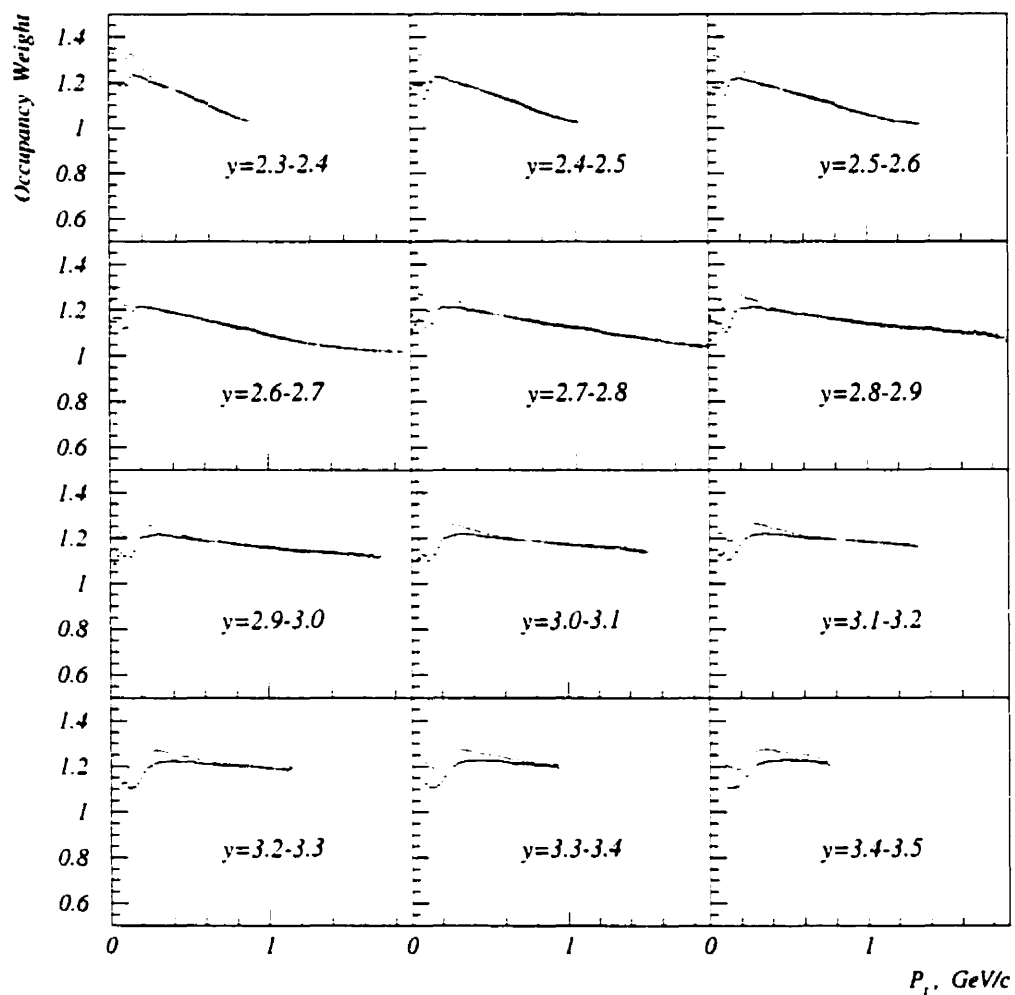


Figure 4.19: Magnitude of the occupancy correction for protons as a function of transverse momentum and rapidity. The solid line denotes the 0-4% centrality. The dashed line represents the 4-10% centrality.

the positive particles have a larger correction factor because they are more likely bent through the beam hole due to the negative field (-0.3353 T) of the spectrometer

magnet. Compared with pions, the  $p_t$  dependence of the correction for protons is more pronounced. The centrality dependences of the occupancy weight become much larger at low  $p_t$  because proton are heavier than pion and thus less deflected.

### 4.5.3 Acceptance Correction

The spectrometer samples only those particles emitted in a finite range of phase space. To deduce the invariant cross section from the measured data, a correction procedure for the finite sampling has to be applied. We call this procedure as *acceptance correction*. In this section we discuss the acceptance calculations for the particles originating from the target. The acceptance for lambda will be studied in the next chapter.

The geometric acceptance is computed by randomly generating particles over a  $p_t$  and  $y$  phase space larger than that covered by the spectrometer. The simulated particles are propagated through a software model of the spectrometer. This model includes following elements:

- *Geometry of spectrometer*: it includes the opening of the collimator and the effective fiducial volume of the tracking detectors. The fiducial cuts for the spectrometer are summarized in Table 4.5. The dead sections in each detector are also taken into account. The dead regions for beam traversing through are listed in Table 4.6.
- *Maximum momentum cut*: This cut is used in the particle identification cut (see Table 4.4).
- *Particle decay in flight*: the effect of particle decay in flight in the spectrometer is approximated by calculating the survival rate of the decay particle [77].

Table 4.5: Geometry of the E877 spectrometer and fiducial cuts used in the 1995 data analysis.

<i>Detector</i>	$z(\mu m)$	$x_{\min}(\mu m)$	$x_{\max}(\mu m)$	$y_{\min}(\mu m)$	$y_{\max}(\mu m)$
Coll. Front	813600	-100000	0	-9600	9600
Coll. Back	1626400	-196900	233300	-19000	19000
VTXA	2005000	-245800	-20190	—	—
VTXB	2255000	-281000	-20190	—	—
DC2	5382660	-634400	186250	—	—
MWPC1	6632600	-782000	278500	—	—
MWPC2	7840600	-940000	357400	—	—
MWPC3	9086900	-1082000	457000	—	—
MWPC4	10317200	-1255000	547500	—	—
DC3	11545875	-1398000	636710	—	—
TOFU	$\sim 12300000$	-1469800	685000	—	—

Table 4.6: The dead zones of tracking detectors due to beam hole

<i>Detector</i>	$x_{\min}(\mu m)$	$x_{\max}(\mu m)$
*VTXA	-20190	12677
*VTXB	-20190	14869
DC2	-16660	39430
MWPC1	-38266	46584
MWPC2	-41251	45406
MWPC3	-35835	70642
MWPC4	-32819	75871
DC3	-9582	96405

\* Only used in the acceptance calculations for lambda

- *Beam spread*: beam extension at the target is also taken into account by using the measured distributions.

For each particle that is accepted, a phase space histogram is incremented at the corresponding  $(p_t, y)$  bin. Finally, the distributions are normalized by the number of the generated particles. The resulting phase space acceptance diagrams for pions, kaons, protons and deuterons are shown in Fig. 4.20. Several features are worth noting. For each specie the left-most boundary corresponds to the edge of the collimator, and the right-most boundary is due to the maximum momentum cut. The negatively charged particles are favoured by the negative magnetic field in the 1995 run. The detector dead sections introduce dead bands in the acceptances of the positive particles at low transverse momentum. They affect the low  $p_t$  spectra in the detection of  $p$ ,  $\pi^+$ ,  $K^+$  and deuteron.

The acceptance corrections for proton in different rapidity slices are shown in Fig. 4.21. One can see that the dead sections for the beam passage on the tracking detectors have a large effect on the detection of protons at low  $p_t$ . At  $y < 2.8$  the dead sections create a hole in the acceptance at low  $p_t$  around 0.1 GeV/c. For  $y > 2.8$  the acceptance does not extend down to  $p_t = 0$  due to these dead sections. The structures that are found throughout the acceptance distributions originate from other individual detector dead regions. These acceptance calculations will be used in constructing the inclusive proton and pion spectra presented in chapter 7.

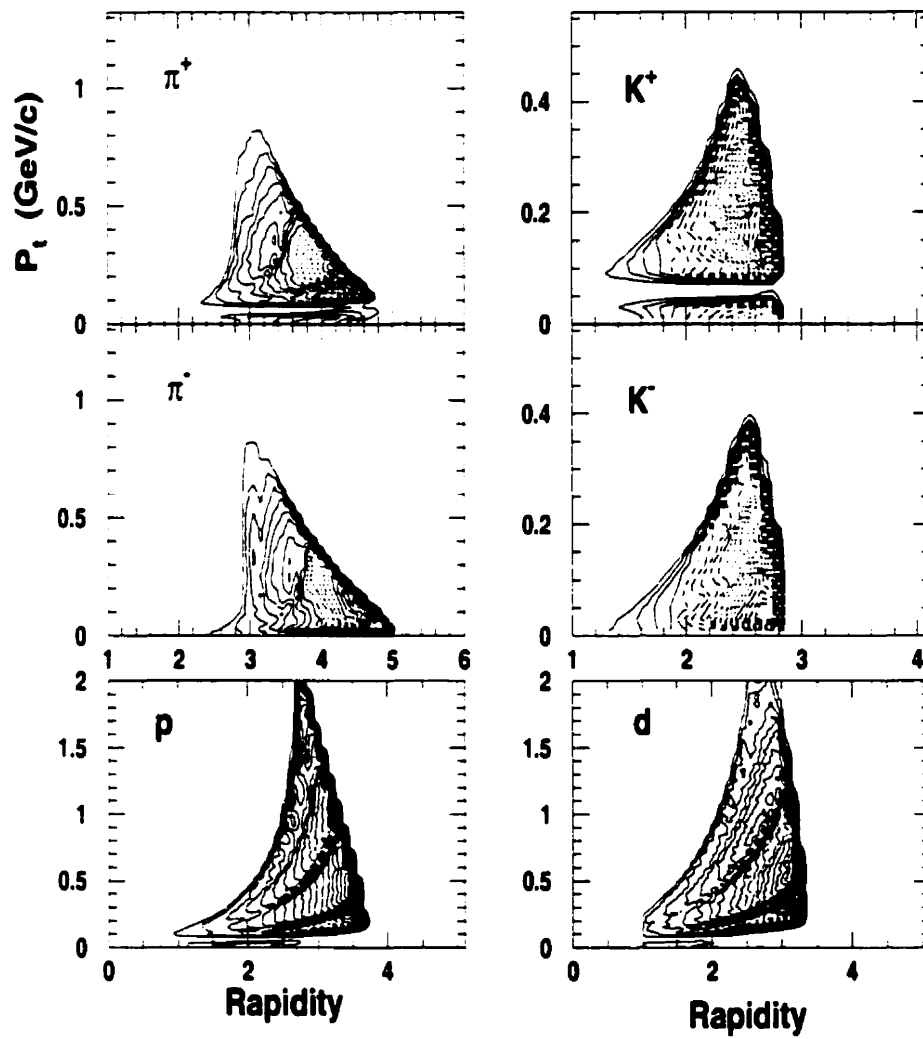


Figure 4.20: Acceptance of E877 spectrometer at -0.3353 T magnetic field setting. The acceptance is plotted as a function of transverse momentum versus rapidity.

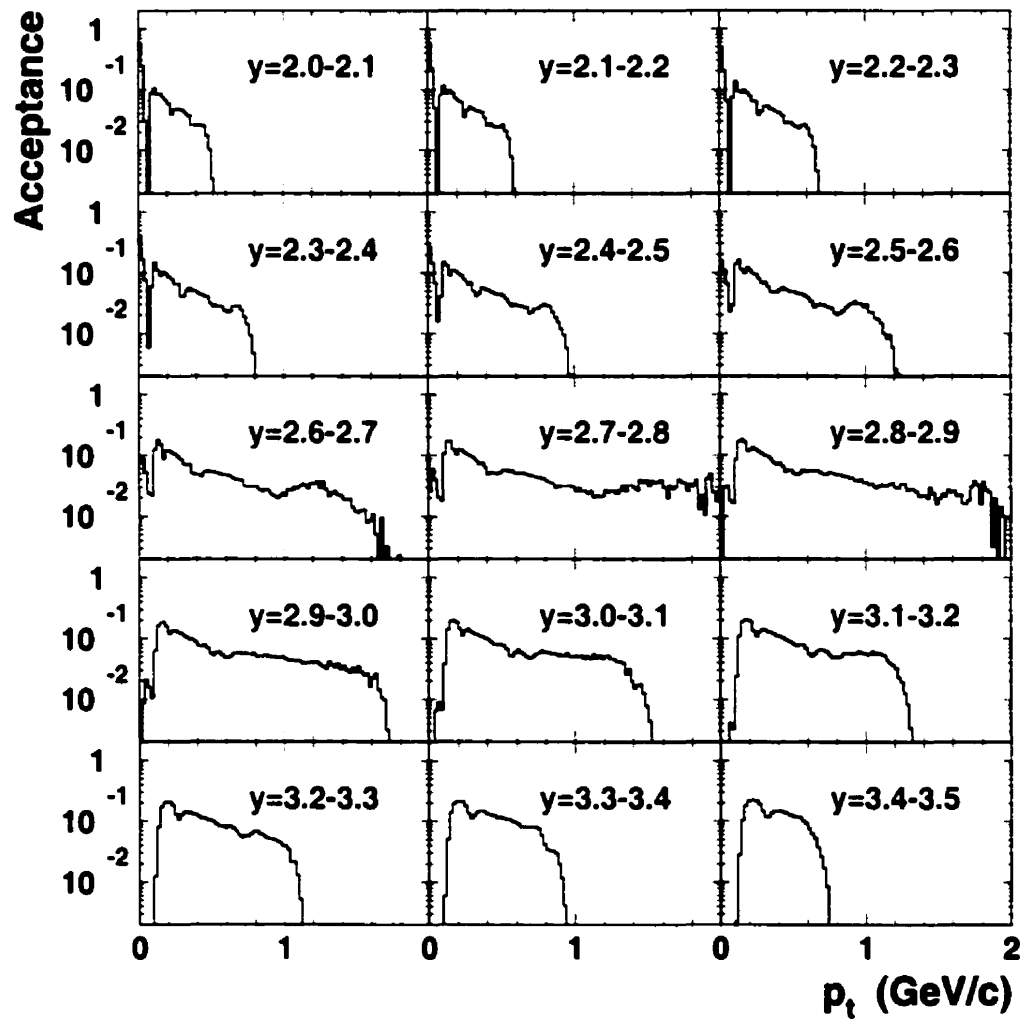


Figure 4.21: Acceptance corrections for proton in different rapidity slices. The calculation was based on the E877 spectrometer magnet operating at  $-0.3353$  Tesla.

## Chapter 5

# Monte Carlo Simulation

Lambda is a short-lived particle ( $\tau \sim 2.6 \times 10^{-10}$ s). Although our detectors couldn't directly detect it, we can measure it via its charged decay channel:  $\Lambda \rightarrow p + \pi^-$  which has a branch ratio of 64%. Since lambdas are reconstructed from the measured  $p$  and  $\pi^-$  pairs, the reconstruction is thus an inverse process of its decay. The careful investigations of the kinematics of lambda decay can greatly help us to better understand the lambda reconstruction. So a comprehensive Monte Carlo kinematic simulation has been developed for these studies.

The properties of the E877 spectrometer, such as the momentum resolution and the response of the VTX detectors, are included in the simulation. In order to avoid involving in too much the detailed properties of the detectors, we have used the parameterized formulas described in section 4.3.2 and section 4.4.1 in the previous chapter. The acceptance for  $\Lambda \rightarrow p + \pi^-$  into the E877 spectrometer will be first studied in the simulation taking into account the decay properties of  $\Lambda$ 's.

As discussed in section 4.3.2, the track finding code, QUANA, assigns a track momenta by assuming the track originates from the target. This assumption is wrong for the secondary tracks from decay particles such as  $\Lambda$ 's. We will look into the

resulting effect on the lambda reconstruction in the simulation. A corresponding correction, called *backtracking* correction, will be developed.

The high abundance of primary protons and pions in the Au+Au collisions results in large uncorrelated  $p$  and  $\pi^-$  pairs (background) in the lambda reconstruction. It is a great challenge to identify the  $\Lambda$ 's signal from such large background of uncorrelated pairs. Some pair cuts have to be made in the data analysis in order to identify lambda. So we will investigate the pair cut parameters so as to set up the optimized cut criteria.

The contents of this chapter are arranged as follows. We first introduce an event generator used for the simulation, then we look into the acceptance for  $\Lambda$ s into the E877 spectrometer and discuss the backtracking issue, and last we study the pair cut parameters by contrasting the cut parameter distributions of the true pairs from lambda decay to the mixed pairs from the uncorrelated  $p$  and  $\pi^-$  pairs.

## 5.1 Event Generator

Since the RQMD model predicts the proton and pion spectra of Au+Au very well [28], we can use the predictions of this model as the event generator of the simulation. In principal, we could use RQMD generated events directly as the event generator of the simulation. Unfortunately, calculating Au+Au events with RQMD takes large amount of CPU time. Since a great amount of events are needed to study the cuts in the lambda reconstruction, the distribution of particles in the simulation were obtained in the following way:

1. we take all the statistics of  $\Lambda$ 's from the about 100K RQMD events to obtain  $\Lambda$ 's  $dN/dy$  and  $m_t$  spectra in rapidity ( $\Delta y = 0.1$ ) slices;
2. we fit the  $m_t$  spectra by Boltzmann distribution (solid lines in Fig. 5.1);

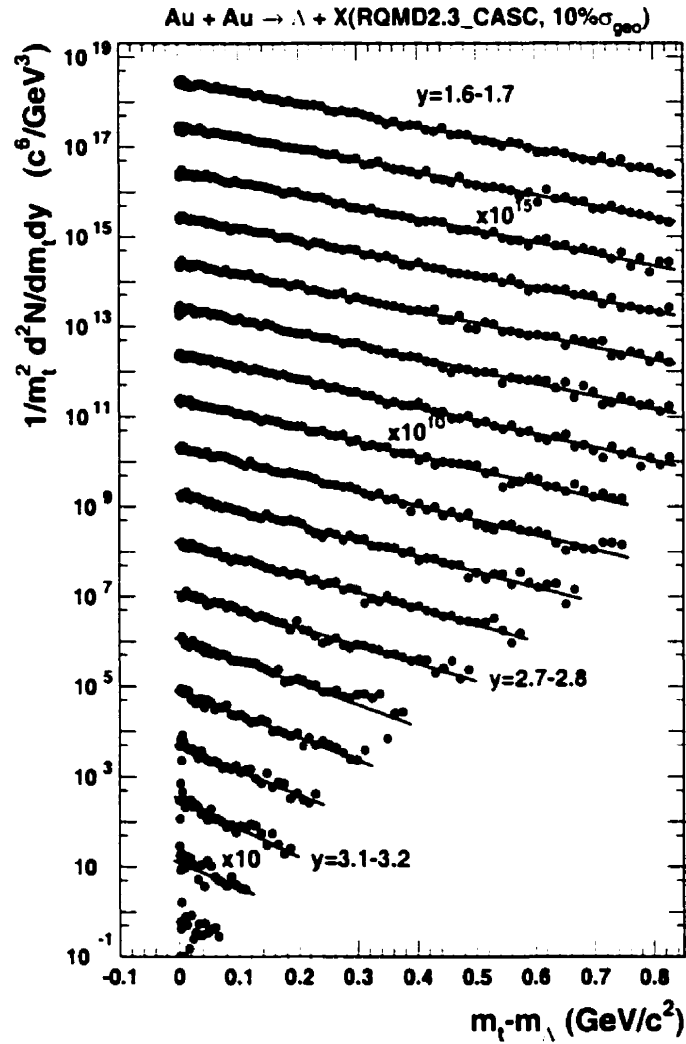


Figure 5.1:  $\Lambda$  spectra from the RQMD v2.3 model run in cascade mode. Beginning with rapidity slice  $y = 3.2 - 3.3$ , spectra have been multiplied by successively increasing powers of ten. Solid lines represent the fits of Boltzmann distribution.

3. then we build a event generator based on the obtained  $dN/dy$  distribution and the parameters of the fitted  $m_t$  spectra.

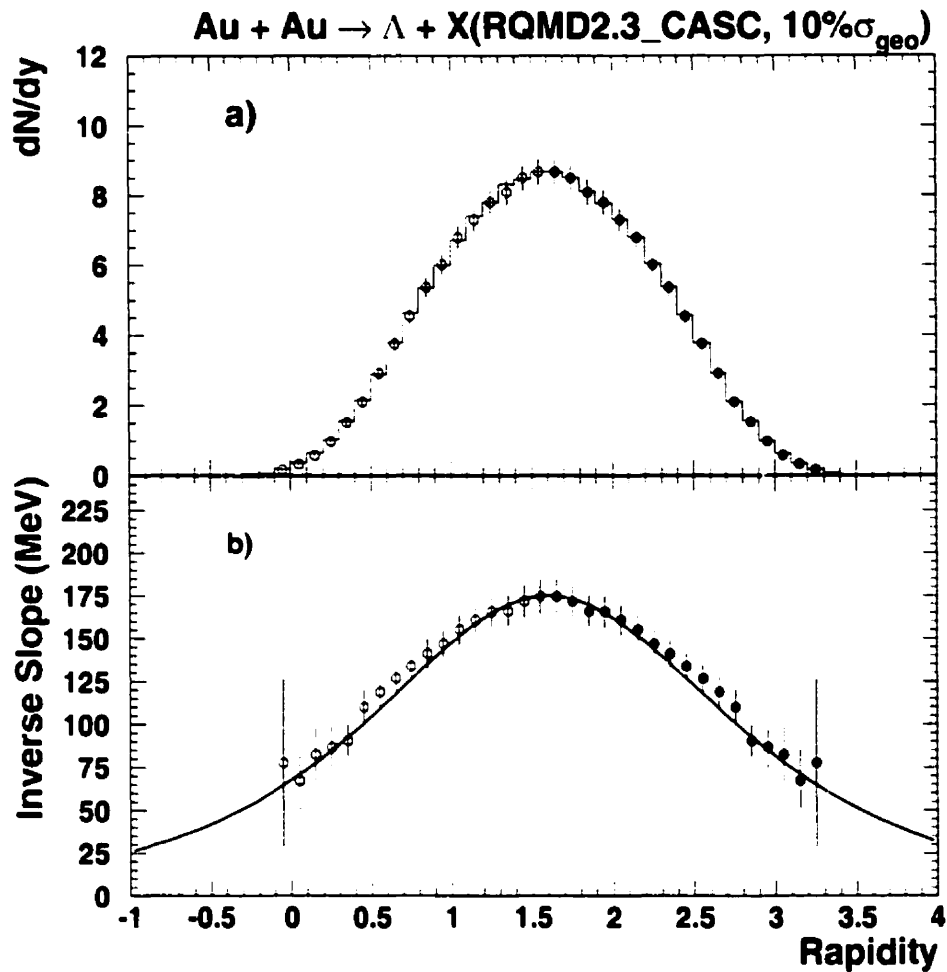


Figure 5.2: a). The  $dN/dy$  distribution of  $\Lambda$ 's, the histogram is the prediction of the RQMD v2.3 model run in cascade mode and the solid points are integrated by extrapolating the  $m_t$  spectra. They are perfectly matching. b). The inverse slope parameter of  $\Lambda$ 's obtained from the Boltzmann fitting in 5.1. The solid line corresponds to Eq. 5.1

The transverse mass ( $m_t$ ) spectra of  $\Lambda$ 's obtained from the RQMD v2.3 model run in cascade mode are shown in Fig. 5.1. The centrality was chosen at 10%. The dots represents the data, and solid lines correspond to a Boltzmann fit. The  $dN/dy$  distribution and the inverse slope parameters are shown in Fig. 5.2. The inverse slope

parameters,  $T_B$ , as a function rapidity can be well described by

$$T_B(y) = 175/\cosh(y - y_{cm}) \quad (5.1)$$

where  $y_{cm}=1.6$  as shown by the solid line in Fig. 5.2.

## 5.2 Acceptance for $\Lambda \rightarrow p + \pi^-$

To determine the correction of the lambda production, we have to know the phase space coverage of the spectrometer for  $\Lambda$ 's. As stated before, the decay properties of lambda have to be taken into account in the simulations. Lambda decays with its proper lifetime in its rest frame. In the calculations we assumed that the decay is isotropical in the center-of-mass of the lambda. The decay momenta then were transferred to the laboratory system by Lorentz invariant transformation. We count a lambda accepted in the E877 spectrometer only when its decay pair ( $p, \pi^-$ ) both are within the fiducial volume of the spectrometer as defined in section 4.5.3. Fig. 5.3 shows the scattering plots for proton emission in the rest frame of lambda. As expected, the E877 forward spectrometer kinematically favors the pairs in which  $p$  in the backward hemisphere and  $\pi^-$  is emitted forward. Fig. 5.4 shows the range of acceptance for lambda decay into the E877 spectrometer. The decay momentum of lambda is only about 101 MeV/c. Because of its mass the secondary protons obtain a relatively weak kick. That's why the acceptance of protons from  $\Lambda$  decay is much like that of directly produced protons originating from the target (see Fig. 5.4(a)). But for the  $\pi^-$ , the situation is quite different since the decay momentum is comparable to the mass of pion. Only low  $p_t$  pion from  $\Lambda$  decay can be accepted in the spectrometer (see Fig. 5.4(b)). So the secondary pions from lambda decay have a considerable contribution to the low  $p_t$  part of the inclusive  $\pi^-$  spectra [36].

As shown in Fig. 5.5, the spectrometer is sensitive only to the  $\Lambda$ s produced at

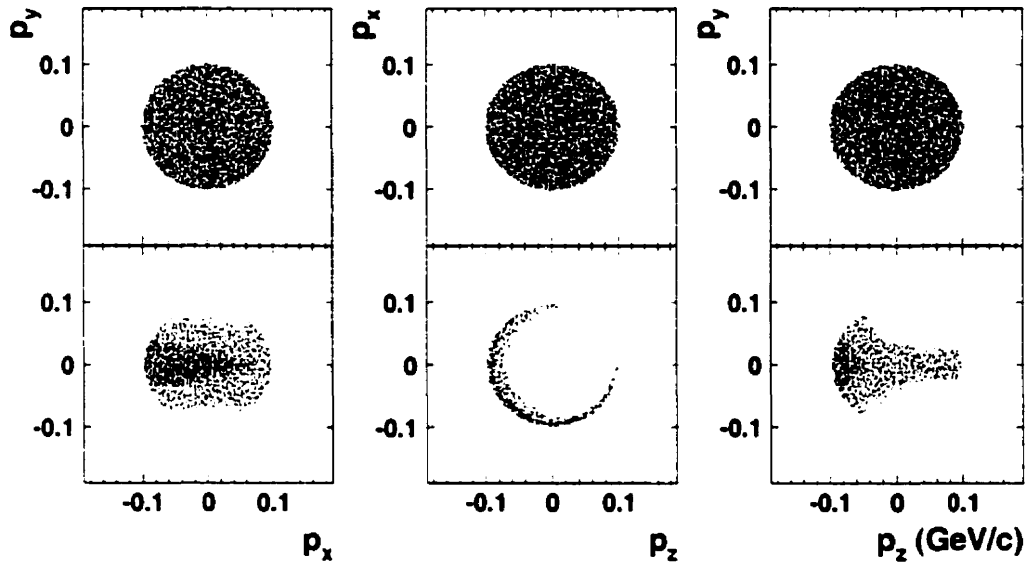


Figure 5.3: Scattering plots for proton emission in the rest frame of  $\Lambda$ 's. The top panels show the generated protons emitting isotropically in the center-of-mass system of  $\Lambda$ 's. The bottom panels show the secondary protons from lambda decay when the decay pair both are accepted by the E877 spectrometer.

forward rapidities. The solid line represents for the generated  $\Lambda$ s and the dash line denotes the accepted  $\Lambda$ s in the spectrometer. The overall geometrically detecting efficiency for  $\Lambda \rightarrow p + \pi^-$  into the spectrometer is of the order of  $10^{-3}$ . Note that in order to reduce the combinatorial backgrounds, some additional cuts will have to be made, which will further reduce the number of the  $\Lambda$ s identified by roughly another factor of ten. In general, the overall reconstructing efficiency for lambda is of the order of  $10^{-4}$ . The detailed descriptions of the acceptance correction with pair cuts for lambda spectra will be given in the next chapter.

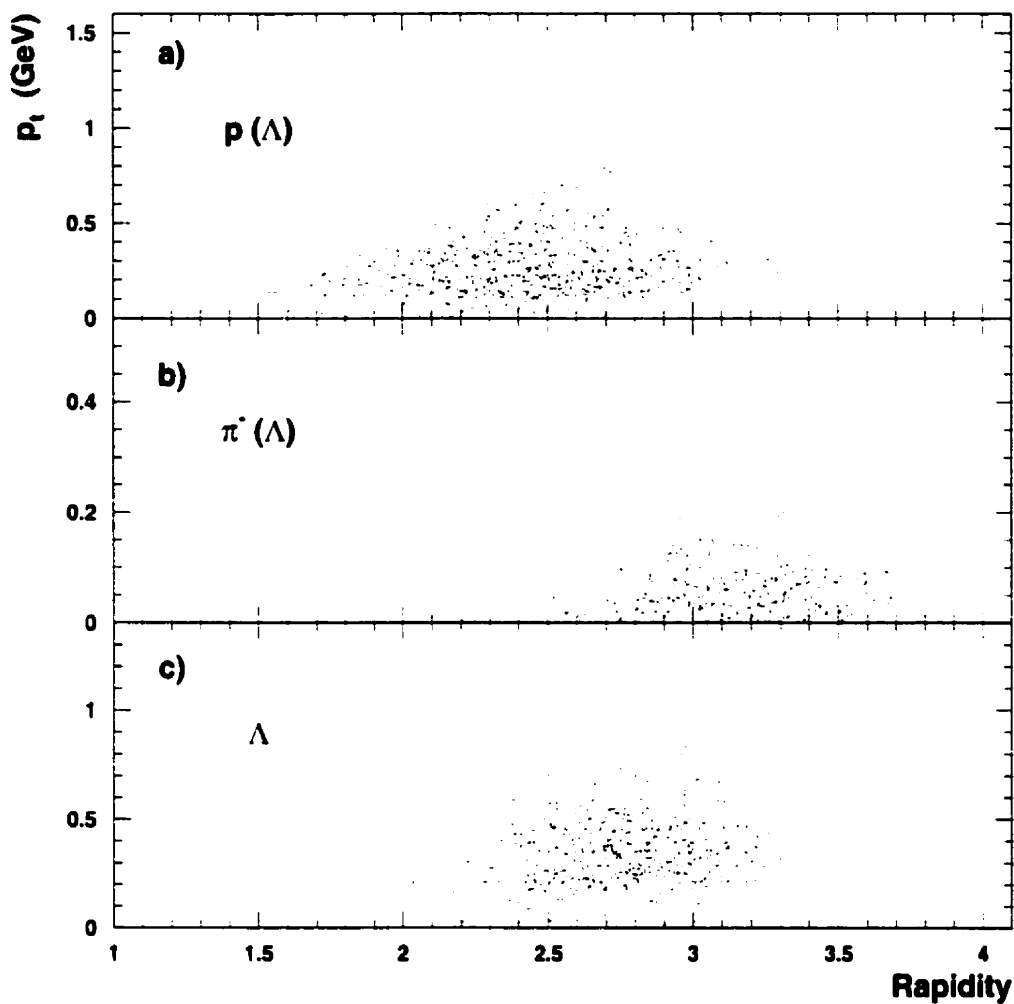


Figure 5.4: The range of acceptance for  $\Lambda \rightarrow p + \pi^-$  into the E877 spectrometer. a). for secondary proton from  $\Lambda$  decay; b). for secondary  $\pi^-$  from  $\Lambda$  decay; c). for  $\Lambda$ .

### 5.3 Backtracking

As mentioned before, the *backtracking* arose from the track's target-origin assumption in QUANA. This assumption is not valid for the secondary tracks from  $\Lambda$ 's decay

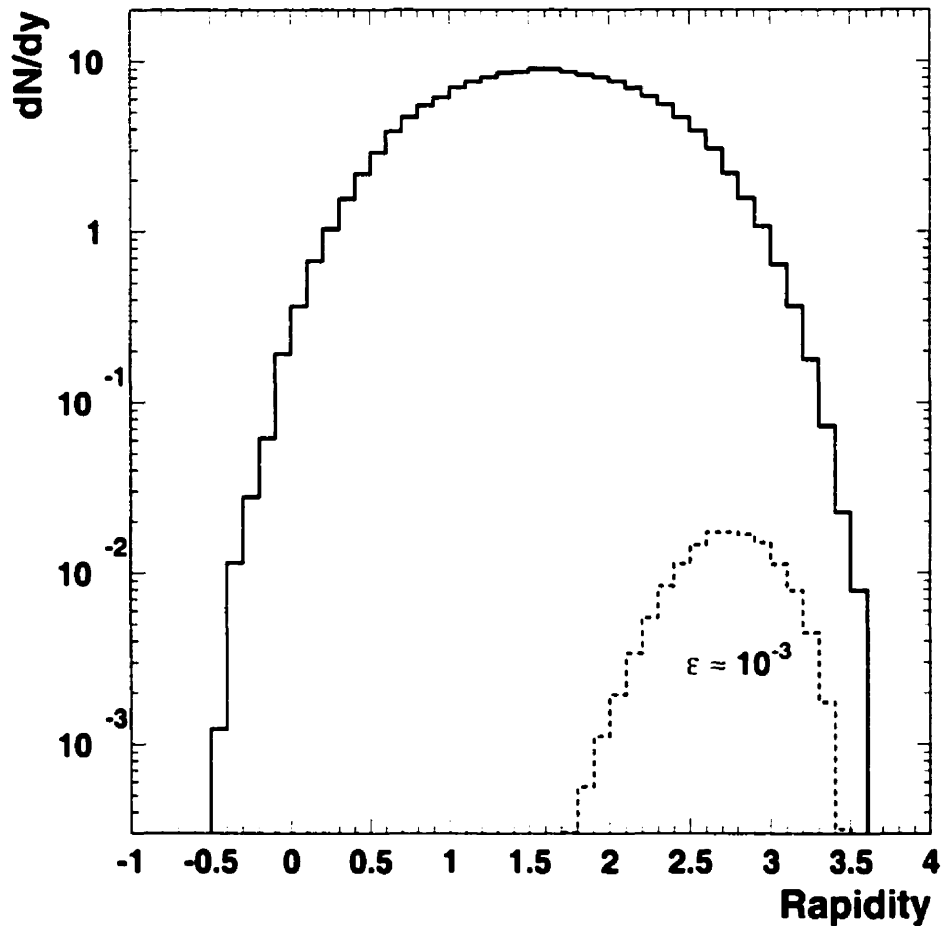


Figure 5.5: Estimation of the geometrically detecting efficiency for  $\Lambda \rightarrow p\pi^-$  into the spectrometer. The solid line is the predictions of the RQMD v2.3 model in cascade mode and the dash line denotes the accepted  $\Lambda$ 's by the spectrometer.

and results in wrong momenta assigned to those tracks. Since the invariant mass of  $(p, \pi^-)$  pair and its momentum are directly calculated from track momenta, it is very sensitive to the effect as shown in Fig. 5.6.

Fig. 5.6(a) shows the calculated invariant mass distribution of  $\Lambda$ 's. This spectrum

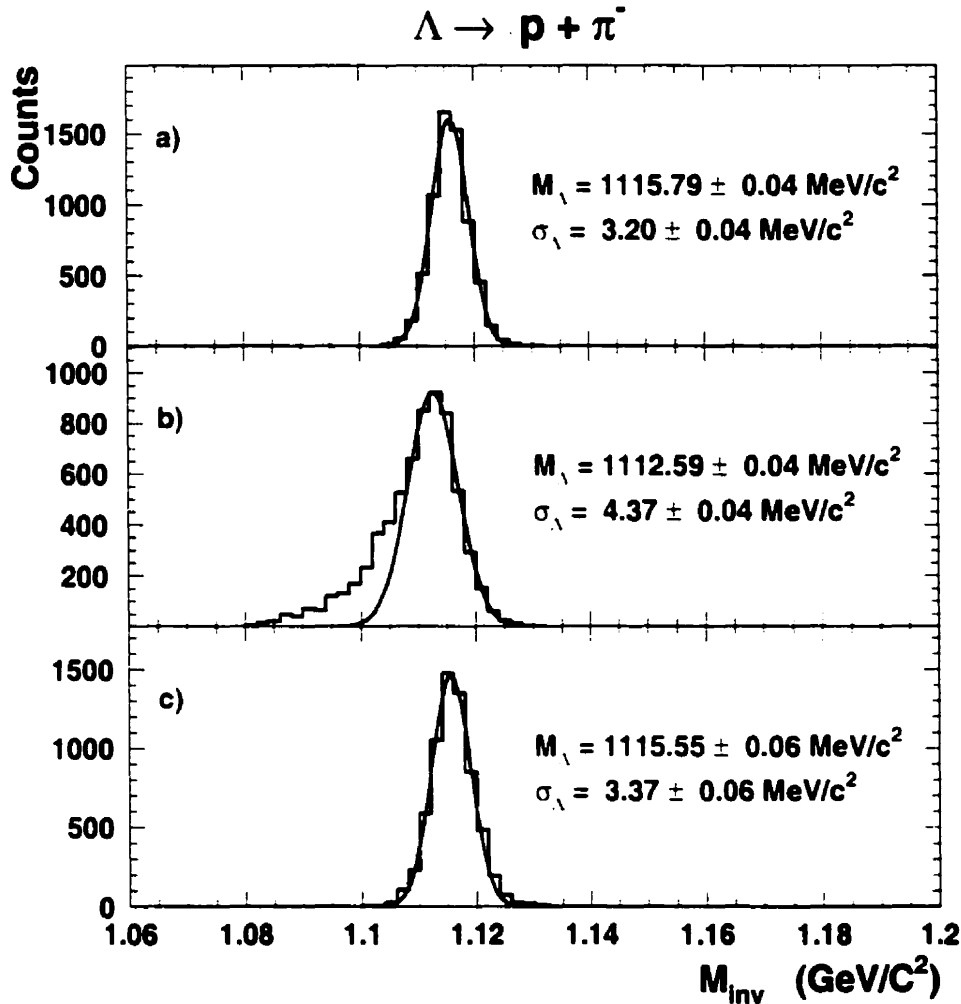


Figure 5.6: a). Invariant mass spectrum of  $\Lambda$ 's taking into account the momentum resolution of the spectrometer: b). Distorted invariant mass spectrum of  $\Lambda$ 's due to the assumption that track originates from the target. c). Corrected invariant mass distribution of  $\Lambda$ 's by backtracking.

was obtained using generated events and included smearing due to the momentum resolution of the E877 spectrometer. The expected mass resolution is about  $3.2 \text{ MeV}/c^2$ . Fig. 5.6(b) shows the calculated invariant mass spectrum of the  $p$  and  $\pi^-$  pair from lambda decay when it is assumed that the particles are produced at the

target, as done in QUANA. One can see that the lambda peak is not only wider but also severely distorted with a tail at low mass values. Note that the distortion will be more important for lambda that decay further away from the target. Obviously, this distortion has to be corrected. A correction procedure has been developed, called as *backtracking*. This correction uses the upstream tracking information from the VTX detectors to determine the position of the decay vertices. This position is inserted as the new origin of the tracks in the momentum assigning procedure. Thus it produces corrected vector momentum for the secondary tracks. By applying the backtracking correction, the distortion of the invariant mass distribution is well corrected as shown in Fig. 5.6(c). This backtracking correction is added into the data analysis to determine the properties (mass, rapidity and transverse momentum) of decay particles.

## 5.4 Investigation of Pair Cuts

Pair cuts play an essential role in lambda identification. The secondary ( $p, \pi^-$ ) tracks from the lambda decay and the directly produced ( $p, \pi^-$ ) tracks are indistinguishable in the experimental data (lean ntuples). Thus, identifying the  $\Lambda$ 's signal becomes very difficult due to the large combinatorial background. Therefore some pair cuts have to be introduced in data analysis to help the identification. But determining these cut parameters is very difficult. Fortunately, using the Monte Carlo simulation we can study lambda signal originating from true pairs and the combinatorial background produced by mixed (uncorrelated) pairs. Further by looking into the features of the cut parameters, we can find the optimized cut criteria.

The  $\Lambda$  decay and reconstruction in the spectrometer are illustrated in Fig. 5.7. To reduce the large combinatorial backgrounds, five types of ( $p, \pi^-$ ) pair cuts are included in our investigations. They are:

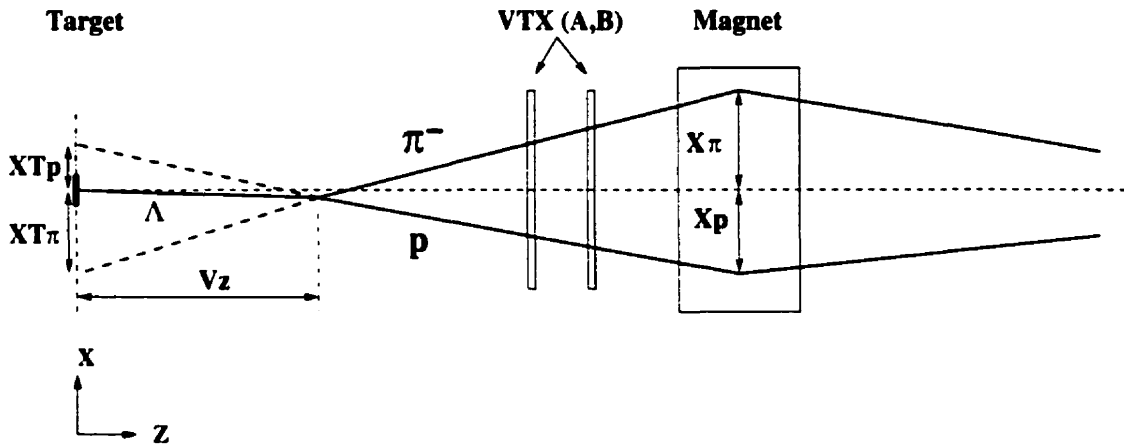


Figure 5.7: Schematic diagram illustrating  $\Lambda$  decay and reconstruction.

- Minimum pair-track separations:** The finite resolution of the tracking detectors results in limited ability at resolving close pair tracks. An *occupancy correction* was developed to resolve this inefficiency of the tracking detectors for single track analysis in section 4.5.2. In the analysis of pair tracks, we just remove those pair tracks whose separations in the two drift chambers and TOFU are closer than the minimum separations (see Fig. 4.16). This type of cut can improve the pair invariant mass resolution, but it also rejects some  $\Lambda$  samples.
- Distance  $V_z$  of decay vertex from the target:**  $V_z$  is one of the most essential pair cut parameters. Its distribution is supposed to be different between the  $\Lambda$ 's and the backgrounds as shown in Fig. 5.8. The upper panel shows the calculated  $V_z$  distribution from lambda decay (true pairs). The solid curve represents the true  $V_z$  distribution of the  $\Lambda$  entering the spectrometer. It has close to an exponential shape related to the  $\Lambda$  lifetime. The dash curve denotes the reconstructed  $V_z$  distribution from the upstream tracking information from the VTX detectors and takes into account the detector resolution. Due to the limitation of the position resolution of the two VTX detectors the measurement of  $V_z$  is less precise for particles that decay near the target. On the other hand,

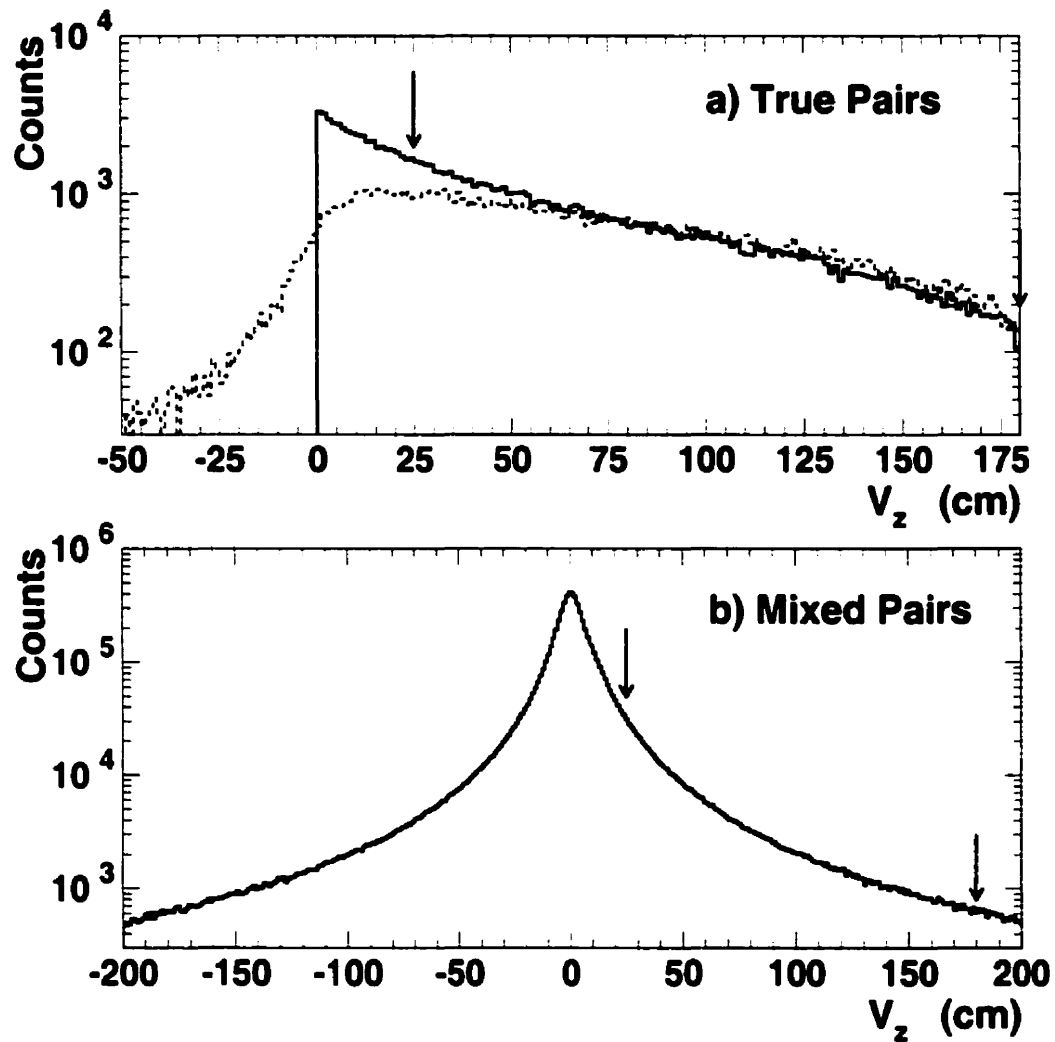


Figure 5.8: Investigation of  $V_z$  distributions of true pairs and mixed pairs. a)  $V_z$  distribution from true pairs (lambda decay); b)  $V_z$  distribution from mixed pairs (backgrounds). The arrows indicate the selected cut parameters.

the  $V_z$  distribution from the mixed pairs (see Fig. 5.8(b)), as expected, is peaked at the target ( $V_z = 0$ ) with a long tail. The minimum  $V_z$  cut is set at 25 cm downstream of the target. We fixed a maximum  $V_z$  cut at 180 cm from the

target, which is basically limited by the VTX detector position. This type of cuts has an effect not only to reduce the large backgrounds but also to cut a fraction of true  $\Lambda$  samples. This fraction is estimated at the order of 28%. We have to note that the above two types of pair cuts are included in the studies of the following pair cuts.

- **( $p$ ,  $\pi^-$ ) pair tracks pointing away from the target:** the upstream tracks of  $p$  and  $\pi^-$  as determined by the VTX detectors are projected back to the target to obtain  $XT_p$  and  $XT_\pi$ . Fig. 5.9 shows the calculated  $XT_p$  and  $XT_\pi$  distributions for true pairs and mixed pairs. The first two cuts have been already included in this study, which cause a dip at  $x = 0$  on the true pair's distributions. Let's focus on the shapes of the distributions. As expected, the distributions for true pairs from lambda decay are much broader than those for the mixed pairs, especially for the secondary  $\pi^-$  which received a larger kick in the decay. The  $XT_\pi$  distribution is roughly 5 times broader than that from the directly produced  $\pi^-$ . So we set a tight cut on  $XT_\pi$  ( $> 10$  mm) and a loose cut on  $XT_p$  ( $> 4$  mm). This means that only those pair tracks in which  $p$  track points more than 4 mm away from the reaction point and  $\pi^-$  track points more than 10 mm away from the reaction point are considered. This cut reduces a considerable the combinatorial backgrounds. However, it also rejects the  $\Lambda$ s that decay close to the target and the  $\Lambda$ s where the decay particles are emitted along the lambda momentum vector.
- **Track matching between upstream and downstream:** the upstream track segment is determined by VTX detectors and the downstream track segment is determined QUANA by the downstream tracking detectors. For any good tracks, the two segments of a track should match at the center of the spectrometer magnet. We can also use the matching point to improve the upstream

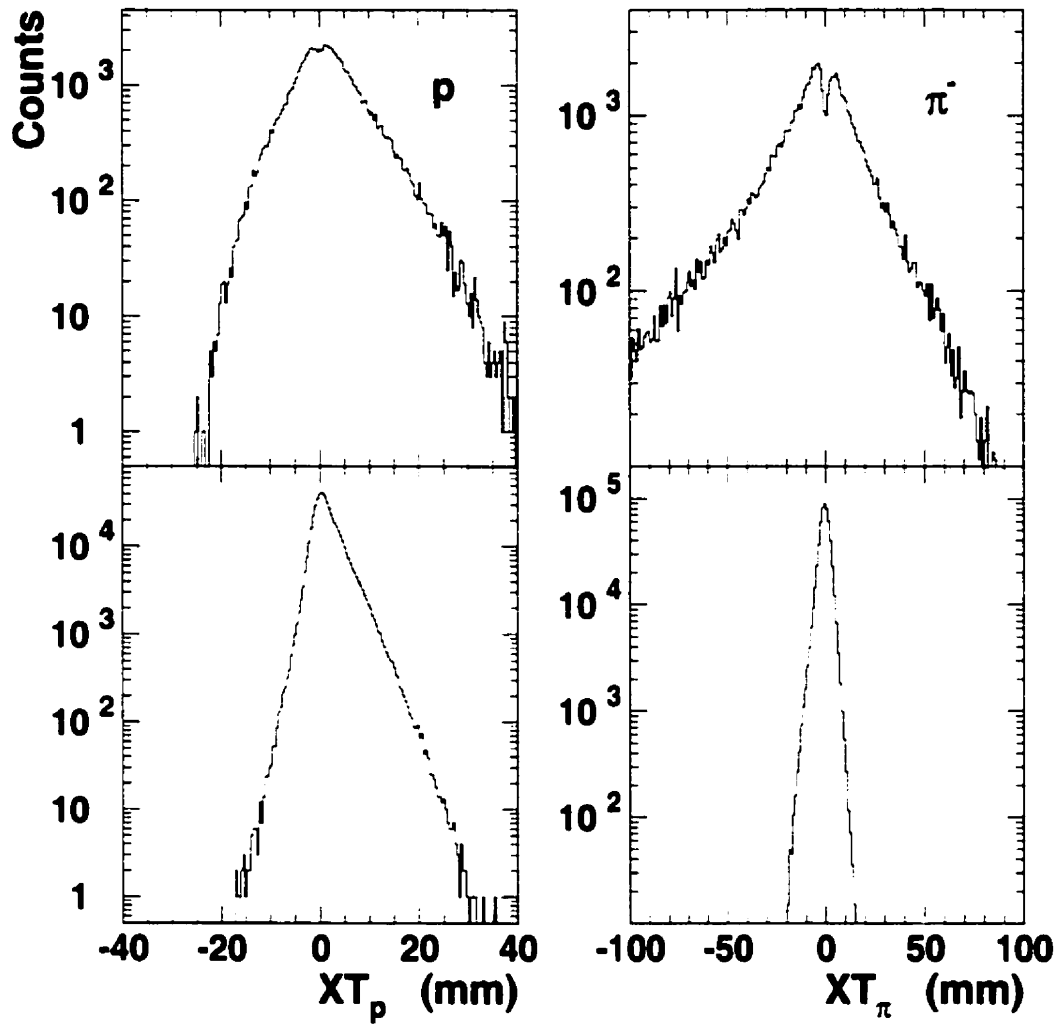


Figure 5.9: Investigation of the extrapolated track position at the target. The true pair's distributions are shown at upper parts while the mixed pair's distributions are shown at lower parts.

tracking and the determination of the decay vertex position. This will be discussed in the next chapter.

Fig. 5.10 show the calculated distributions of the matching parameters  $\Delta X_p$  and

$\Delta X_\pi$  for true pairs and mixed pairs. They all exhibit nice Gaussian shapes. As

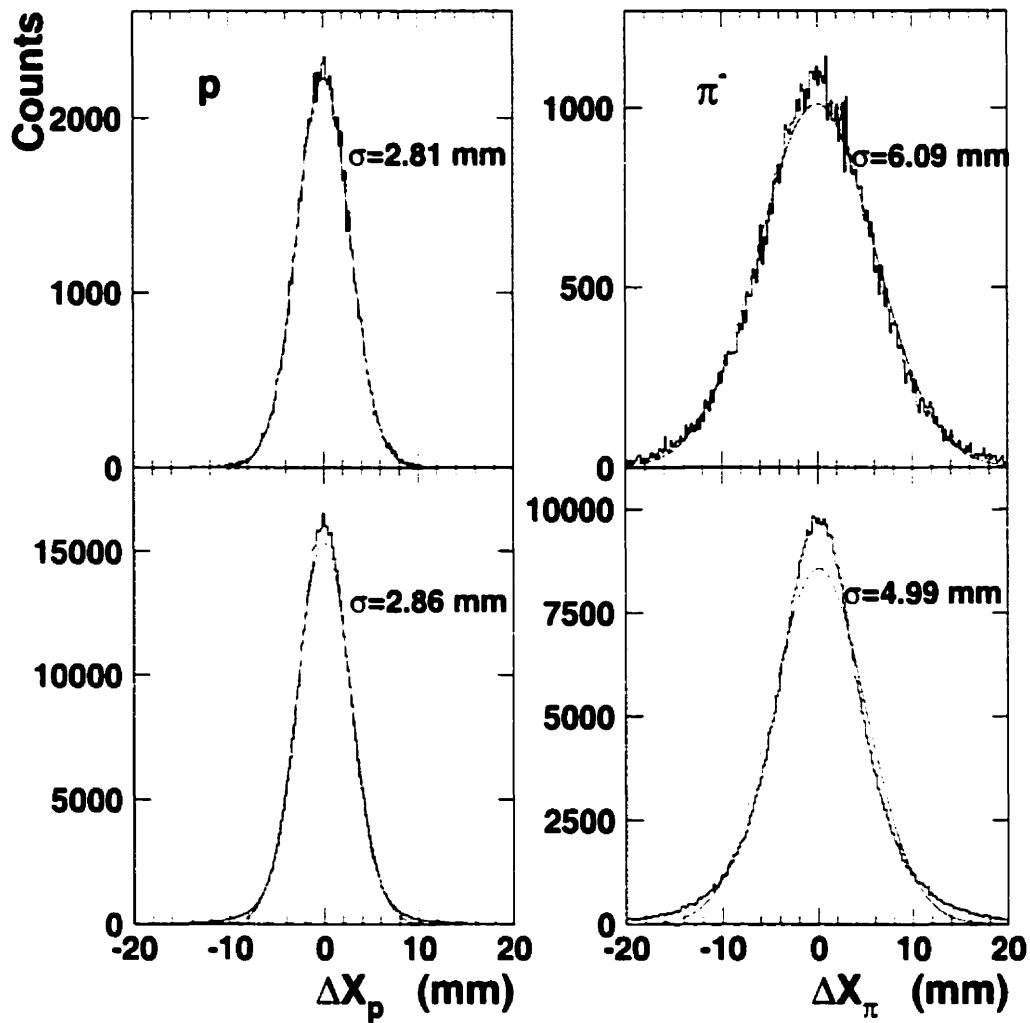


Figure 5.10: Investigation of the track matching parameters at the center of the magnet. The true pair's distributions are shown in upper parts while the mixed pair's distributions are shown in lower parts. The solid lines represent Gaussian fits.

expected. for both particles the shapes of both true pairs and mixed pairs are no much different. But for the  $\pi^-$ , the distribution of true is somewhat wider

than that of mixed pairs. Since in both cases the simulation contains only valid tracks, thus this cut has little effect on the contribution of combinatorial background but its main effect is in reducing the contribution from misidentified background tracks.

- **Reconstructed momentum vector pointing back to the target:** the reconstructed pair momentum vector is supposed to point back to the reaction point at the target, because the  $\Lambda$ s produced in the reactions should come from the target while the backgrounds may not. So the reconstructed momentum vector is projected back to the target to obtain  $\Delta X_v$  and  $\Delta Y_v$ . The calculated  $\Delta X_v$  distributions for true pairs and mixed pairs are shown in Fig. 5.11. As expected, the  $\Delta X_v$  distribution for true pairs from lambda decay shows a nice Gaussian distribution with  $\sigma \sim 1$  mm. On the other hand, the mixed pair distribution is distorted on the right edge with a long tail. So we set a cut on  $\Delta X_v$  within  $\pm 2\sigma$  to conserve the majority of  $\Lambda$  samples and reject the backgrounds on the long tail of  $\Delta X_v$  distribution from mixed pairs. This cut will also have an effect to reduce the background produced by misidentified tracks.

In addition to the investigations of the pair cuts, the above calculations are also used to evaluate the reconstruction efficiency for lambda spectra in the data analysis. This will be discussed in the following chapter.

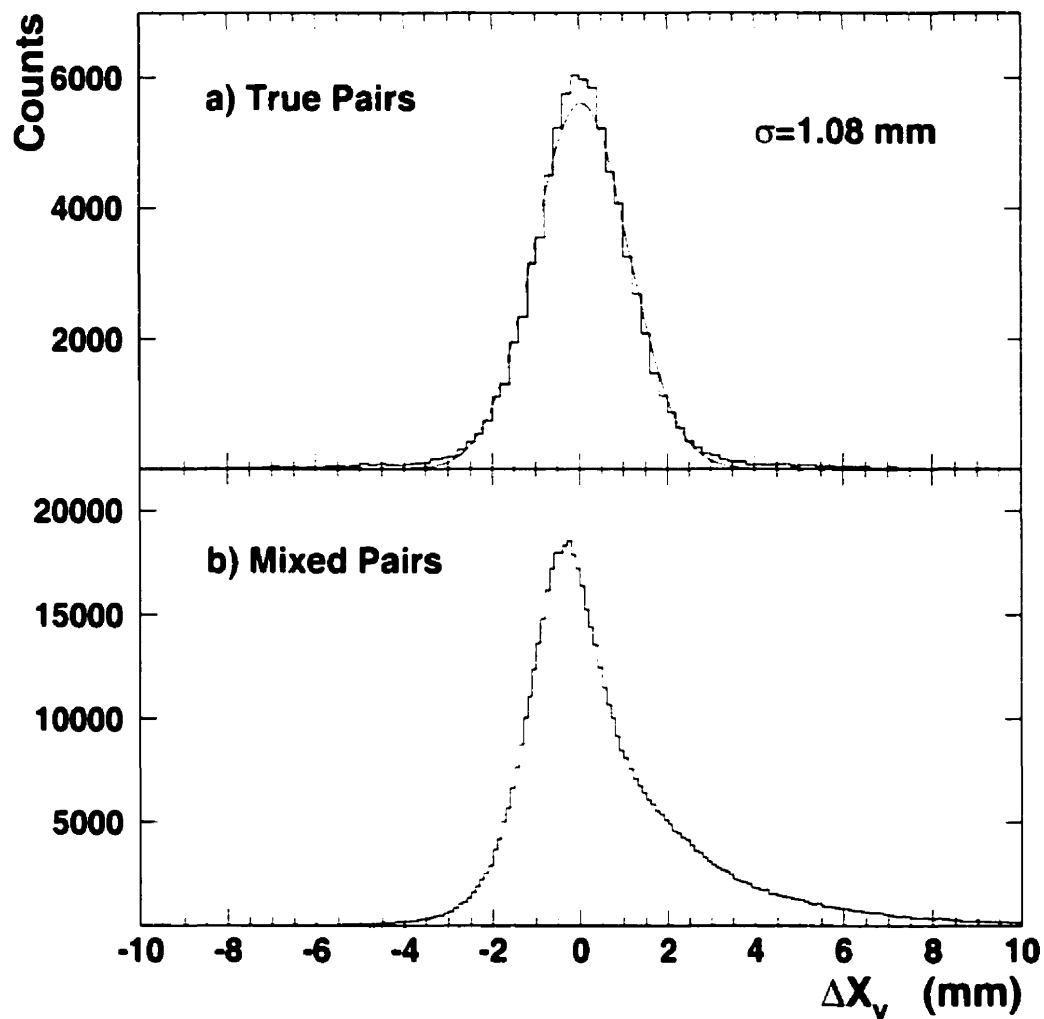


Figure 5.11: Investigation of the reconstructed momentum vector pointing, which is projected back to the target to obtain  $\Delta X_v$ . a). The calculated  $\Delta X_v$  distribution for true pairs; b). The calculated  $\Delta X_v$  distribution for mixed pairs.

# Chapter 6

## Lambda Identification

In the previous chapter we have performed a comprehensive Monte Carlo simulation on  $\Lambda$ 's decay and reconstruction. This provides us a solid guidance to study the lambda identification from the experimental data. In this chapter we will discuss the analysis of the data in detail. First we overview our analysis procedures, then look into each step of the analysis and last discuss the determination of the  $\Lambda$  yield.

### 6.1 Overview

Lambda identification is based on the invariant mass analysis of  $(p, \pi^-)$  pairs. We can calculate the invariant mass of a  $p$  and  $\pi^-$  pair from the measured momenta  $\mathbf{P}_p$  and  $\mathbf{P}_\pi$

$$M_{inv} = \sqrt{(e_p + e_\pi)^2 - (\mathbf{P}_p + \mathbf{P}_\pi)^2} \quad (6.1)$$

where the total energies of proton ( $e_p$ ) and pion ( $e_\pi$ ) are

$$e_p = \sqrt{P_p^2 + m_p^2} \quad \text{and} \quad e_\pi = \sqrt{P_\pi^2 + m_\pi^2}$$

Since our data analysis on lambda identification is performed on the reduced data (lean ntuples) where the secondary  $p$  and  $\pi^-$  tracks are indistinguishable from the

directly produced  $p$  and  $\pi^-$  tracks, the  $(p, \pi^-)$  combination will then result in a large combinatorial backgrounds. It is a great challenge to identify the  $\Lambda$ s from such large backgrounds. Traditionally, there are two approaches for lambda identification:

- **Direct approach:** In this approach, a set of pair cut parameters, similar to those described in section 5.4, are directly imposed on the pairs to reduce the combinatorial background. However, these pair cuts also reject a fraction of the true  $\Lambda$  samples. The optimization of the pair cuts are needed in this approach.
- **Mixed event method:** In this method the mixed  $(p, \pi^-)$  pairs from different events are used to precisely determine the combinatorial backgrounds. The mixed pair analysis parallels the true pair analysis. In such an approach the number of the pair cut parameters can be reduced and the cut criteria can be set more loosely. Of course, these pair cuts must be identical in both true pair and mixed pair analyses. As the combinatorial backgrounds is expected to be very precisely determined, the lambda spectrum can be obtained simply by subtracting the normalized mixed pair spectrum from the true pair spectrum. With this we can keep a larger fraction of the  $\Lambda$  samples. However, the determination of the backgrounds is very critical and may even failed if other sources of  $(p, \pi^-)$  correlations exist.

In our data analysis, we mainly employed the direct approach for  $\Lambda$ 's identification. The mixed event method are also used to look into the backgrounds, especially for the contribution of the correlated  $(p, \pi^-)$  pairs.

The overall procedure for lambda reconstruction is as follows: first making global event selection such as centrality cut, then selecting single  $p$  and  $\pi^-$  tracks by loose PID cuts. Once the single track are selected, then  $p$  and  $\pi^-$  pair are formed and the invariant mass of each pair is calculated. Then a set of pair cuts, as discussed in the previous chapter are used as filter to reduce the dominating combinatorial back-

grounds. After the filtering, the lambda signal (peak) is identifiable in the invariant mass distribution of the pairs and the lambda yield is obtained after the background subtraction.

## 6.2 Single Track Selection

As mentioned above, the reconstructing process starts from selecting single  $p$  and  $\pi^-$  tracks in each event. We use the PID cut, which has been described in 4.3.4, to help the track selection. Due to the decay effect of  $\Lambda$ 's, we have to make loose PID cuts to select all protons and pions. The cut criterion is chosen as

$$|m^2 - m_i^2| < 3.0\sigma_{m_i^2}, \quad i = p, \pi^- \quad (6.2)$$

where  $m^2$  is the measured squared mass and  $m_i^2$  is the peak value of the  $m^2$  distribution for each particle species. This cut is twice as wide as the standard PID cut shown in section 4.3.4. According to the acceptance calculations in section 5.2, the spectrometer favours the low  $p_t$  pions from the  $\Lambda$ 's decay. Since the light pion's trajectory is more strongly affected by the lambda decay, we further loose the cut criterion of Eq.( 6.2) for  $\pi^-$  at low momentum.

$$|m^2 - m_{\pi^-}^2| < 0.12 \text{ when } p_{\pi^-} < 3.5 \text{ GeV}/c \quad (6.3)$$

Like the normal PID cut procedure, the maximum momentum cut is also imposed on the single track selection. The momentum cuts are 15 GeV/c for protons and 10 GeV/c for  $\pi^-$ s. This implies that the reconstructed  $\Lambda$ 's are limited to about 25 GeV/c.

Since the TOFU pulse height cut helps distinguish the charge state of a particle, we also impose this cut on the single track selection. This type of cut improves the quality of the track selection.

When the single  $p$  and  $\pi^-$  tracks in an event have been selected, we store them in a stack and then combine them to form true  $(p, \pi^-)$  pairs. In the meantime, we also keep up the single track data of the latest 10 events for mixed event analysis. The mixed pairs are used for the combinatorial background studies.

## 6.3 Pair Reconstruction

Having done the single track selection, we can proceed to the pair reconstruction. The pair reconstruction is divided into two parallel processes, true pair and mixed pair. Each process has same contents, including upstream track reconstruction, decay vertex determination, backtracking correction and invariant mass calculation. In this section, we will mainly focus on the true pairs analysis.

### 6.3.1 Upstream Track Reconstruction

As described in section 4.3.1, QUANAH didn't use any tracking information upstream of the spectrometer magnet for track determination, and assumed that the track originates from the target. To reconstruct  $\Lambda$ , we have to redo the determination of the upstream track segment between the target and the spectrometer magnet by using the tracking information from the measurements of two VTX detectors. This procedure is referred as *upstream track reconstruction*.

Unfortunately, these two vertex chambers can only provide two measuring points for a track. Although two points are sufficient to determine a straight line, the resulting resolution in the track location is limited. Since the two vertex chambers were placed very close to each other, only about 25 cm apart, any uncertainties of the hit-position measurements in one of the detectors can lead to a large uncertainty on the track determination from the two measured points and thus on the decay vertex

location.

In order to improve the effective track resolution, we have used an extra point in the determination of the upstream track segment. As discussed in section 5.4, the track upstream and downstream of the the spectrometer magnet should match up at the center of magnet. We can choose this matching point (a virtual point) as the third point to aid the determination of the upstream track segment. The coordinate of this point is determined by a linear extrapolation of the downstream track segment which was well determined by DC2 and DC3 in QUANAH. Thus the position resolution of the matching point is determined by the position resolution of DC2 and DC3 ( $\sigma_x \sim 300 \mu\text{m}$ ,  $\sigma_y \sim 1 \text{ mm}$ ) [30]. Since this matching point is about 3.1 m downstream of the target (about 1 m away from the VTXA chamber), it does improve the determination of the upstream track segment.

Since in the direction perpendicular to the bend plane the track is not deflected by the magnetic field, it should be a straight line in the y-z plane from upstream to downstream. So a three-point linear fit is used to obtain y information of the upstream track, in which two points are from the measurements of two VTX chambers and the other point is selected from the measurement of either one of DC2, DC3 and TOFU, depending on which is available.

### 6.3.2 Decay Vertex Determination

Once the upstream track segments for  $p$  and  $\pi^-$  have been determined, we reconstruct the decay vertex ( $V_x, V_y, V_z$ ) for lambda. Since the tracking detectors have much better position resolution in the bend plane (x-z plane), the reconstruction is mainly performed in the bend plane of the spectrometer by finding the crossing point of the  $p$  and  $\pi^-$  pair tracks. This crossing point position determined the values  $V_x$  and  $V_z$  of the assumed decay vertex. Fig. 6.1 shows the obtained  $V_z$  distribution.

One can see that the reconstructed  $V_z$  distribution is as expected peaked at the target ( $V_z = 0$ ) with a long tail. The distribution has a very similar shape as the calculated distribution from uncorrelated pairs in the Monte Carlo simulation in Fig. 5.8. This indicates that the combinatorial background is dominant in the lambda reconstruction.

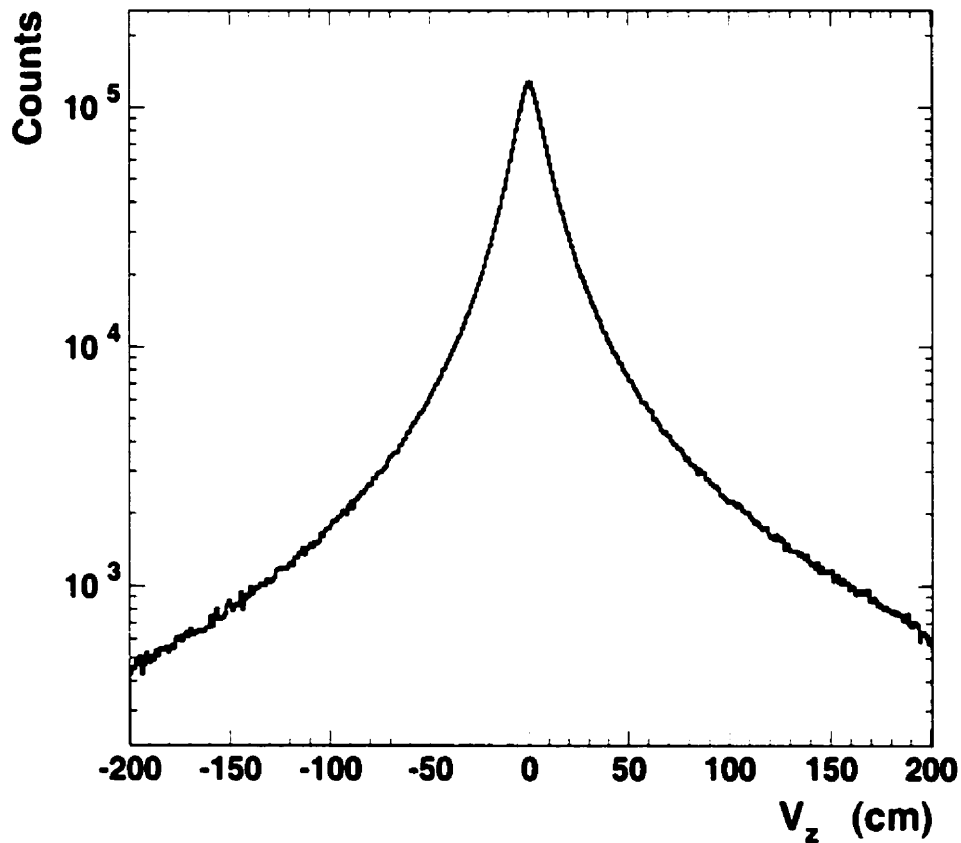


Figure 6.1: The reconstructed  $V_z$  distribution from the  $p$  and  $\pi^-$  pair tracks.

Because of the relatively poor resolution in the  $y$  direction, the  $V_y$  coordinate in the direction perpendicular to the bend plane, is determined in association with  $V_z$ . The  $V_y$  coordinate of the assumed vertex is taken as an average of the  $y$  coordinate

of the upstream  $p$  and  $\pi^-$  tracks at  $V_2$ .

When the decay vertex coordinates have been determined, the *backtracking* correction described at section 5.3 is used to recalculate the momenta of the secondary tracks. Then the invariant mass of each  $(p, \pi^-)$  pair is calculated according to the Eq. 6.1. Some pair cuts have to be made to identify the lambda peak in the invariant mass spectrum of  $(p, \pi^-)$  pairs. We will discuss these pair cuts in the following section.

## 6.4 Pair Cuts

As stated before, the large combinatorial background dominates in the pair reconstruction. In order to identify the lambda signal from the huge background, a set of pair cuts (five types) described in section 5.4 are used in the data analysis. As shown in Fig. 6.2(a), without any pair cuts there is no lambda signal visible on the invariant mass spectrum due to the large combinatorial background. After we imposed the  $V_2$  cut ( $25 \text{ cm} < V_2 < 180 \text{ cm}$ ) on the true pair analysis, the combinatorial background is reduced significantly so that the lambda signal comes up as a little bump in the invariant mass spectrum (see Fig. 6.2(b)). When we include the requirement that tracks pointing away from the target, it further reduces the combinatorial background dramatically so that the lambda signal (peak) shows up nicely in the invariant mass spectrum (see Fig. 6.2(c)). Therefore the cut on  $V_2$  and requiring pair tracks pointing away from the target are the most essential cuts to reduce the large combinatorial background. This is consistent with what we obtained from the Monte Carlo simulation in section 5.4.

On the other hand, these cuts also have an effect to remove a fraction of  $\Lambda$ s from the samples. So optimizing these cuts is necessary in order to keep maximum statistics. Unfortunately, these pair cut parameters are highly correlated, which makes

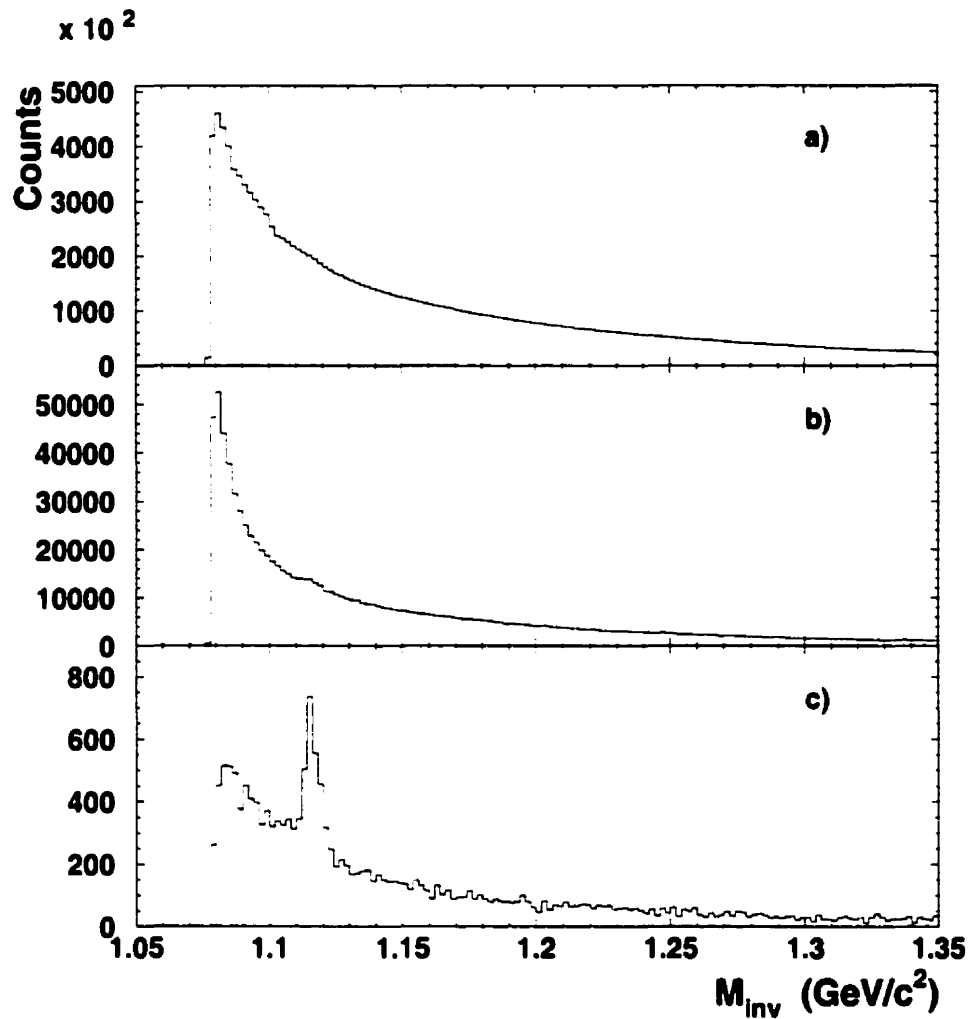


Figure 6.2: The invariant mass distributions. a) before pair cuts; b) without the cut of pair tracks away-from-target; c) including the cut of pair tracks away-from-target.

the optimization difficult. In [86] it is discussed how to deal with such optimization of multi-correlated parameters by a neural network approach. Due to the large data samples it was judged that this approach would be too much time-consuming in our case. So we develop a simpler approach instead.

Our approach is based on the investigations of Monte Carlo simulation described

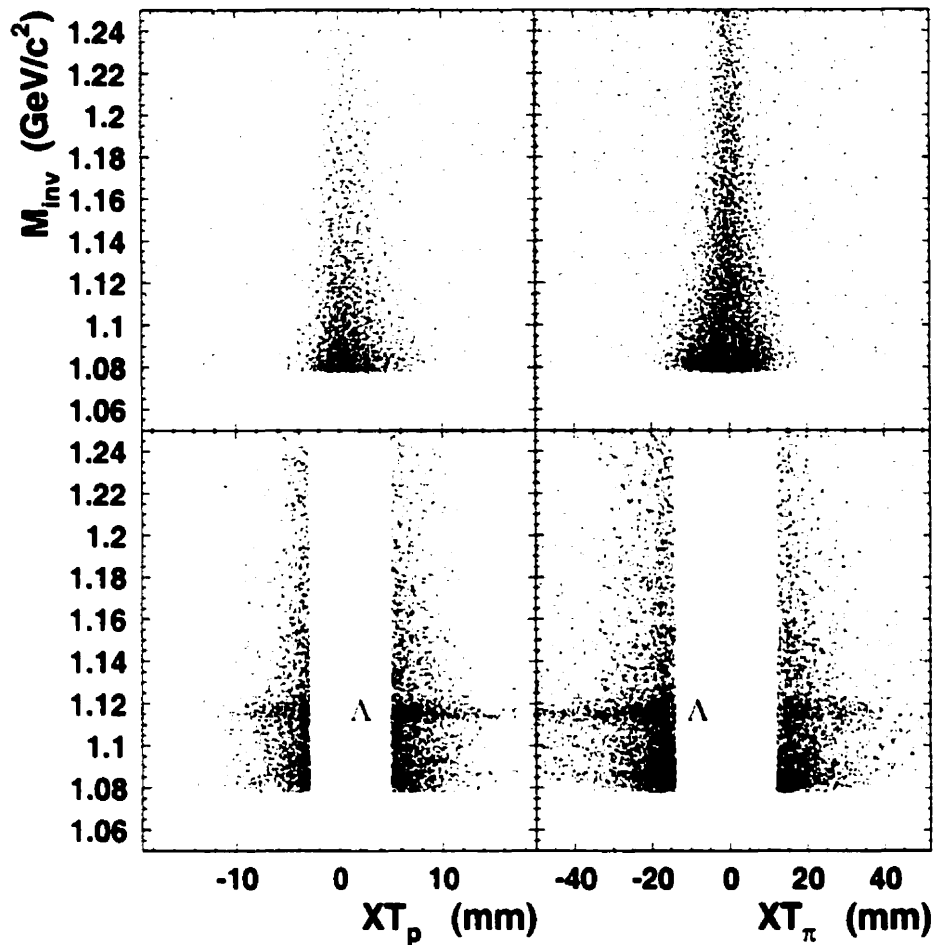


Figure 6.3: Scattering plots of invariant mass versus the cut parameters of pair tracks pointing away from target. upper panels: before cut; lower panels: after cut ( $XT_p < -3$  mm or  $XT_p > 5$  mm and  $XT_\pi < -15$  mm or  $XT_\pi > 13$  mm).

in section 5.4. Actually, the  $V_2$  cut parameter has been determined there. So we first fix the  $V_2$  and the minimum track separation cuts, then set others with coarse cuts according to the deduced cut criteria from the Monte Carlo simulation, and last look into the correlation of each cut parameter with invariant mass spectrum to fine tune

the cut criteria. Fig. 6.3 illustrates the determination of the cut criteria of pair tracks pointing away from the target. The cut parameters are  $.XT_p < -3$  mm or  $.XT_p > 5$  mm and  $.XT_\pi < -15$  mm or  $.XT_\pi > 13$  mm. One can see that the lambda band shows up after imposing the cut of pair tracks pointing away from the target since the parameters  $.XT_p$  and  $.XT_\pi$  for lambda are correlated.

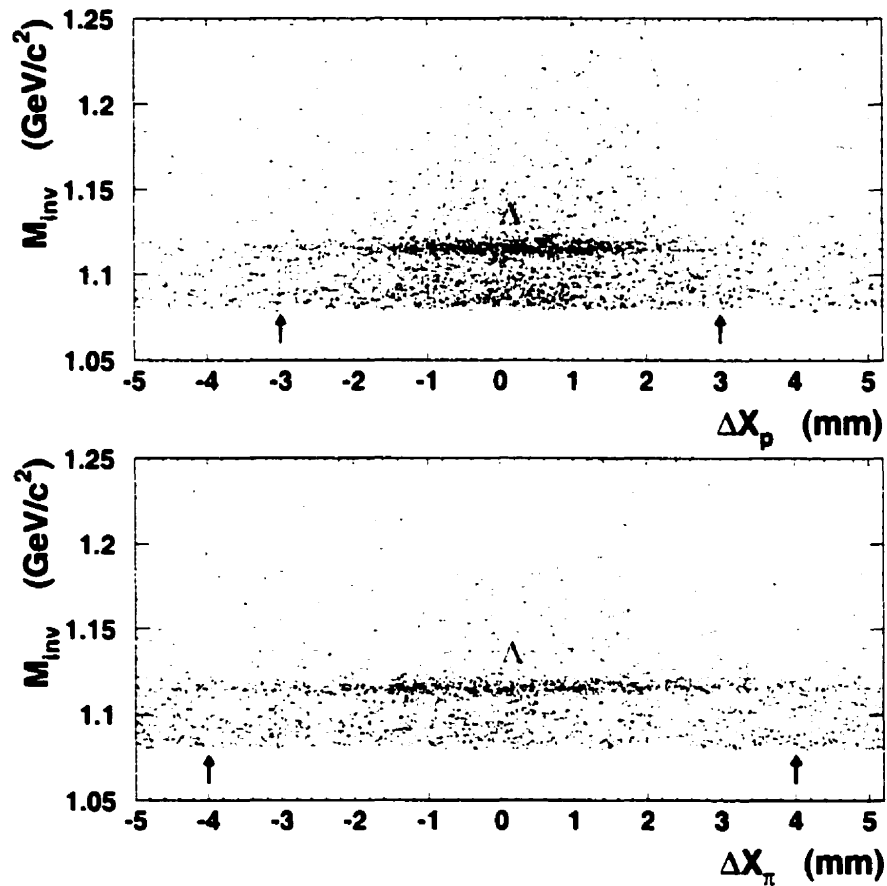


Figure 6.4: Scattering plot of invariant mass versus track matching cut parameters. The cuts on  $V_2$  and pair tracks pointing away from the target are included. The arrows mark the cut positions.

When the cut criteria on  $V_2$  and pair tracks pointing away from the target have

been determined, let's look into the cut parameters for track matching between upstream and downstream. Fig. 6.4 shows the scattering plot of invariant mass versus track matching parameters. The cuts on  $V_z$  and pair tracks pointing away from the target have been already included. One can see that the lambda bands are centered at  $\Delta X_p=0$  and  $\Delta X_\pi=0$ . In the final analysis we set a loose cut criteria at  $|\Delta X_p| < 3$  mm and  $|\Delta X_\pi| < 4$  mm.

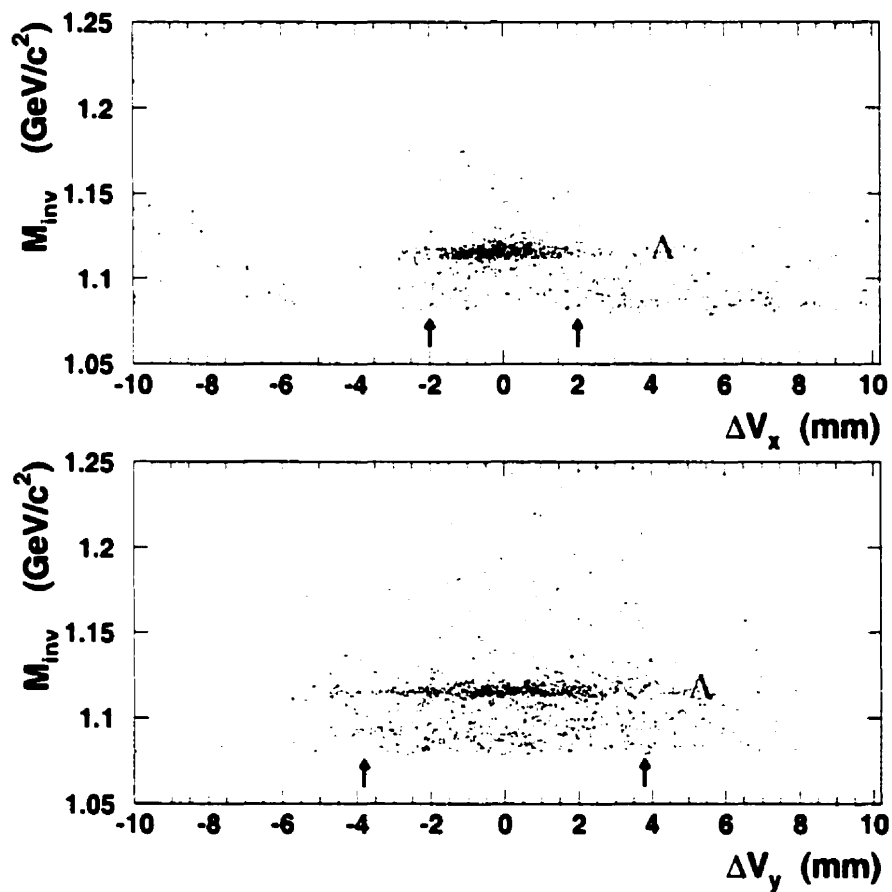


Figure 6.5: Scattering plot of invariant mass versus the cut parameter of reconstructed momentum vector pointing back to the target. The arrows mark the cut positions.

Fig. 6.5 shows the scattering plot of invariant mass versus the parameters of

reconstructed pair momentum vector pointing back to the target. The previous four types of pair cuts have been already included. As expected, the lambda samples are indeed concentrated on the target ( $\Delta V_x=0$  and  $\Delta V_y=0$ ). We set the cut criteria at  $|\Delta V_x| < 2$  mm and  $|\Delta V_y| < 3.8$  mm. This cut has a similar effect as the matching cut to reduce the background produced by misidentified tracks.

The pair cut criteria are summarized as follows:

- Minimum pair-track separations:
  - $\Delta X_{DC2} > 1.2$  cm
  - $\Delta X_{DC3} > 2.5$  cm
  - $\Delta X_{TOFU} > 1$  slat
- Distance  $V_z$  of decay vertex from the target:
  - $25$  cm  $< V_z < 180$  cm
- Pair tracks pointing away from the target:
  - $X_{T_p} < -3$  mm and  $X_{T_p} > 5$  mm
  - $X_{T_\pi} < -15$  mm and  $X_{T_\pi} > 13$  mm
- Matching between upstream and downstream tracks:
  - $|\Delta X_p| < 3$  mm
  - $|\Delta X_\pi| < 4$  mm
- Reconstructed pair momentum vector pointing back to target:
  - $|\Delta X_v| < 2.0$  mm
  - $|\Delta Y_v| < 3.8$  mm

After the pair cuts filtering, the large background has been dramatically reduced so that the  $\Lambda$  signal (peak) becomes well identifiable in the invariant mass distribution (see Fig. 6.6). Without *backtracking* correction, the lambda is peaked at  $1.113$  GeV/c<sup>2</sup>

with a resolution of  $3.94 \text{ MeV}/c^2$ . After the *backtracking* correction the lambda peak shifts to the known lambda mass  $1.116 \text{ GeV}/c^2$  with a better resolution of  $3.32 \text{ MeV}/c^2$ . The *backtracking* correction also significantly improves the lambda peak to background ratio. Note that the observed resolution of the lambda peak is very consistent with the results of the Monte Carlo simulation (see Fig. 5.6).

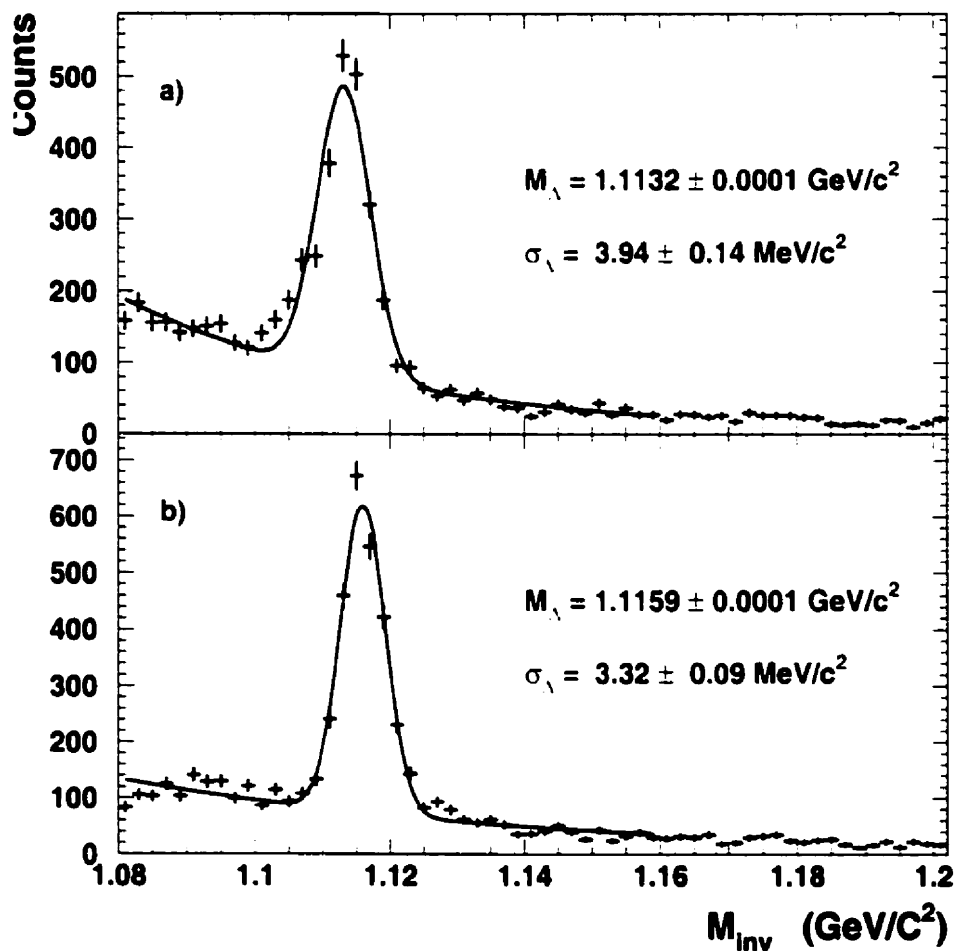


Figure 6.6: Invariant mass distribution of true  $\pi\pi^-$  pairs. a) invariant mass distribution before backtracking correction; b) invariant mass distribution after backtracking correction.

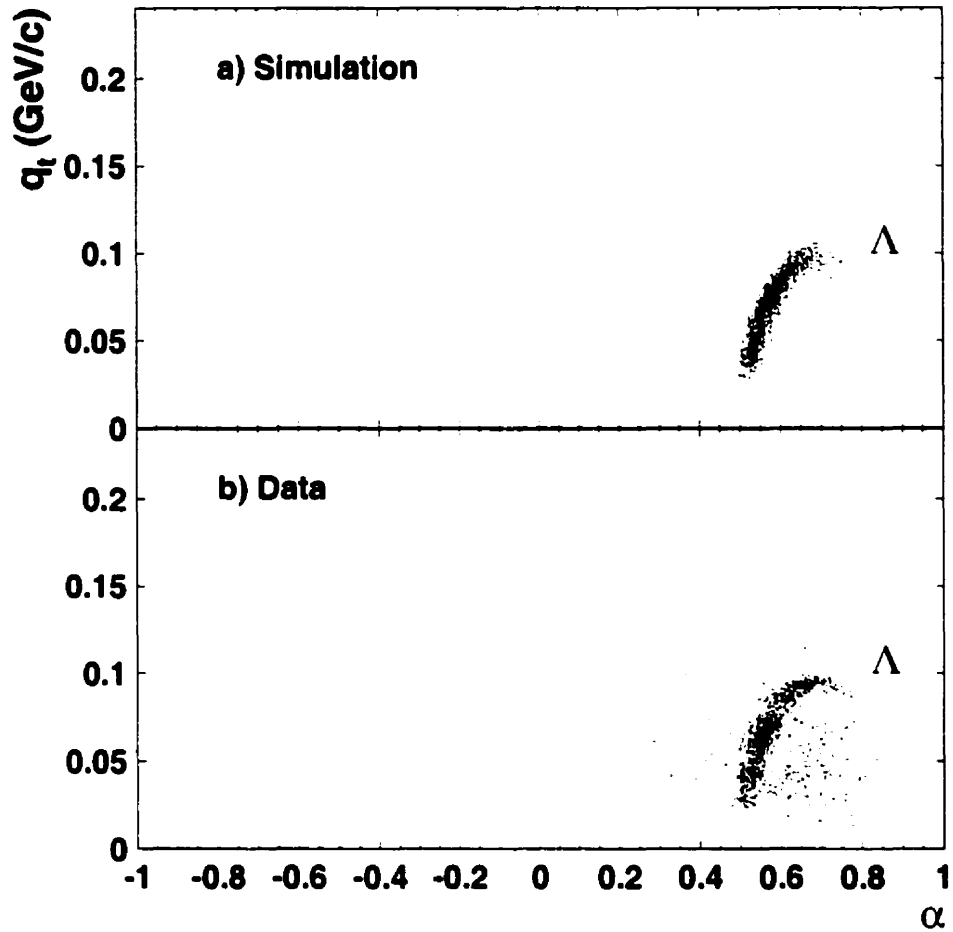


Figure 6.7: Podolanski-Armenteros plot for lambda identification. a) The calculated  $\Lambda$ s in the Monte Carlo simulation described in chapter 5. b) The obtained  $\Lambda$ s in the data analysis. Identical cut parameters are used in both the data and simulation.

We can check the result of lambda identification from another angle. Fig. 6.7 shows the Podolanski-Armenteros plot [87] after the above pair cuts. In this plot, the Podolanski-Armenteros variable  $\alpha$  is defined as:

$$\alpha = \frac{q_L^+ - q_L^-}{q_L^+ + q_L^-} \quad (6.4)$$

where  $q_L^+$  and  $q_L^-$  are the momentum of the positive and negative tracks from the lambda decay parallel to the direction of the lambda momentum, respectively.  $q_t$  is the momentum of the pair tracks perpendicular to the lambda emitting direction. The Podolanski-Armenteros plot basically describes the relation between  $\cos(\theta_{cm})$  and  $\sin(\theta_{cm})$ , where  $\theta_{cm}$  is the decay angle in the center-of-mass frame. The data and the results from the Monte Carlo simulation are in good agreement.

## 6.5 Background Subtraction

Although a lambda signal has been well isolated from the large backgrounds (see Fig. 6.6(b)), there are still some amounts of backgrounds underneath the  $\Lambda$ 's peak. We have to subtract these backgrounds before further physics analysis. In this section, we discuss the background subtraction.

Before doing the background subtraction, it is necessary to look into the sources of the backgrounds in the invariant mass distribution. Besides the dominant ( $p, \pi^-$ ) combinatorial backgrounds which pass through the pair cuts, there is another contribution from  $p$  and  $\pi^-$  pair correlation. Fig. 6.8 shows the normalized one-dimensional correlation function obtained from the  $p$  and  $\pi^-$  pairs used in the lambda reconstruction. The relative momentum  $q$  was evaluated in the center-of-mass of the pair, which is directly related to the invariant mass  $M_{inv}$  of the pair. One can see that the HBT-type correlation of  $p$  and  $\pi^-$  pairs has a very strong signal at  $q \sim 0$  related to the source size, which is mainly due to the Coulomb interaction between the pair particles. The small bump at  $q = 0.2$  GeV/ $c$  is due to the correlated  $p$  and  $\pi^-$  pairs from lambda decay. Since the HBT-type correlation [88] is mainly concentrated at  $q < 0.1$  GeV/ $c$ , equivalent to  $M_{inv} < 1.11$  GeV/ $c^2$ , it does affect the lambda peak in the invariant mass spectrum, especially at the left edge of the lambda peak. So we definitely cannot neglect it in the background subtraction.

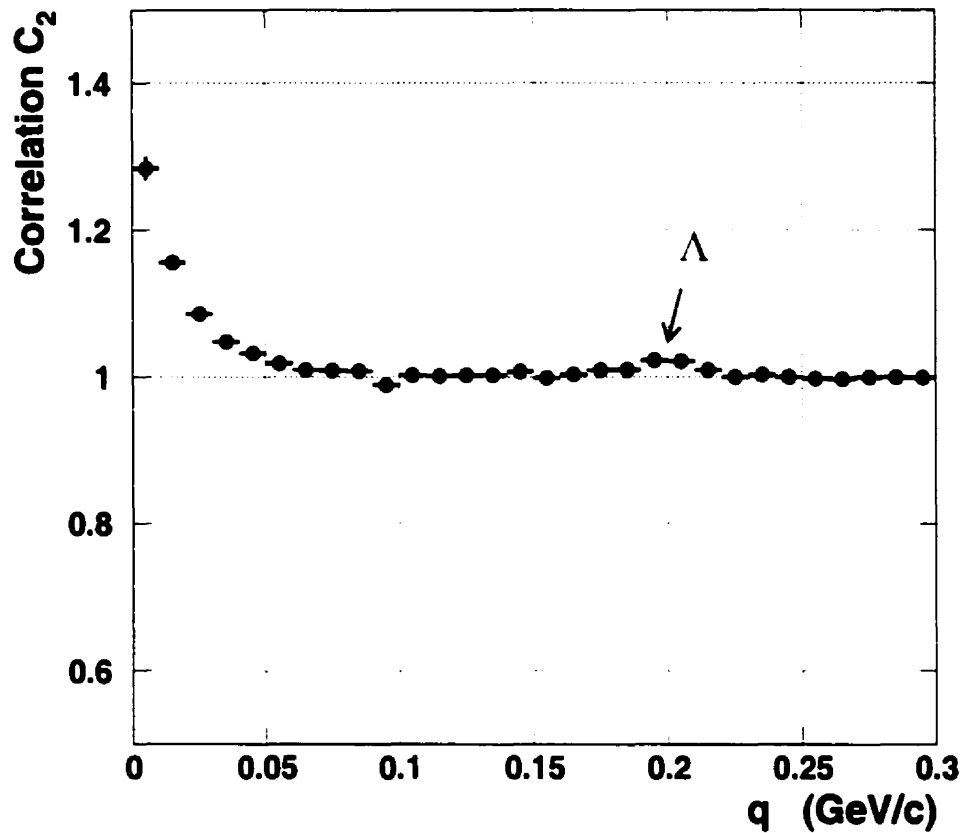


Figure 6.8: One-dimensional correlation function  $C_2$  versus  $p$  and  $\pi^-$  relative momentum  $q$  in the center-of-mass of pairs. Experimentally the definition of the correlation function is  $C_2(q) = N_{true}/N_{false}$ .

We have attempted to estimate the background by using mixed pair analysis. Fig. 6.9 shows the obtained invariant mass distributions for true pairs (solid histogram) and mixed pairs (dash histogram). The mixed pair's distribution was normalized with respect to the tail of the true pair distribution. This approach seems to underestimate the background at low  $M_{inv}$  in agreement with Fig. 6.8. So because of the effect and the relatively limited statistics, we have used a simpler method to

subtract the remaining background.

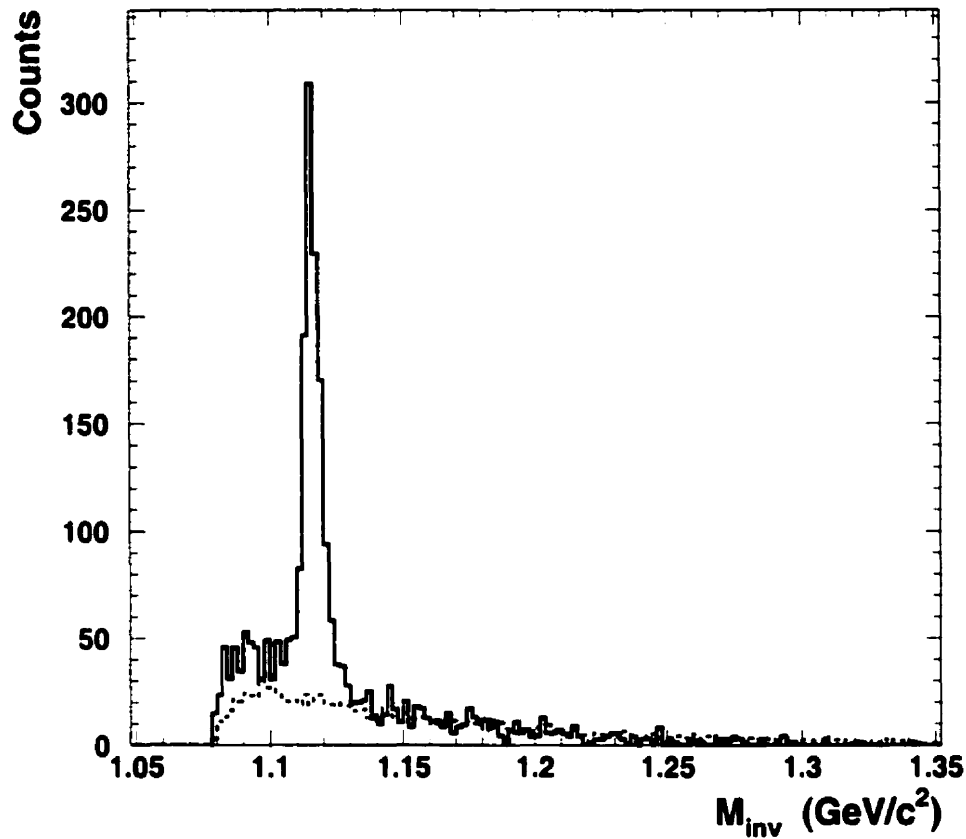


Figure 6.9: Background subtraction by mixed pair method. The solid histogram represents the true pair's distribution, the dash histogram is the normalized distribution from mixed pairs to estimate the background.

In principle, we can use fitting method to extract the yield of  $\Lambda$ s from the invariant mass spectrum. But the fitting method requires enough statistics for working well. In the invariant mass spectrum the statistics of  $\Lambda$ 's are usually small at high  $p_t$  so that the fitting often fails in those regions. To overcome the problem due to low statistics, we instead use a linear interpolation method for the background subtraction (see

Fig. 6.10).

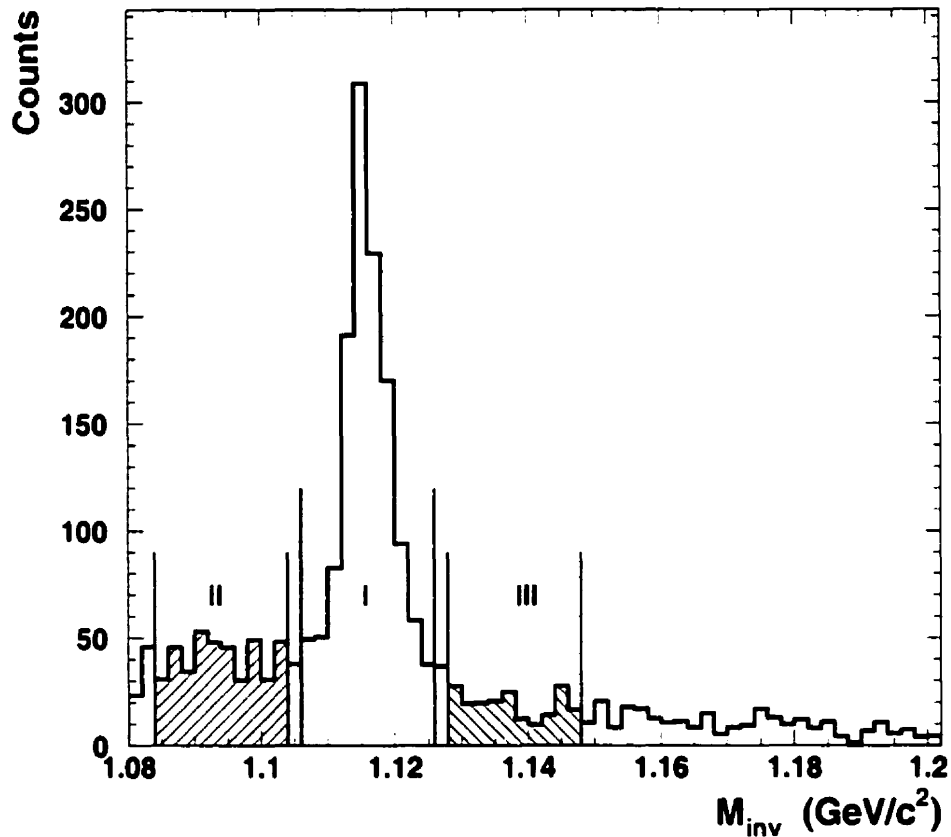


Figure 6.10: Background subtraction by linear interpolation.

In the range of  $1.084 < M_{inv} < 1.16 \text{ GeV}/c^2$ , the background distribution is approximately linear. We set three windows with equal width in the invariant mass spectrum. Window *I* that contains the lambda particles is set in the range of  $1.106 < M_{inv} < 1.126 \text{ GeV}/c^2$ , called  $\Lambda$  window. Window *II* and *III*, sandwiching the  $\Lambda$  window, are used as references of backgrounds. Further the net amount of the  $\Lambda$ s is obtained by subtracting the background from the lambda window. We have examined this method. It performs consistently and gives a result as good as the

fitting method within statistical errors. So we mainly use the linear interpolation method for the background subtraction in our data analysis for lambda spectra.

After subtracting the background underneath the lambda peak, we have obtained 2644  $\Lambda$ s from 31.918.757 central events ( $< 10\% \sigma_{geo}$ ). We will use these identified  $\Lambda$ s to construct lambda spectra discussed in the next chapter.

## 6.6 Corrections of Acceptance and Pair Cuts

After the filtering of the pair cuts, the obtained phase space acceptance diagram for lambda is shown in Fig. 6.11. Our measurements have a coverage in rapidity range of  $2.2 < y < 3.4$ . The  $\Lambda$ s in low  $p_t$  ( $< 0.15$  GeV/c) are not reconstructed, because of the dead zones in the VTX detectors near the beam axis.

To reconstruct the lambda spectra in the covered phase space, the measured data needs to be corrected for the spectrometer acceptance and a variety of cuts. The single track efficiency has been discussed in section 4.5.1. But the efficiency of VTX detectors is missed there. We have studied the efficiency of VTX detectors by looking into the proton ratio with/without the VTX cut. The obtained efficiency of VTX detectors is about 85% for single track in the sensitive area of the detectors. This is in good agreement with the result of Bersch's studies [69]. The effect of the dead regions due to beam hole (see Table 4.6) are included in the acceptance correction. We used these estimations to correct the single track efficiencies in pair reconstruction.

The corrections of acceptance for lambda with the pair cuts included are obtained from the Monte Carlo kinematic simulation described in chapter 5. Fig. 6.12 shows the calculated acceptance for lambda as a function of rapidity and  $p_t$ . The set of pair cut parameters listed in section 6.4 has been included in calculations. We divided the measured rapidity range ( $2.2 < y < 3.4$ ) into four rapidity bins with equal width. One can see that the E877 spectrometer has a very low acceptance (under  $10^{-3}$ ) for

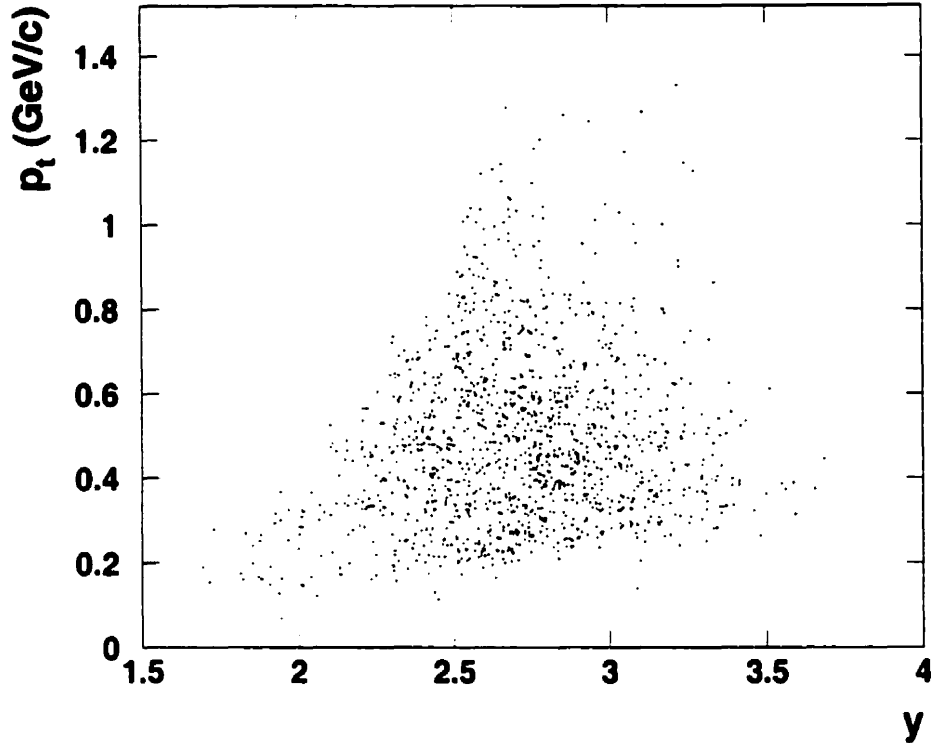


Figure 6.11: The measured range for  $\Lambda$ 's in phase space after the pair cuts.

lambda after the pair cuts. In generally, the spectrometer favors the  $\Lambda$ s at forward rapidities; especially in beam rapidity region ( $3.1 < y < 3.4$ ) there is relatively high reconstructing efficiency. The structures that are found through the acceptance distribution of  $\Lambda$ 's originate from the dead sections of the individual tracking detectors.

These corrections introduce some uncertainties. The acceptance calculation uncertainty is of the order of 10%. The estimation of the tracking efficiency of the VTX detectors has an uncertainty about 5%. The background subtraction to extract lambda yield introduces an error about 5%. We use the single track efficiency to estimate the efficiency of the pair tracks. It results in another uncertainty for the

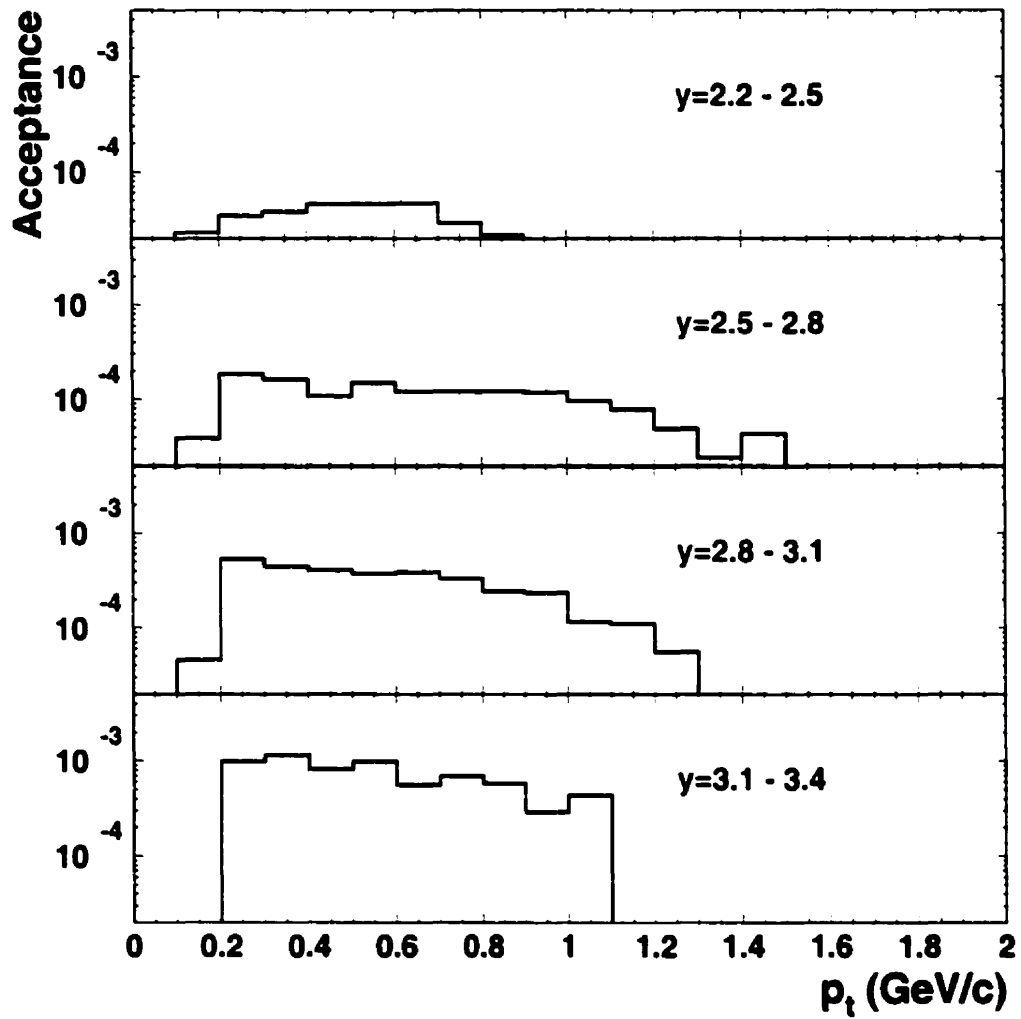


Figure 6.12: Acceptance corrections for  $\Lambda$ 's with pair cuts in four rapidity bins.

corrections. The overall systematic uncertainty is of the order of 15%.

# Chapter 7

## Results and Discussions

In this chapter, we present our results on lambda production in Au+Au collisions at 11.5 A·GeV/c. We begin by discussing the results on the proton and pion spectra, which are intended to establish the quality of our analysis procedure. Then the double differential multiplicities for lambda as a function of centrality will be presented. Lambda yield and  $dN/dy$  distribution are obtained by integration of the experimental  $m_t$  spectra. Finally, the azimuthally anisotropic flow of  $\Lambda$ 's will be presented and discussed. All the experimental results on  $\Lambda$ 's will be compared with the predictions of the Relativistic Quantum Molecular Dynamics (RQMD) model [43].

### 7.1 Proton and Pion Spectra

The spectra of protons and pions produced in Au+Au collisions at AGS energies have been extensively studied by the collaborations E877 [27, 28] and E866 [14]. The E877 experiment made a systematic study of the proton and pion spectra from the data in the 1993 run [28]. Those data were obtained at a bombarding energy of 10.8 A·GeV/c, slightly lower than the beam energy in the 1995 run. To examine the consistence of our data analysis, we have constructed the proton and pion spectra

from the present data set and compare the results to those obtained from 1993 data set. Since the E866 experiment had a complementary coverage in rapidity to that of E877, we also include the E866 data in the discussion.

To produce particle spectra, the particle identification (PID) cuts, shown in Fig. 4.12, were used to select the particle species. The TOFU pulse height cut, shown in Fig. 4.9, was used to select the charge state of the particle. The efficiency and corrections described in section 4.5 are used to obtain the invariant multiplicity distribution of the particles presented here.

### 7.1.1 Inclusive Proton Spectra

The inclusive transverse mass spectra of protons for the most central  $4\% \sigma_{geo}$  are shown in Fig. 7.1. The data were divided into constant  $p_t$  bins of 20 MeV and rapidity bins of 0.1 unit width. The spectra are plotted as  $1/m_t^2 \cdot d^2N/dm_t dy$  vs  $m_t - m_p$ , a representation in which a thermal (Boltzmann type) distribution would be represented as a pure exponential. For comparison we plotted the 1995 data (solid points) and the 1993 data (open points) together. The agreement between the two data sets is very good. In the 1995 data, there is a gap in each spectrum at very low  $p_t$  resulting from the effect of the dead sections in the tracking detectors where the Au beam passed through. Since the spectrometer was operated with a negative polarity magnetic field, the dead zones affect mainly the measurements of positive charged particles such as proton.

The overall behavior of the transverse mass spectra is well described by exponential Boltzmann fits (solid lines). Around beam rapidity ( $y_{beam}=3.2$ ), a steeper rise shows up at low  $p_t$  which is attributed from the projectile spectators. Detailed discussions about the effect of the spectators can be found in [28]. Here our interest is on the thermal component. To extract the inverse slope parameter, a single exponential

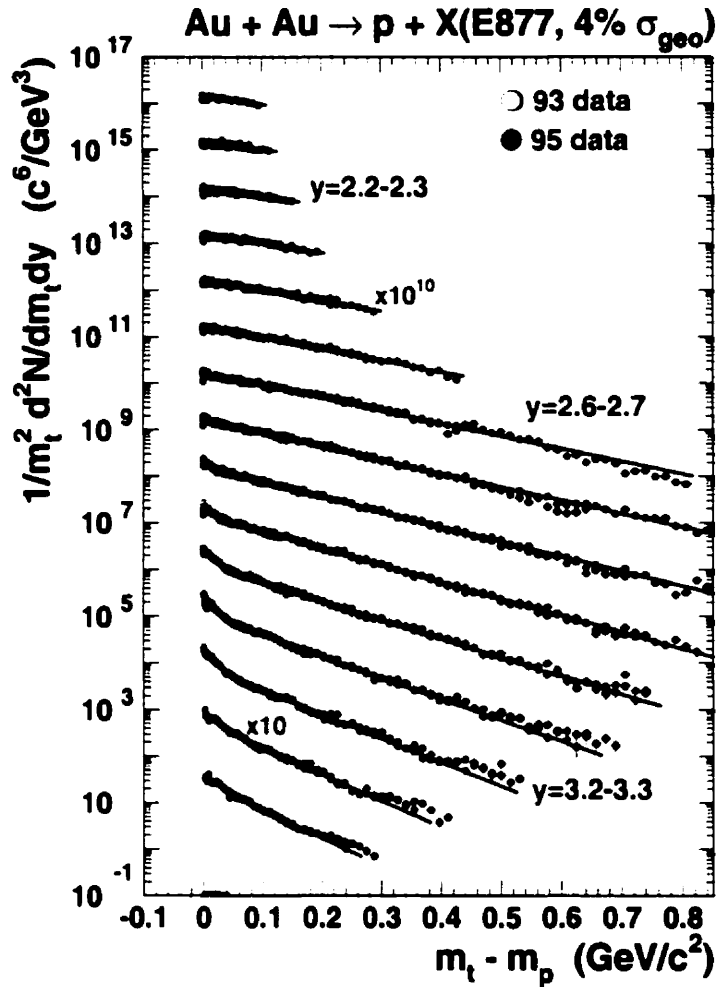


Figure 7.1: Measured proton transverse mass spectra in Au+Au collisions for the most central 4% of  $\sigma_{geo}$ . Starting with rapidity bin  $y = 3.3 - 3.4$ , the spectra have been multiplied by successively increasing powers of 10. Errors are statistics. The solid circle represents the 95 data while the open circle denotes the 93 data [28]. Full lines are the results of Boltzmann fits to the data.

fit was performed beginning at  $m_t - m_p = 0.1 \text{ GeV}/c^2$  for rapidities  $y=2.9$  to 3.4. For other rapidities the fits began right after the “beam hole”. The rapidity dependence of the inverse slope parameters  $T_B$  are presented in Fig. 7.2. Since the reaction system

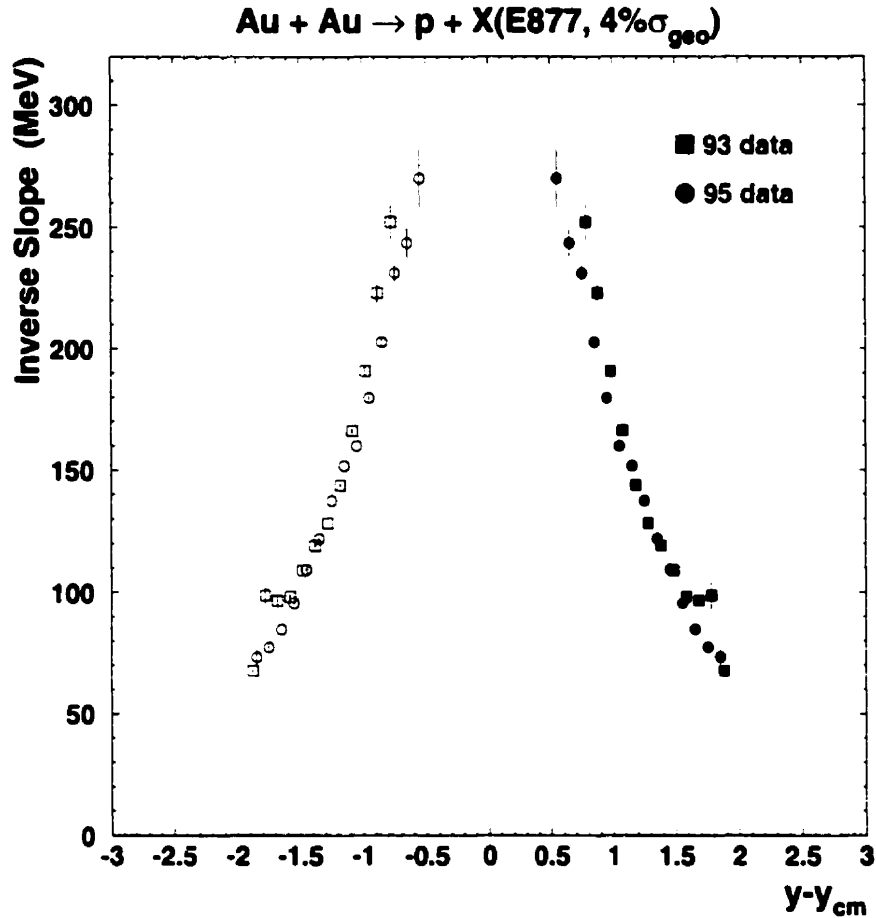


Figure 7.2: Proton inverse slope parameters as a function of rapidity. The data are represented by solid symbols and reflected about mid-rapidity (open symbols).

is symmetric, the measured values (solid symbols) are reflected about mid-rapidity to better visualize the behavior of the data. Both the 95 data and the 93 data agree very well. The values of the inverse slope parameters increase progressively from the beam rapidity to the mid-rapidity. A possible explanation of the large inverse parameter values at mid-rapidity is the effect of the hydrodynamical collective flow, which add a common velocity to the thermal motion during the fireball expansion [16].

The rapidity density distribution of protons is expected to provide important

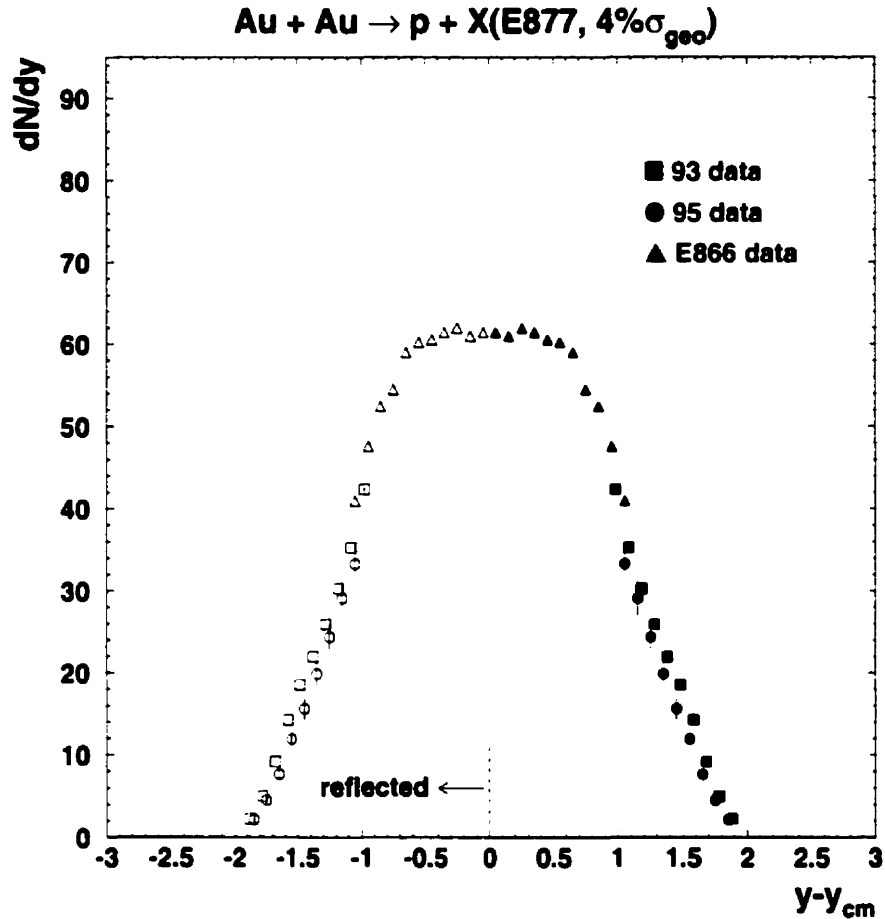


Figure 7.3: Rapidity distribution of protons for the most central Au+Au collisions. The solid symbols are the measured points and the open symbols are obtained from reflecting the measurement about  $y_{cm}$ .

information about the baryon stopping of the reaction system. The measured proton rapidity distribution  $dN/dy$  is shown in Fig. 7.3. The distribution is obtained by integrating the transverse mass spectra where data available and extrapolating to  $p_t = \infty$  using the exponential Boltzmann fits (see Fig. 7.1). The results from the 95 data and the 93 data agree well within the systematic errors. Besides a comparison with the results from the E877 1993 data, we also included the results from the E866

experiment [14]. This results in a complete proton  $dN/dy$  distribution in central Au+Au collisions at AGS energies. The proton seems to have a flat  $dN/dy$  at mid-rapidity, which is not consistent with the predictions of the RQMD that gives a more Gaussian-like distribution [28]. The width of the distribution is significantly narrower than that observed from Si+Au system [30, 31]. This indicates that a large degree of stopping and hence a state of high baryon density has been formed at the central Au+Au collisions at AGS energies. The model calculations indicate that the density is about 8 times normal nuclear density [14].

### 7.1.2 Inclusive Pion Spectra

Pions are produced copiously at AGS energies. Because of their light masses and large cross sections for interaction in nuclear matter they are expected to be thermalized easily. Since the transverse flow of pions is very weak [42], their spectra are not as affected as those of heavier particles by collective flow and thus they are good probes for studying thermal properties at freeze-out.

The inclusive pion  $m_t$  spectra measured in the most central ( $4\% \sigma_{geo}$ ) collisions are presented in Fig. 7.4. Like the proton  $m_t$  spectra, the effect of the “beam hole” also appeared on the  $\pi^+$  spectra. Both the 95 data and 93 data are very consistent. Overall, the transverse mass spectra also exhibit thermal shapes with increasing inverse slope values as approaching mid-rapidity. A clear enhancement above the pure exponential (thermal source) fits (solid lines) are observed for  $m_t - m_\pi < 0.2 \text{ GeV}/c^2$ . A similar effect was already observed for Si+Pb system and was explained as the contribution from the decay pions of  $\Delta$  resonances [89]. To further test this hypothesis we have made an attempt to reconstruct  $\Delta^{++}$  via its decay to  $p\pi^+$  pairs. This analysis is presented in Appendix B.

A single exponential fit was performed to the data above  $m_t - m_\pi = 0.2 \text{ GeV}/c^2$

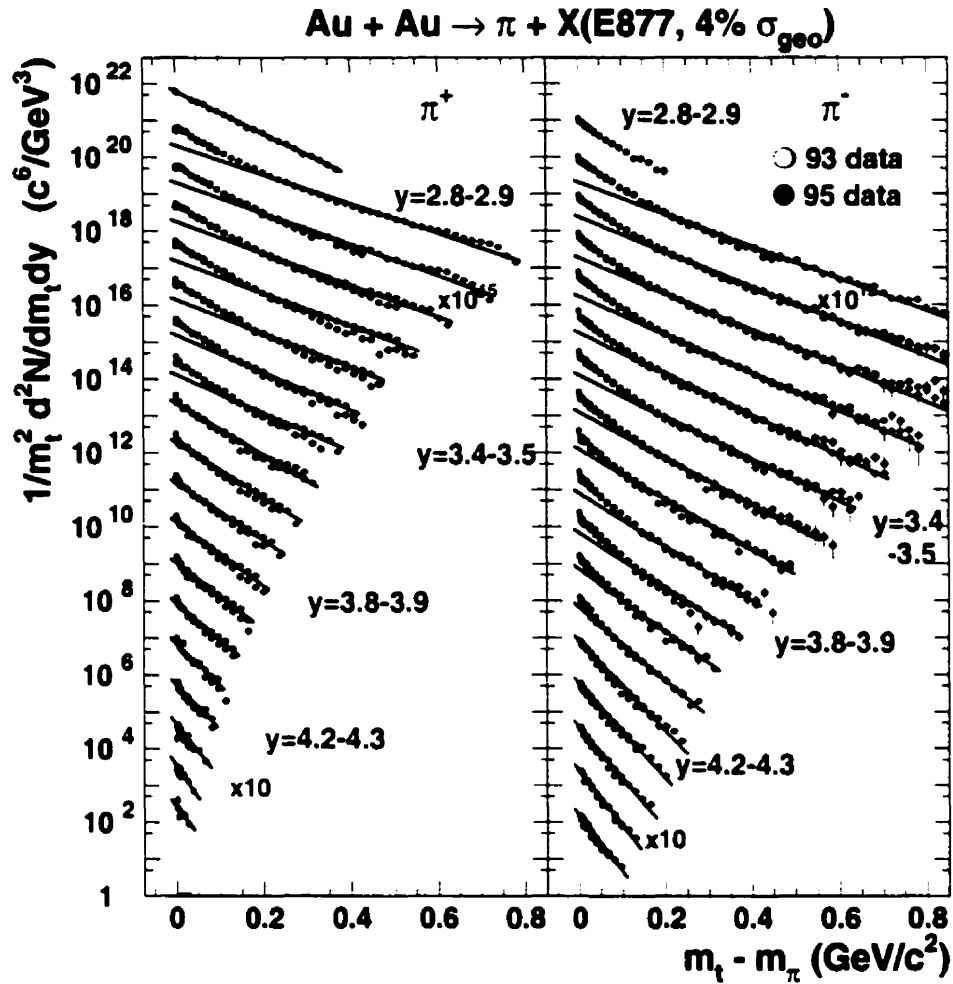


Figure 7.4: Pion transverse mass spectra in Au+Au collisions for the most central 4% of  $\sigma_{geo}$ . Starting with rapidity bin  $y = 4.4 - 4.5$ , the spectra have been multiplied by successively increasing powers of 10. Errors are statistics. The solid circle represents the 95 data while the open circle denotes the 93 data [28]. Full lines are the results of Boltzmann fits to the data.

in the rapidity bins where available ( $2.8 < y < 3.5$  for  $\pi^+$  and  $2.8 < y < 4.0$  for  $\pi^-$ ) and starting from  $m_t - m_\pi = 0 GeV/c^2$  at other rapidities. The obtained inverse slope parameters as a function of rapidity are presented in Fig. 7.5. The 93 and 95

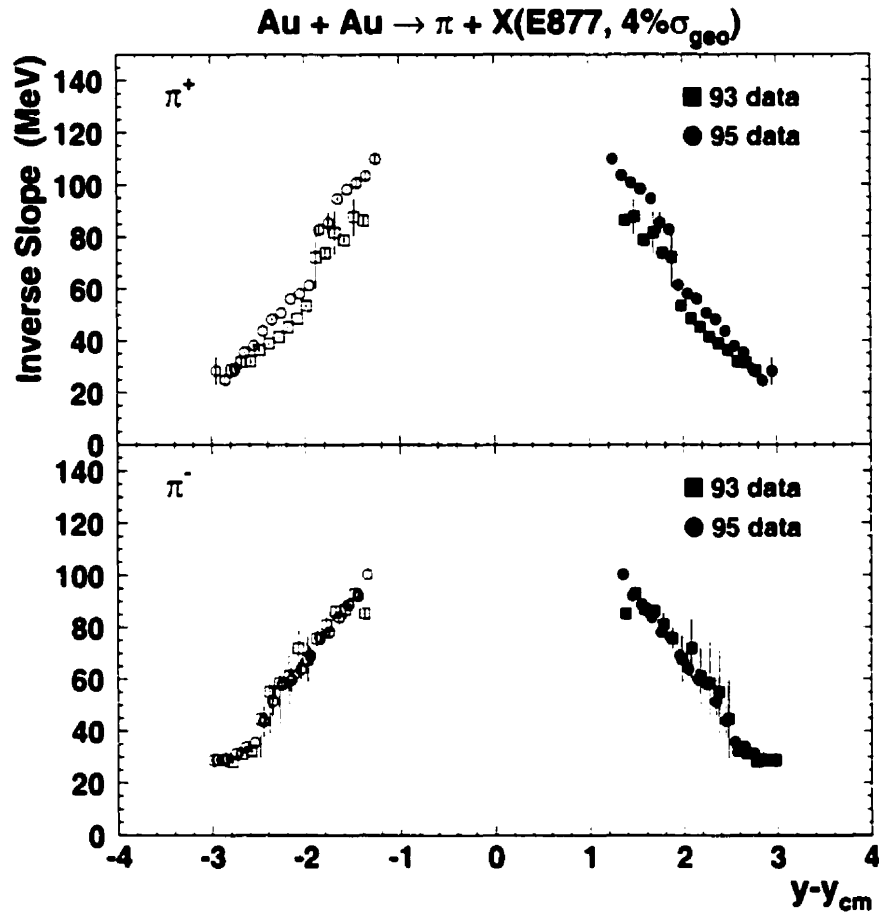


Figure 7.5: Pion inverse slope parameters as a function of rapidity. The data are presented by solid symbols and reflected about mid-rapidity (open symbols).

data are in good agreement. The only difference is that in the case of  $\pi^+$  the 95 data shows somewhat higher temperature than the 93 data does.

The spectra, in a similar manner to the protons, are integrated over  $m_t$  in each rapidity bin to obtain the rapidity distribution. The resulting rapidity distributions are presented in Fig. 7.6. Besides a comparison with the results from 1993 E877 data, we also added the results from the E866 experiment [14] into the plot. This results in a nearly complete pion  $dN/dy$  distributions in central Au+Au collisions at AGS

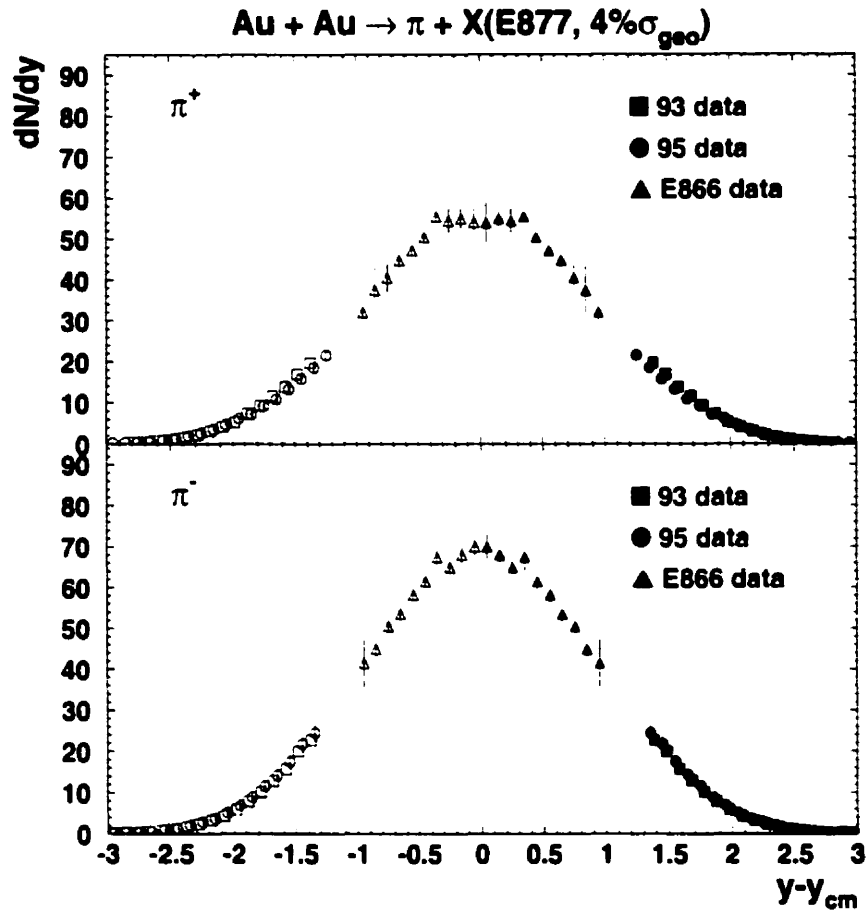


Figure 7.6: Rapidity distribution of pions for the most central Au+Au collisions. The solid symbols are the measured points and the open symbols are obtained from reflecting the measurement about  $y - y_{cm} = 0$ .

energies.

In summary, we have constructed proton and pion spectra for the most central Au+Au collisions and compared to the previous results from the 1993 data set. They are very consistent. This establishes the quality of our analysis procedure. In the following section, we will use this procedure to construct the lambda spectra.

## 7.2 Lambda Yield and Spectra

Our approach is to present the experimental data on lambda production and compare the results with the thermal model and Relativistic Quantum Molecular Dynamics (RQMD) model [43], a dynamic hadronic model. The thermal model has been used to describe the overall behavior of the particle spectra produced in heavy-ion collisions. We will fit the measured lambda spectra using this model in order to characterize the data and to extract the Boltzmann temperature parameters. The comparison with the dynamic hadronic model can be used to learn if conventional physics is sufficient or if new physics is necessary to explain the experimental data.

In order to generate lambda spectra, the pair cuts described in section 6.4 are used to identify the  $\Lambda$ s. Due to the limited lambda statistics, the data are divided into constant  $p_t$  bins of 100 MeV and rapidity bins of 0.3 unit width from  $y = 2.2$  to  $y = 3.4$ . The lambda yield is obtained from the invariant mass distributions in each  $(y, p_t)$  bin after background subtraction as described in section 6.5. After corrections for acceptance and cut efficiency, the inclusive lambda spectra can be obtained by the same method used to generate the proton and pion spectra. Our  $\Lambda$  samples could contain a contribution from higher mass states having a  $\Lambda$  as their decay product that passes our cuts. The main source of these is  $\Sigma^0$  decay.

The lambda transverse mass spectra measured for the most central and semi-central Au+Au collisions are presented in Fig. 7.7 and Fig. 7.8, respectively. The error bars are not only statistical errors but also include the errors from the background subtraction. Overall, the spectra exhibit exponential thermal shapes with increasing inverse slope parameter when approaching mid-rapidity. The general behavior is well described by single exponential fits (solid lines). This is consistent with the fireball from where these  $\Lambda$ s originate to be in local thermal equilibrium.

The data are also compared to the RQMD v2.3 model run in cascade (dash his-

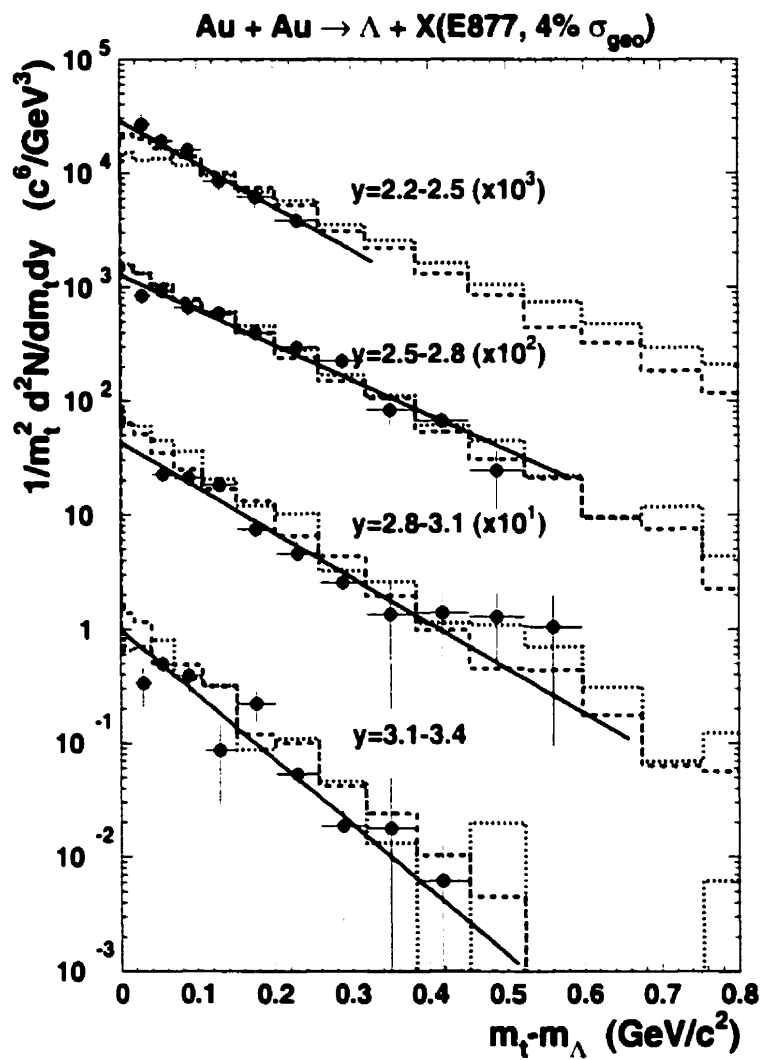


Figure 7.7: Measured  $\Lambda$  transverse mass spectra for the most central (4%  $\sigma_{geo}$ ) Au+Au collisions. The solid lines are the exponential Boltzmann fits. The dash lines and dot lines are the predictions of RQMD v2.3 model run in cascade and mean-field modes, respectively.

tograms) and mean-field (dot histograms) modes. As one can see, the conventional hadronic model reproduces the data very well both in magnitude and shape over the

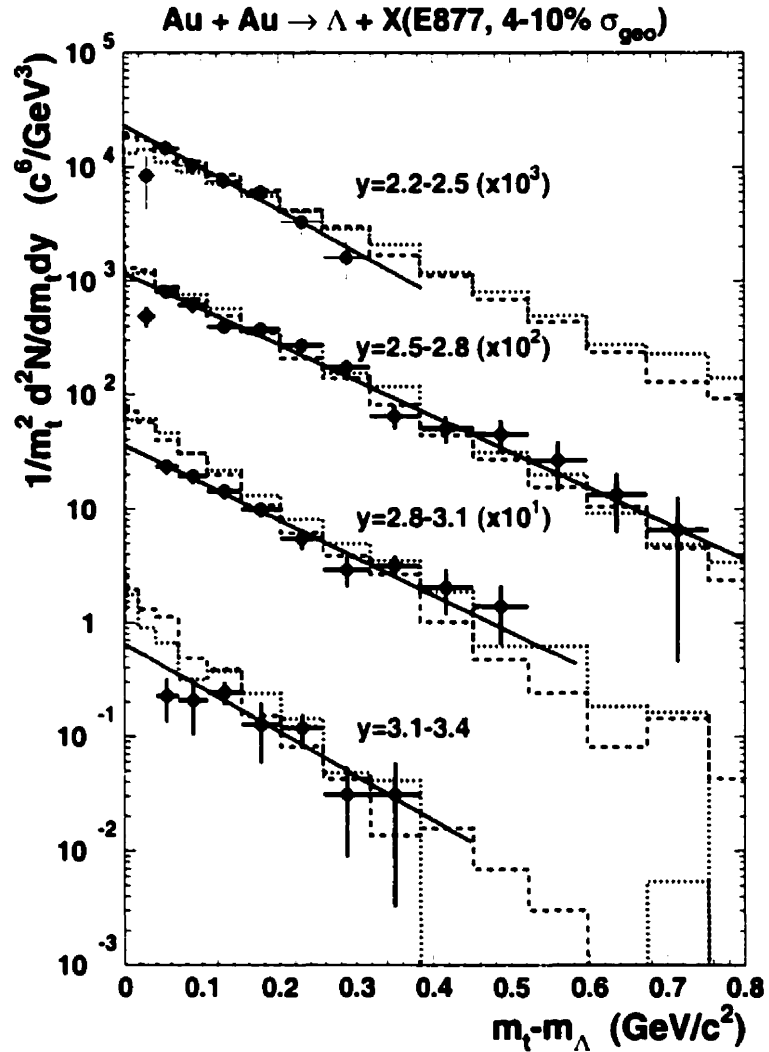


Figure 7.8: Measured  $\Lambda$  transverse mass spectra for the semi-central Au+Au collisions (4 – 10%  $\sigma_{geo}$ ). The solid lines are the exponential Boltzmann fits. The dash lines and dot lines are the predictions of RQMD v2.3 model run in cascade and mean-field modes, respectively.

measured rapidity and centrality intervals. In the forward rapidity region, there are little differences between the cascade predictions and the mean-field predictions in

the RQMD v2.3 model.

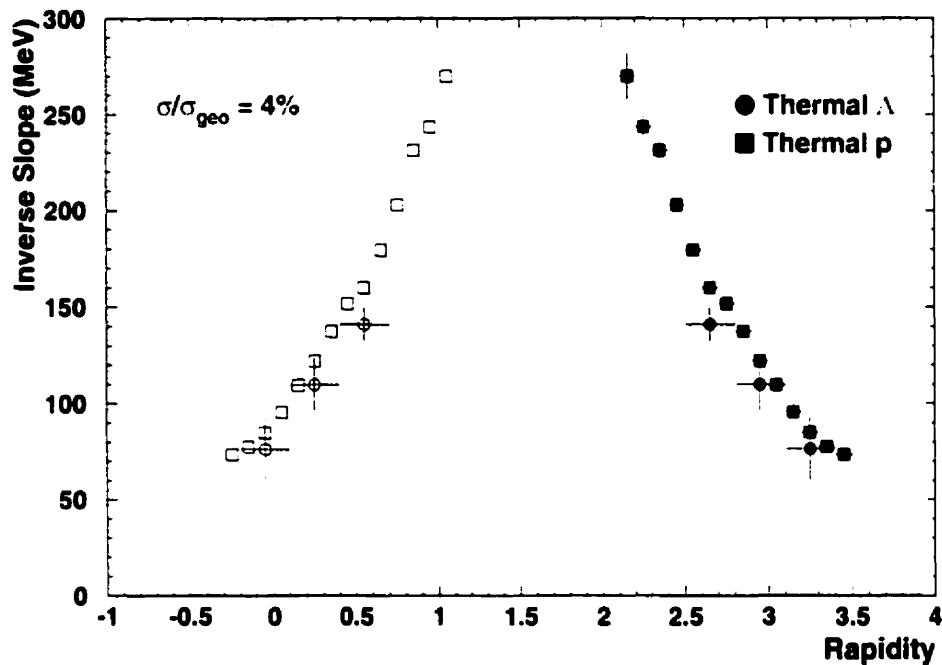


Figure 7.9: The inverse slope parameters as a function of rapidity in Au+Au collisions for 4% of  $\sigma_{geo}$ . The data are represented by solid symbols and reflected about mid-rapidity (open symbols). The proton data are extracted from the 1995 data set in Fig. 7.2.

The inverse slope parameters obtained from the exponential Boltzmann fits of the  $m_t$  spectra are presented in Fig. 7.9 for centrality 4% and Fig. 7.10 for centrality 4-10%. The data are compared to the values obtained from fitting the proton spectra. For both centrality bins, the extracted inverse slope parameters from the lambda spectra are similar, within the systematic errors, with the proton results in both amplitude and shape. This implies that like the protons the lambdas obtain a similar collective flow which is superimposed on the thermal motions in the freeze-out.

By integrating the transverse mass spectra where data are available and using the

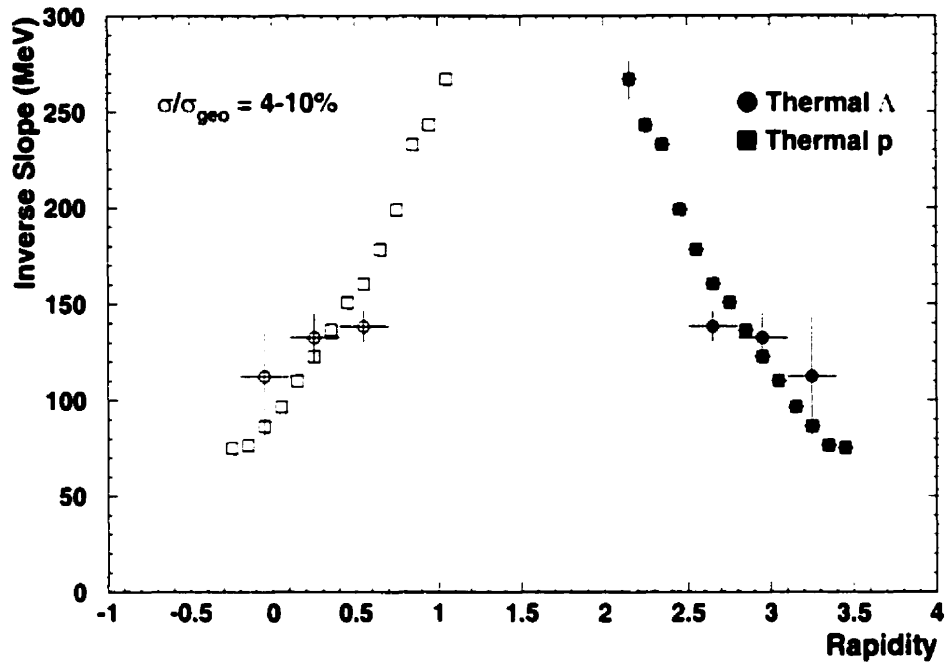


Figure 7.10: The inverse slope parameters as a function of rapidity in Au+Au collisions for  $4 - 10\% \sigma_{geo}$ . The data are represented by solid symbols and reflected about mid-rapidity (open symbols).

results from the Boltzmann fits to extrapolate to infinity, we obtain the  $\Lambda$  rapidity density distributions in the two centrality intervals, shown in Fig. 7.11 and Fig. 7.12. The data are also compared with the predictions of the RQMD model (histograms), where the dash histogram is the prediction of the model run in cascade mode while the dot histogram is the prediction of mean field mode. Our data are in very good agreement with the predictions of the model within the systematic errors. In the covered rapidity range ( $2.2 < y < 3.4$ ), the results from the calculations of both the pure cascade and the effects of mean-field included show a very little difference. The mean-field effects seem to have an effect only in the midrapidity range. Fig. 7.11

also includes the results from the E891 experiment [90] at the AGS. They reported a yield which is roughly 20% higher than ours. This difference is at the limit of the systematic errors of both experiment.

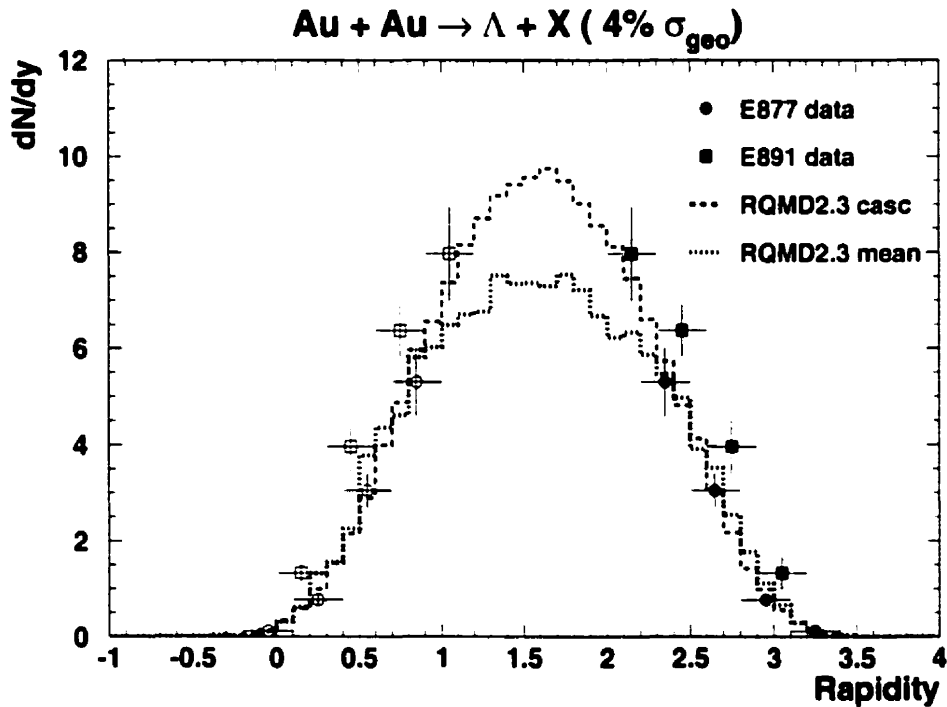


Figure 7.11: Lambda rapidity distribution in the most central Au+Au collisions (4% $\sigma_{geo}$ ). The data are represented by solid symbols and reflected about mid-rapidity (open symbols).

From the measured rapidity distributions of lambda and proton (listed in Appendix A), we calculated the ratio of  $\Lambda/p$ , shown in Table 7.1. The data are compared to the predictions of the RQMD model (v2.3) in the rapidity range ( $2.2 < y < 3.4$ ). The data are within errors consistent with the RQMD results. The agreement is, however, better with the pure cascade calculations.

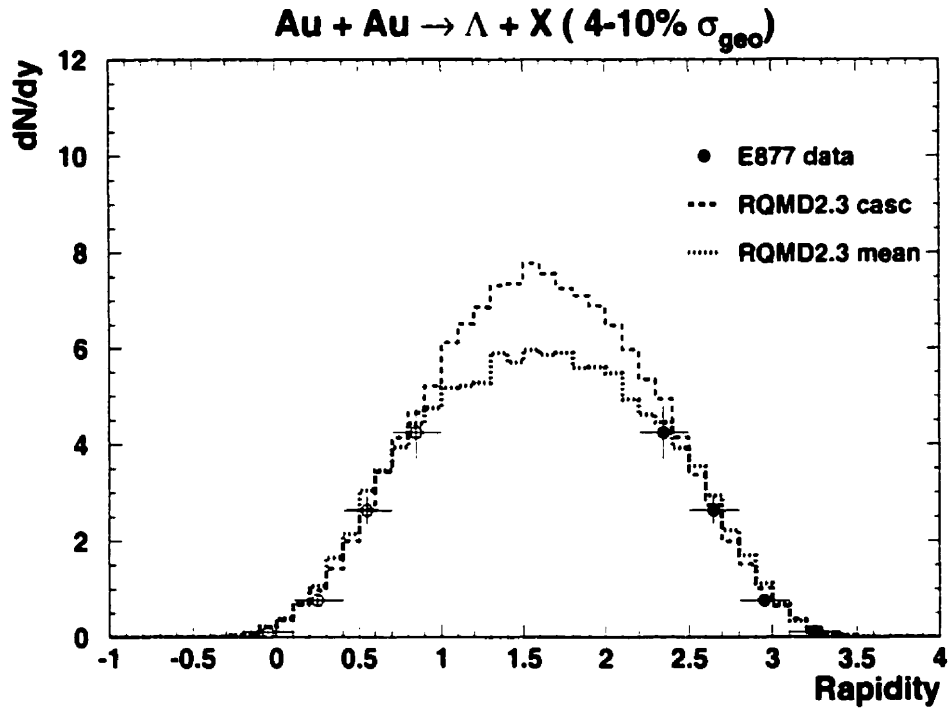


Figure 7.12: Lambda rapidity distribution in the semi-central Au+Au collisions ( $4 - 10\% \sigma_{geo}$ ). The data are presented by solid symbols and reflected about mid-rapidity (open symbols).

Table 7.1:  $\Lambda/p$  ratio in Au+Au collisions at 11.5 A-GeV/c. The data are compared with the predictions of the RQMD model (v2.3).

	Rapidity Range ( $2.2 < y < 3.4$ )	Centrality Bin	
		( $4 - 10\% \sigma_{geo}$ )	$< 4\% \sigma_{geo}$
$\Lambda/p$ ratio	Experimental data	$0.068 \pm 0.008$	$0.084 \pm 0.008$
	RQMD v2.3 Cascade	$0.064 \pm 0.006$	$0.077 \pm 0.006$
	RQMD v2.3 Mean-field	$0.057 \pm 0.007$	$0.069 \pm 0.007$

## 7.3 Lambda Directed Flow

The directed flows of proton and pion in Au+Au collisions at the AGS have been systematically studied by the E877 collaboration [21, 42, 84] using the Fourier expansion method. In this section we will attempt to extend the E877 flow studies to the lambda hyperons.

At lower energies ( $<2$  A·GeV), the theoretical studies [45] indicate that the directed flow of lambda hyperons is very sensitive to the  $\Lambda$  potential in dense nuclear matter formed in heavy-ion collisions. The calculations also shows that the primordial lambda hyperons have a weak flow as compared with the nucleon flow. The final-state interaction, especially the propagation in mean-field potential, enhances the lambda flow in the direction of nucleons and brings theoretical results in good agreement with the experimental data from both FOPI [47] and EOS [46] collaborations. We expect our data on lambda flow to provide more information for these questions.

### 7.3.1 Experimental Results

Due to the limited statistics of the  $\Lambda$  samples, we have to justify the analysis method in the study of lambda directed flow. First we look into the azimuthal angular distribution with respect to the reaction plane to extract the average directed flow parameter  $v_1$  over the full accepted  $p_t$  ranges with different rapidity and centrality windows. Then we attempt to study the  $p_t$  dependence of  $v_1$  as a function of rapidity and centrality using the Fourier expansion method as previously used in the analysis of proton and pion directed flow [21, 84].

We divide the azimuthal angle into six equal bins in the range from  $-180^\circ$  to  $180^\circ$ . In order to obtain the azimuthal angular distribution of lambdas, the lambda yields is extracted from the invariant mass distributions in each azimuthal angle bin

after background subtraction. The obtained azimuthal angular distribution of  $\Lambda$ 's with respect to the reaction plane are presented in Fig. 7.13.

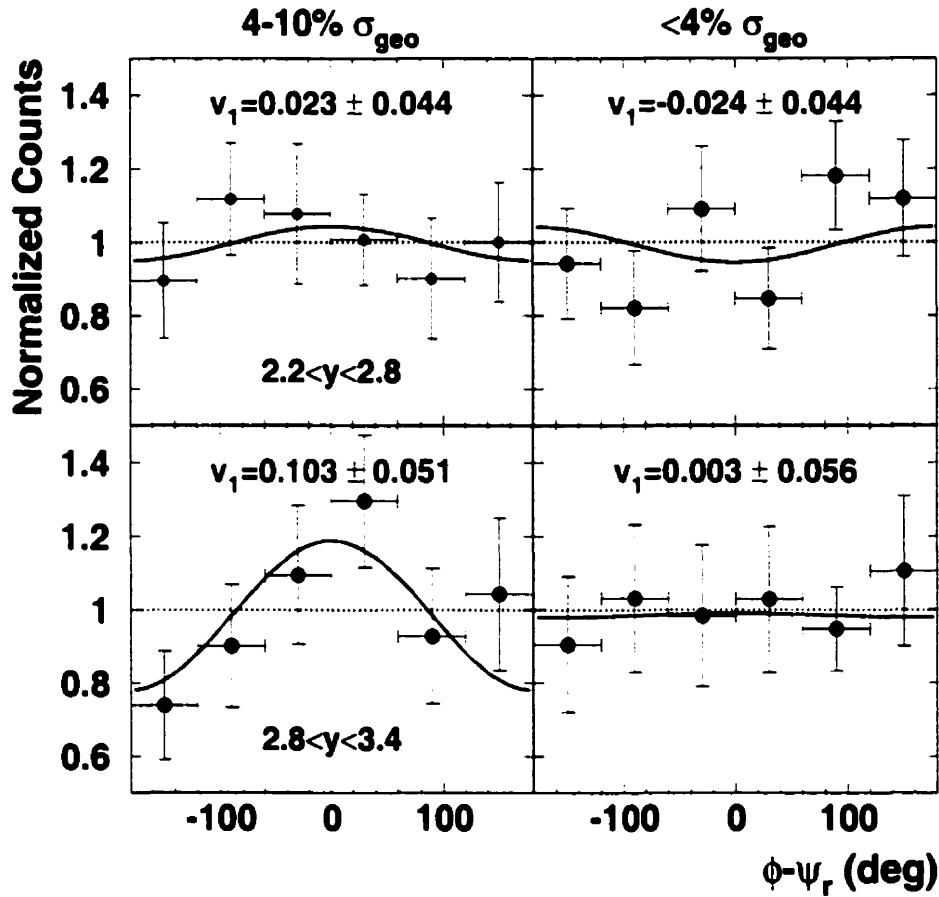


Figure 7.13: Lambda azimuthal angular distributions measured in transverse momentum range  $0.15 < p_t < 1.5$  GeV/c for different rapidity and centrality bins. The distributions are normalized to unity. The solid lines are the fits using Eq. 7.1. The obtained values of  $v_1$  are uncorrected for the reaction plane resolution.

Because of the limited statistics the errors are relatively large, however, one can see that the azimuthal angular distributions of lambda emission with respect to the reaction plane exhibit some azimuthal anisotropy. In the most central bin ( $< 4\% \sigma_{geo}$ ),

as can be expected there is no/or very little flow signal in the azimuthal distributions. But in the semi-central bin ( $4 - 10\% \sigma_{geo}$ ), flow signal shows up in the azimuthal distributions, and become significant when approaching the forward rapidities.

For an emission dominated by directed flow, the azimuthal emission distribution can be parameterized by

$$\frac{dN}{d\varphi} = 1 + 2v_1 \cos \varphi \quad \varphi = \phi - \psi_r \quad (7.1)$$

where  $\phi$  is the azimuthal angle of lambda emission in the lab frame and  $\psi_r$  is the reaction plane angle, which is determined as discussed in section 4.2.4. The parameter  $v_1$  quantifies the directed flow of particles parallel ( $v_1 > 0$ ) or antiparallel ( $v_1 < 0$ ) to the impact parameter vector. The fit by the above expression to the measured distribution yields the average  $v_1$  values (see figure). Note that the obtained  $v_1$  values are not corrected for the reaction plane resolution.

The  $p_t$  dependence of  $v_1$  is presented in Fig. 7.14. Once more the data display very little directed flow for the most central collisions ( $< 4\% \sigma_{geo}$ ). Stronger signal for the semi-central collisions ( $4 - 10\% \sigma_{geo}$ ), especially in the forward rapidities ( $2.8 < y < 3.4$ ), is observed. This tendency is consistent with the results obtained from the inclusive azimuthal angular distributions.

Due to the limited data statistics, we cannot draw any definite conclusions about the  $p_t$  dependence of the flow signal. But we can still compare the present data on lambda flow with the more precise proton data and the predictions of the RQMD v2.3 model. By such comparisons, some qualitative conclusions can be drawn.

### 7.3.2 Comparison with Protons

Since nucleon is the major carrier of the flow signal and the directed flow of proton has been well studied, it is a very good reference to which other particle flow can be compared. In the E877 experiment the acceptance for  $\Lambda$  is very similar with that of

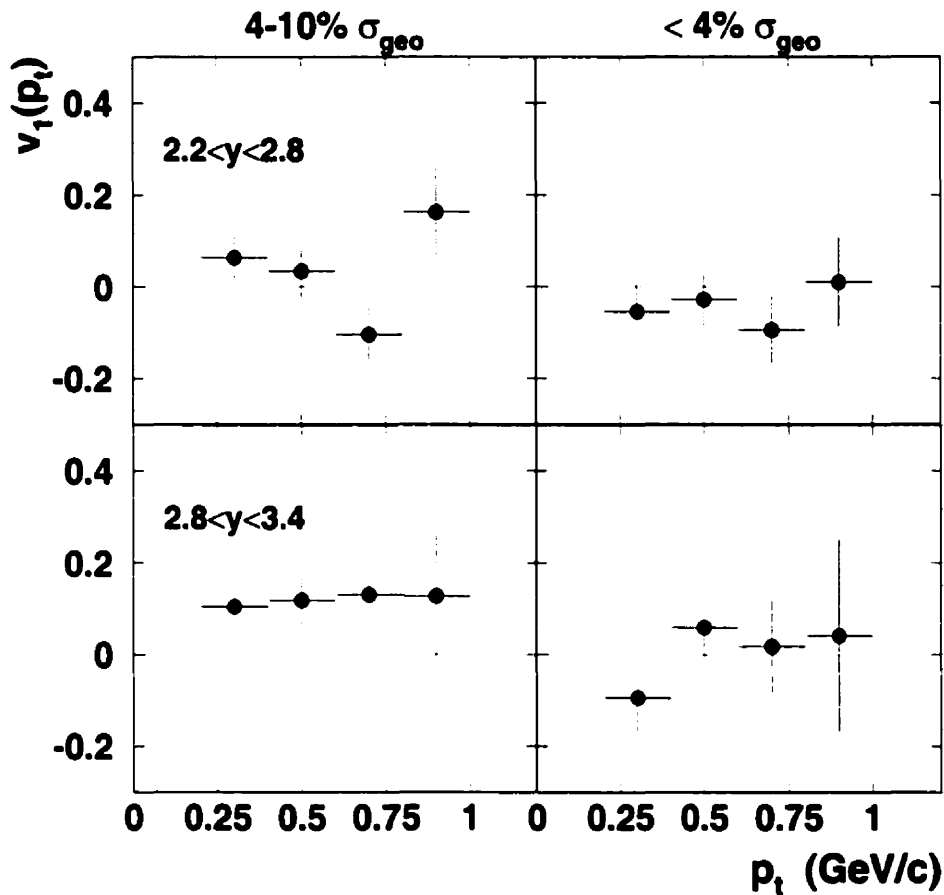


Figure 7.14: The  $p_t$  dependence of  $v_1$  of  $\Lambda$ 's in different rapidity and centrality bins.

the proton. This allows to make a direct comparison between them in discussing the directed flow of lambdas.

The azimuthal angular distribution for protons in the same acceptance range as the  $\Lambda$ s is presented in Fig. 7.15. The fits (solid lines) using the expression 7.1 are used to extract the average values of  $v_1$ . The obtained values of  $v_1$  for both lambda and proton are summarized in Table 7.2. Generally for the most central collisions ( $4\%\sigma_{geo}$ ) the obtained average values of the flow parameter  $v_1$  of  $\Lambda$  are somewhat smaller than that of protons. As the centrality decrease, the amplitude of the lambda directed

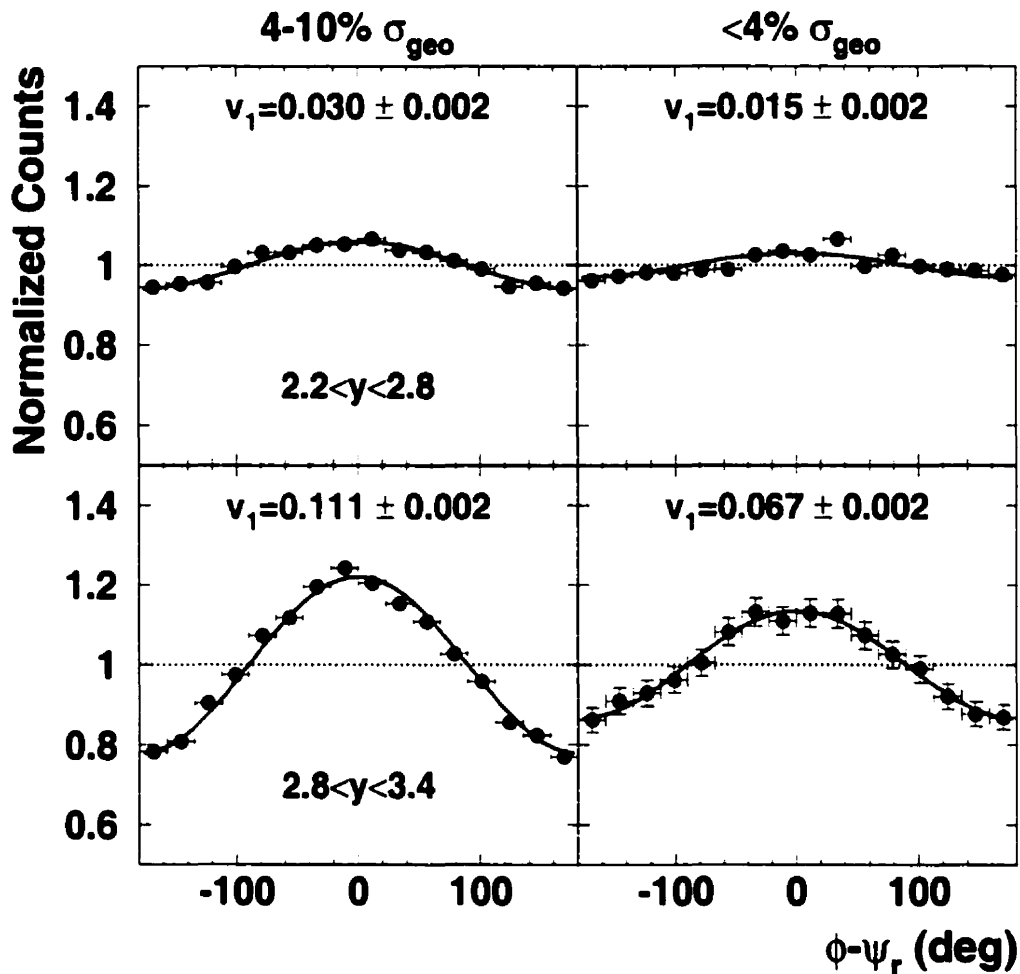


Figure 7.15: Proton azimuthal angular distributions measured in the same acceptance region as that of the  $\Lambda$ 's. The distributions are normalized to unity. The solid lines are the fits using Eq. 7.1. The obtained values of  $v_1$  are uncorrected for the reaction plane resolution.

flow becomes comparable to that of the protons.

The comparison of  $p_t$  dependence of  $v_1$  between lambda and proton is presented in Fig. 7.16. The large statistics uncertainties in the  $v_1(p_t)$ -dependence of  $\Lambda$  does not allow to draw any definite conclusions.

Table 7.2: Comparison of directed flow parameters  $v_1$  between  $\Lambda$ 's and protons for different rapidity centrality bins. The values of  $v_1$  shown in this table are taken from Fig. 7.13 and Fig. 7.15. The values corrected for the reaction plane resolution are also presented.

Centrality Bin		$(4 - 10\%)\sigma_{geo}$		$< 4\%\sigma_{geo}$	
Rapidity Bin		$2.2 < y < 2.8$	$2.8 < y < 3.4$	$2.2 < y < 2.8$	$2.8 < y < 3.4$
$\Lambda$	$v_1$ (uncorrected)	$0.023 \pm 0.044$	$0.103 \pm 0.051$	$-0.024 \pm 0.044$	$0.003 \pm 0.056$
	$v_1$ (corrected)	$0.031 \pm 0.058$	$0.137 \pm 0.068$	$-0.038 \pm 0.069$	$0.004 \pm 0.087$
$p$	$v_1$ (uncorrected)	$0.030 \pm 0.002$	$0.111 \pm 0.002$	$0.015 \pm 0.002$	$0.067 \pm 0.002$
	$v_1$ (corrected)	$0.040 \pm 0.003$	$0.148 \pm 0.003$	$0.023 \pm 0.003$	$0.105 \pm 0.003$

### 7.3.3 Comparison with RQMD prediction

The properties of hadrons may change when inside a dense nuclear medium. Baryons can acquire effective masses in the dense medium. In the RQMD model, the effect of mean-field is simulated by introducing Lorentz-invariant quasi-potentials [40]. The quasi-potentials generate additional pressure in the early stages of the collisions and therefore lead to an extra boost for the freeze-out particles in the transverse direction. So it is expected that the model will generate a stronger transverse flow for lambda when the mean-field effect is included.

At low energies (around 2 A-GeV), the theoretical calculations from the relativistic transport models (including the RQMD model) have indicated that the mean-field potentials play a major role in  $K^+$  and  $\Lambda$  flows [48, 91]. Without any final-state interaction, both  $K^+$  and  $\Lambda$  flow in the same direction as nucleons, but with much smaller flow amplitudes. The inclusion of their rescattering with the dense matter just enhances the flow of  $K^+$  and  $\Lambda$  a little in the direction of nucleons, as a results of thermalization effects. However, the propagations of  $K^+$  and  $\Lambda$  in their mean-field potentials lead to significantly different flow patterns for  $K^+$  and  $\Lambda$ . Kaons

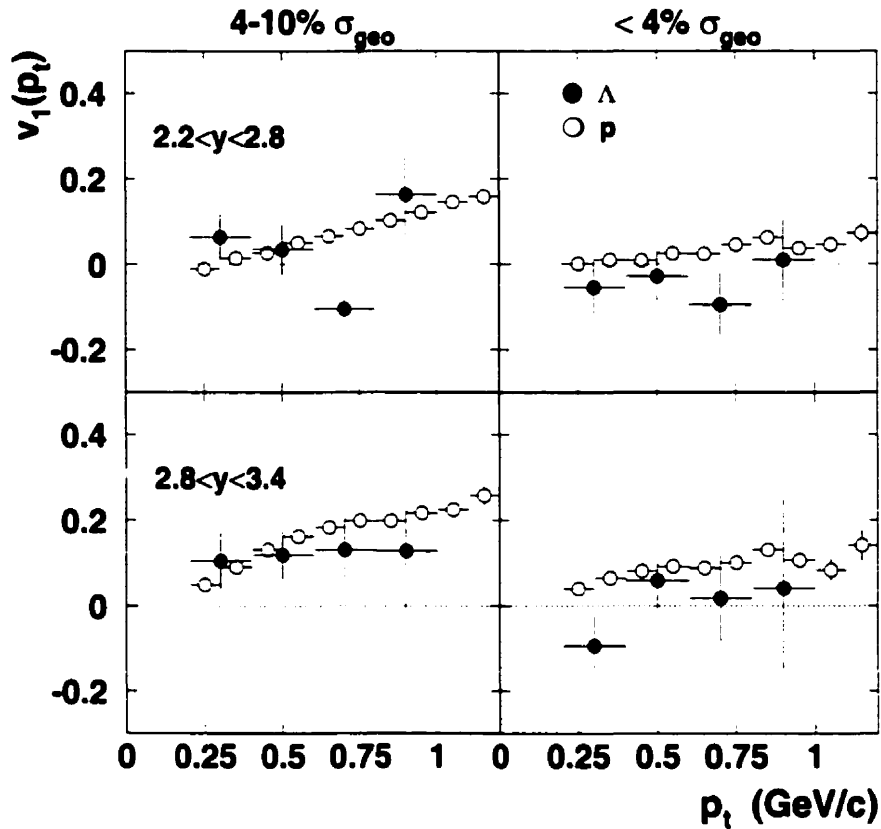


Figure 7.16: Comparison of  $v_1(p_t)$  data between  $\Lambda$ 's (solid circles) and protons (open circles).

are pushed away from nucleons by their repulsive potential while lambda hyperons are pulled towards nucleons by their attractive potentials. This leads to the small anti-flow of kaons with respect to nucleons, and to a flow of lambda hyperons very close to the flow of nucleons.

At the AGS, the predictions of RQMD model (v2.3) for proton and lambda directed flows in Au+Au collisions are shown in Fig. 7.17. For comparison, the proton flow is plotted on the upper panel as a reference. As shown in Fig. 2.9, the RQMD model (v2.3) describes well the data of proton flow if the effects of mean-field are

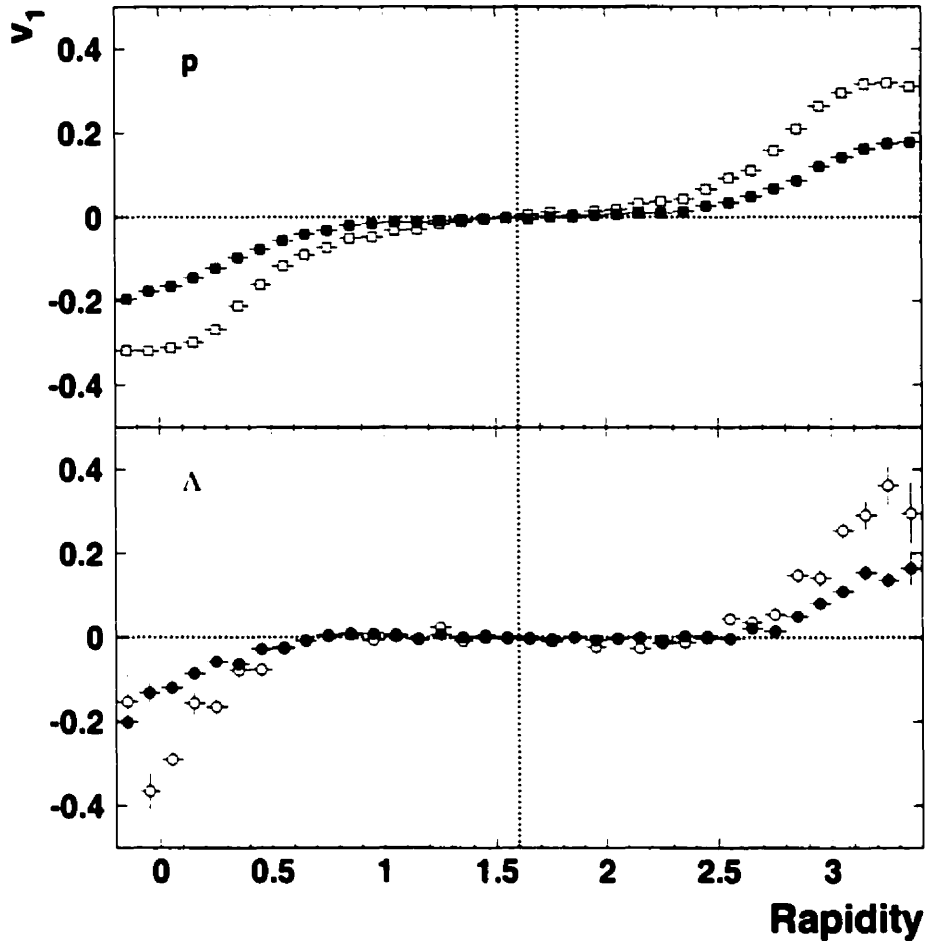


Figure 7.17: Proton and lambda directed flows in Au+Au collisions ( $b < 10$  fm) at 11.5 A-GeV/c as a function of rapidity predicted by the RQMD model (v2.3) run in cascade mode (solid symbols) and mean-field mode (open symbols).

included. In general, the RQMD model predicts that the lambda flow is very similar as the proton flow. Both cascade and mean-field modes predict that lambda has a very small flow at the mid-rapidities and that the flow become larger and comparable with the proton flow at  $y > 2.5$ . This is the region well covered in our experimental

measurements. A close inspection of the mid-rapidity region in Fig. 7.17, reveals that a very small anti-flow is actually predicted by the mean-field mode with a transition from negative to positive sign that occurs around  $y = 2.4$ .

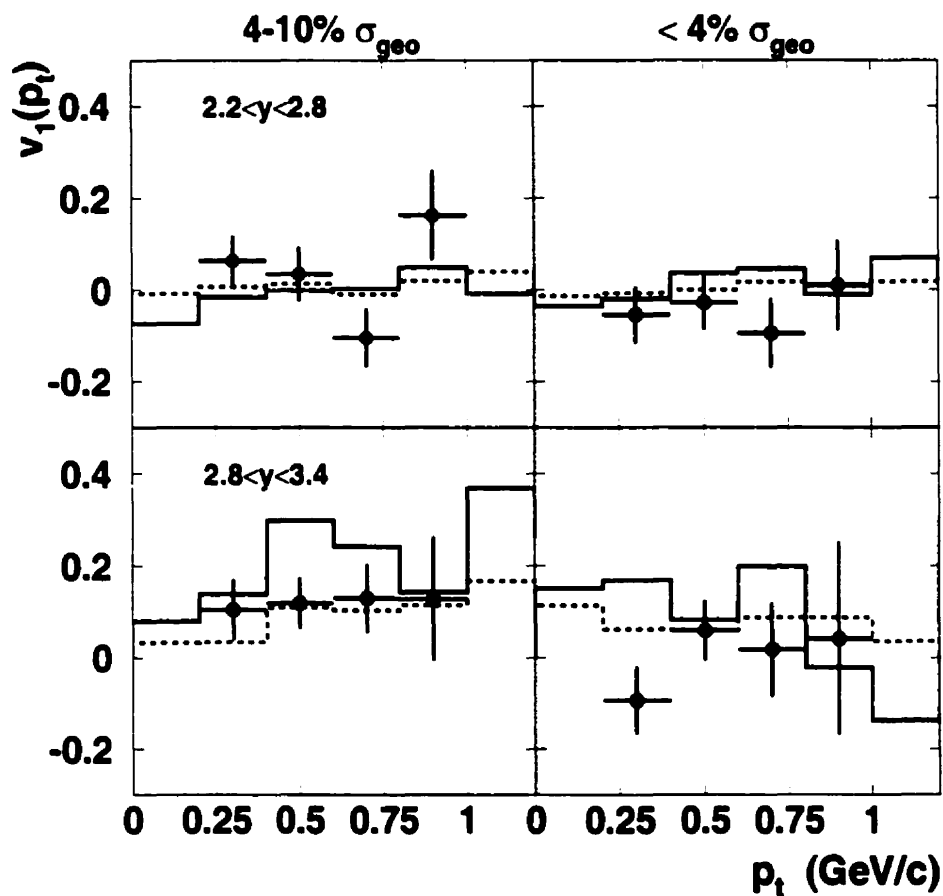


Figure 7.18: Comparison of  $\Lambda$  flow data (solid circles) with the predictions of the RQMD model (v2.3), run in cascade (dashed histogram) and mean-field (full histogram) modes.

The comparisons between the measured data and the predictions of the RQMD model in cascade and mean-field modes are presented in Fig. 7.18. Although the interpretation of the  $v_1(p_t)$ -dependence is limited due to low statistics, one can conclude that the measured  $p_t$  dependence of lambda directed flow is consistent with the

predictions of the RQMD model with the pure cascade calculations giving a better description on the data trend than the mean-field mode does.

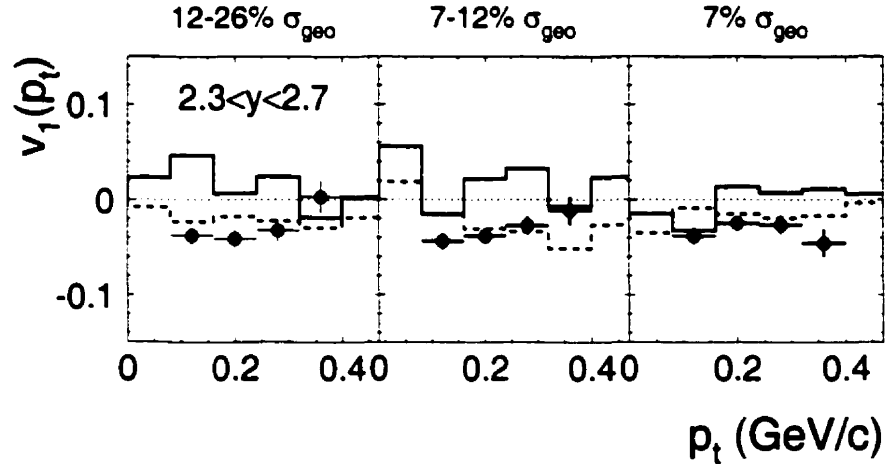


Figure 7.19: Comparison of  $K^+$  flow data with the predictions of the RQMD model (v2.3). The histograms are the predictions of the RQMD model run in cascade (dashed histogram) and mean-field (full histogram) modes. The figure is taken from [49].

A similar conclusion is reached from the recent results on  $K^+$  flow at the AGS [49]. Fig. 7.19 shows the comparison of  $K^+$  directed flow data with the predictions of the RQMD model (v2.3). In this case also the cascade calculations give a better description of the data than the mean-field. Since lambda production is mainly associated with kaon in hadronic scenario, the theoretical calculations indicate clearly a pivotal role of  $K^+$  and  $\Lambda$  medium effects in baryon-dense matter at lower energies ( $< 2$  A-GeV) [48]. Whether existing such effects at the AGS or even at higher energies, is still a question.

## Chapter 8

# Summary and Conclusions

The E877 experiment at the AGS of Brookhaven National Laboratory was dedicated to the study of the hadron production and flow pattern in Au+Au collisions at energies around 11 A-GeV. For the E877 last run in 1995, two identical multi-wire proportional chambers with highly segmented chevron pad readout were added upstream of the spectrometer magnet. They provided precise measurements of the coordinates of the track before it enters the magnetic field. This additional tracking information allowed to reconstruct the decay vertices of lambda hyperons. The improved experimental apparatus and large statistics accumulated during that run ( $\sim 45$  millions central events) allowed us to extend our previous measurements of hadron production and flow pattern to lambda hyperons.

Lambdas are measured via the charged decay channel:  $\Lambda \rightarrow p\pi^-$ . Due to the limited acceptance, the forward spectrometer is mainly sensitive to the  $\Lambda$ 's emitted at forward rapidities ( $y > 2.2$ ) and the overall geometrical detecting efficiency is in the order of  $10^{-3}$ . On the other hand, the abundant proton and pion produced in the Au+Au collisions result in a large combinatorial background. It is a great challenge to identify the low yield  $\Lambda$ s from such large background.

We have performed a comprehensive Monte Carlo kinematic simulation to study lambda reconstruction. The  $\Lambda$ s are generated according to the predictions of RQMD model (v2.3). The properties of lambda decay and of the E877 spectrometer are included in the simulation. By looking into the track properties of the correlated  $p\pi^-$  pairs from lambda decay versus the uncorrelated  $(p, \pi^-)$  pairs, five types of pair cut parameters are selected to reduce the dominant background and to help lambda identification. The corrections for the spectrometer acceptance with optimized pair cuts are also obtained in the kinematic simulation.

The assumption of tracks originating from the target in the low level track finding algorithm used in the analysis is not proper for the secondary tracks from lambda decay. This assumption led to wrong momenta being assigned to the secondary tracks. As a consequence, the mass spectrum of lambda is significantly distorted. We have developed a correction procedure, called "backtracking", to successfully solve this problem. It significantly improves the lambda identification.

Lambda identification is done from the invariant mass spectrum of the  $p\pi^-$  pairs by performing the five types of pair cuts on the pair analysis. The cut criteria have been optimized by the guidance of the Monte Carlo simulation. A linear interpolation around the lambda peak in the invariant mass distribution is used to subtract the background underneath the lambda peak. By this procedure we have obtained 2644  $\Lambda$ s from 31.918.757 central events ( $< 10\% \sigma_{geo}$ ).

The proton and pion spectra for most central collisions ( $< 4\% \sigma_{geo}$ ) are also constructed and analyzed. The results obtained are very consistent with the previous ones from the E877 1993 data set. These results are used to establish the quality of our analysis procedure in obtaining the lambda spectra.

The lambda spectra for the most central ( $< 4\% \sigma_{geo}$ ) and semi-central ( $(4 - 10\%) \sigma_{geo}$ ) collisions are obtained. The overall behavior of the transverse mass spectra is well described by a single exponential. The obtained inverse slope parameters from

the lambda transverse mass spectra are also well consistent with those obtained from the proton  $m_t$  spectra. This is consistent with a picture where the fireball from which the  $\Lambda$ s originate is in local thermal equilibrium.

We have clearly observed, for the first time at the AGS, a strong positive directed flow signal for lambda hyperons at the forward rapidities ( $2.8 < y < 3.4$ ) in the semi-central Au+Au collisions ( $4 - 10\% \sigma_{geo}$ ). The average flow amplitude for lambda hyperons is comparable with that of the protons in the same acceptance range. This result is consistent with the observations made at lower energies ( $< 2$  A·GeV), which show that the lambda flow follows the flow of nucleons. But the interpretation of our flow data for lambda hyperons is limited due to the low statistics.

All the measured results for lambda production in Au+Au collisions have been compared to the predictions of RQMD model (v2.3) in its pure cascade version and in the mode that takes into account the effects of mean-field. In the rapidity range covered, the model describes the data well. The measured transverse momentum dependence of the directed flow,  $v_1(p_t)$ , is also consistent with the predictions of the model with a somewhat better description being observed for the pure cascade calculations. This is consistent with the conclusions obtained from the  $K^+$  directed flow and confirms that lambda production is mainly associated with kaon in hadronic interactions. These data complete the study of the directed flow of the most abundant particles (proton, light nuclei, pions and kaons) produced in Au+Au collisions by the E877 experiment. This comprehensive set of data provides an important test bed for the theoretical models.

The narrow rapidity distributions for protons and lambdas indicate that a large stopping is reached in the central Au+Au collisions at the AGS. Whether the systems produced at the AGS have undergone a QGP phase transition is still an unsettled issue. The observed effects from the hadronic observables (proton, pion, kaon and lambda etc) are well explained by the conventional hadronic models. The quest for

the QGP has been passed to the experiments at RHIC. Hopefully the answer will come in the near future.

# Appendix A

## Data Tables

The following tables list the numerical values of the Boltzmann fit parameters and rapidity distributions for proton, pion and lambda at different centrality windows.

Table A.1: Boltzmann fit parameters for protons in the centrality interval  $\sigma_{\text{top}}/\sigma_{\text{geo}} = 4\%$ .

$$1/m_t^2 \cdot d^2N/dm_t dy = N_B/m_p \cdot \exp(-(m_t - m_p)/T_B(y)).$$

$y$	$N_B$ ( $c^4/\text{GeV}^2$ )	$T_B$ (MeV)	$dN/dy$
2.0 - 2.1	$135.51 \pm 1.40$	$240.25 \pm 11.84$	$50.69 \pm 3.50$
2.1 - 2.2	$135.85 \pm 1.33$	$269.90 \pm 12.08$	$60.38 \pm 3.90$
2.2 - 2.3	$138.97 \pm 1.10$	$243.38 \pm 6.19$	$52.92 \pm 2.32$
2.3 - 2.4	$142.17 \pm 0.94$	$231.11 \pm 3.80$	$50.28 \pm 2.18$
2.4 - 2.5	$148.55 \pm 0.81$	$202.71 \pm 1.71$	$43.58 \pm 2.34$
2.5 - 2.6	$152.49 \pm 0.69$	$179.56 \pm 0.85$	$37.94 \pm 2.60$
2.6 - 2.7	$155.81 \pm 0.43$	$159.87 \pm 0.39$	$33.33 \pm 2.57$
2.7 - 2.8	$147.97 \pm 0.43$	$151.80 \pm 0.38$	$29.14 \pm 2.18$
2.8 - 2.9	$140.68 \pm 0.61$	$137.35 \pm 0.42$	$24.37 \pm 1.57$
2.9 - 3.0	$133.50 \pm 1.12$	$121.91 \pm 0.53$	$19.83 \pm 1.57$
3.0 - 3.1	$119.45 \pm 1.16$	$109.38 \pm 0.56$	$15.60 \pm 1.27$
3.1 - 3.2	$103.95 \pm 1.30$	$95.59 \pm 0.64$	$11.89 \pm 0.73$
3.2 - 3.3	$77.02 \pm 1.35$	$84.90 \pm 0.81$	$7.68 \pm 0.57$
3.3 - 3.4	$49.38 \pm 1.43$	$77.38 \pm 1.24$	$4.53 \pm 0.52$
3.4 - 3.5	$24.95 \pm 1.82$	$73.42 \pm 3.25$	$2.17 \pm 0.27$

Table A.2: Boltzmann fit parameters for protons in the centrality interval  $\sigma_{\text{top}}/\sigma_{\text{geo}} = 4 - 10\%$ .  $1/m_t^2 \cdot d^2N/dm_t dy = N_B/m_p \cdot \exp(-(m_t - m_p)/T_B(y))$ .

$y$	$N_B$ ( $c^4/\text{GeV}^2$ )	$T_B$ (MeV)	$dN/dy$
2.0 - 2.1	$115.41 \pm 1.04$	$235.99 \pm 9.93$	$42.06 \pm 2.54$
2.1 - 2.2	$117.53 \pm 1.01$	$266.91 \pm 10.23$	$51.38 \pm 2.91$
2.2 - 2.3	$120.47 \pm 0.82$	$243.20 \pm 5.25$	$45.83 \pm 1.96$
2.3 - 2.4	$124.61 \pm 0.71$	$232.83 \pm 3.31$	$44.55 \pm 2.02$
2.4 - 2.5	$134.21 \pm 0.36$	$199.03 \pm 1.41$	$38.41 \pm 2.22$
2.5 - 2.6	$141.28 \pm 0.54$	$178.35 \pm 0.70$	$34.85 \pm 2.54$
2.6 - 2.7	$150.43 \pm 0.34$	$160.37 \pm 0.32$	$32.31 \pm 2.61$
2.7 - 2.8	$153.30 \pm 0.51$	$150.90 \pm 0.34$	$29.93 \pm 2.29$
2.8 - 2.9	$158.21 \pm 0.53$	$136.30 \pm 0.32$	$27.11 \pm 1.74$
2.9 - 3.0	$159.68 \pm 0.99$	$122.66 \pm 0.40$	$24.03 \pm 1.87$
3.0 - 3.1	$157.17 \pm 1.08$	$110.05 \pm 0.40$	$20.69 \pm 1.35$
3.1 - 3.2	$149.60 \pm 1.24$	$96.43 \pm 0.43$	$17.43 \pm 1.01$
3.2 - 3.3	$122.10 \pm 1.36$	$86.38 \pm 0.53$	$12.45 \pm 0.82$
3.3 - 3.4	$88.72 \pm 1.58$	$76.64 \pm 0.74$	$7.93 \pm 0.80$
3.4 - 3.5	$48.92 \pm 2.20$	$75.19 \pm 2.09$	$4.41 \pm 0.47$

Table A.3: Boltzmann fit parameters for positive pions in the centrality interval  $\sigma_{\text{top}}/\sigma_{\text{geo}} = 4\%$ .  $1/m_t^2 \cdot d^2N/dm_t dy = N_B/m_\pi \cdot \exp(-(m_t - m_\pi)/T_B(y))$ .

$y$	$N_B$ ( $c^4/\text{GeV}^2$ )	$T_B$ (MeV)	$dN/dy$
2.7 - 2.8	$862.30 \pm 35.79$	$75.90 \pm 1.05$	$24.35 \pm 1.09$
2.8 - 2.9	$289.39 \pm 12.01$	$109.87 \pm 1.35$	$21.53 \pm 1.24$
2.9 - 3.0	$288.00 \pm 12.62$	$103.65 \pm 1.42$	$18.55 \pm 1.10$
3.0 - 3.1	$255.67 \pm 13.86$	$100.80 \pm 1.76$	$15.76 \pm 0.97$
3.1 - 3.2	$223.05 \pm 4.07$	$98.41 \pm 0.61$	$13.34 \pm 0.85$
3.2 - 3.3	$197.37 \pm 6.47$	$94.80 \pm 1.01$	$10.87 \pm 0.71$
3.3 - 3.4	$217.89 \pm 32.88$	$85.54 \pm 4.07$	$9.17 \pm 0.60$
3.4 - 3.5	$184.17 \pm 10.08$	$82.91 \pm 1.43$	$7.27 \pm 0.49$
3.5 - 3.6	$310.76 \pm 2.97$	$61.56 \pm 0.34$	$6.20 \pm 0.39$
3.6 - 3.7	$262.45 \pm 2.64$	$58.22 \pm 0.33$	$4.75 \pm 0.35$
3.7 - 3.8	$209.24 \pm 2.45$	$56.25 \pm 0.40$	$3.60 \pm 0.28$
3.8 - 3.9	$182.17 \pm 2.31$	$50.70 \pm 0.40$	$2.63 \pm 0.23$
3.9 - 4.0	$142.88 \pm 2.26$	$48.35 \pm 0.52$	$1.92 \pm 0.20$
4.0 - 4.1	$119.32 \pm 2.38$	$43.77 \pm 0.66$	$1.38 \pm 0.13$
4.1 - 4.2	$97.41 \pm 2.49$	$38.13 \pm 0.81$	$0.92 \pm 0.10$
4.2 - 4.3	$73.72 \pm 2.45$	$35.60 \pm 0.97$	$0.64 \pm 0.08$
4.3 - 4.4	$63.09 \pm 2.19$	$29.03 \pm 0.75$	$0.40 \pm 0.05$
4.4 - 4.5	$47.50 \pm 2.27$	$24.73 \pm 1.34$	$0.26 \pm 0.04$
4.5 - 4.6	$34.96 \pm 2.76$	$28.22 \pm 5.43$	$0.22 \pm 0.04$

Table A.4: Boltzmann fit parameters for negative pions in the centrality interval  $\sigma_{\text{top}}/\sigma_{\text{geo}} = 4\%$ .  $1/m_t^2 \cdot d^2 N/dm_t dy = N_B/m_\pi \cdot \exp(-(m_t - m_\pi)/T_B(y))$ .

$y$	$N_B$ ( $c^4/\text{GeV}^2$ )	$T_B$ (MeV)	$dN/dy$
2.9 - 3.0	$291.63 \pm 12.58$	$100.33 \pm 1.15$	$24.53 \pm 2.09$
3.0 - 3.1	$338.20 \pm 15.18$	$92.25 \pm 1.16$	$21.80 \pm 2.03$
3.1 - 3.2	$271.25 \pm 16.19$	$88.83 \pm 1.47$	$17.51 \pm 1.72$
3.2 - 3.3	$245.14 \pm 15.90$	$83.86 \pm 1.47$	$14.25 \pm 1.58$
3.3 - 3.4	$250.84 \pm 18.05$	$78.07 \pm 1.48$	$11.61 \pm 1.37$
3.4 - 3.5	$178.49 \pm 18.41$	$76.17 \pm 2.04$	$8.91 \pm 1.15$
3.5 - 3.6	$179.88 \pm 36.42$	$69.08 \pm 3.52$	$6.89 \pm 0.97$
3.6 - 3.7	$173.47 \pm 43.11$	$63.90 \pm 3.85$	$5.18 \pm 0.79$
3.7 - 3.8	$111.64 \pm 37.42$	$59.86 \pm 4.83$	$3.67 \pm 0.63$
3.8 - 3.9	$94.63 \pm 7.61$	$58.03 \pm 1.19$	$2.90 \pm 0.54$
3.9 - 4.0	$98.21 \pm 47.91$	$51.47 \pm 5.73$	$2.04 \pm 0.42$
4.0 - 4.1	$91.03 \pm 64.82$	$43.82 \pm 6.38$	$1.31 \pm 0.31$
4.1 - 4.2	$112.48 \pm 1.21$	$35.81 \pm 0.28$	$0.92 \pm 0.25$
4.2 - 4.3	$78.04 \pm 1.02$	$34.00 \pm 0.32$	$0.59 \pm 0.18$
4.3 - 4.4	$52.06 \pm 0.84$	$31.50 \pm 0.38$	$0.36 \pm 0.12$
4.4 - 4.5	$33.43 \pm 0.69$	$29.29 \pm 0.47$	$0.21 \pm 0.08$
4.5 - 4.6	$20.35 \pm 0.55$	$28.89 \pm 0.67$	$0.13 \pm 0.06$

Table A.5: Boltzmann fit parameters for  $\Lambda$ 's in the centrality interval  $\sigma_{\text{top}}/\sigma_{\text{geo}} = 4\%$ .  
 $1/m_t^2 \cdot d^2N/dm_t dy = N_B/m_\Lambda \cdot \exp(-(m_t - m_\Lambda)/T_B(y))$ .

$y$	$N_B$ ( $c^4/\text{GeV}^2$ )	$T_B$ (MeV)	$dN/dy$
2.2 - 2.5	$32.11 \pm 5.79$	$115.14 \pm 18.51$	$5.30 \pm 0.72$
2.5 - 2.8	$14.42 \pm 1.32$	$141.09 \pm 8.81$	$3.05 \pm 0.36$
2.8 - 3.1	$4.80 \pm 0.87$	$109.79 \pm 13.86$	$0.77 \pm 0.11$
3.1 - 3.4	$1.10 \pm 0.39$	$76.32 \pm 16.62$	$0.12 \pm 0.02$

Table A.6: Boltzmann fit parameters for  $\Lambda$ 's in the centrality interval  $\sigma_{\text{top}}/\sigma_{\text{geo}} = 4 - 10\%$ .  
 $1/m_t^2 \cdot d^2N/dm_t dy = N_B/m_\Lambda \cdot \exp(-(m_t - m_\Lambda)/T_B(y))$ .

$y$	$N_B$ ( $c^4/\text{GeV}^2$ )	$T_B$ (MeV)	$dN/dy$
2.2 - 2.5	$25.81 \pm 4.98$	$117.14 \pm 17.20$	$4.24 \pm 0.56$
2.5 - 2.8	$12.98 \pm 1.28$	$139.44 \pm 8.23$	$2.64 \pm 0.30$
2.8 - 3.1	$4.00 \pm 0.54$	$132.47 \pm 13.00$	$0.77 \pm 0.10$
3.1 - 3.4	$0.72 \pm 0.34$	$112.44 \pm 32.22$	$0.11 \pm 0.02$

# Appendix B

## Reconstruction of $\Delta^{++}$

The low  $m_t$  enhancement of the measured pion transverse mass spectra in Au+Au collisions at the AGS could be mainly attributed to the decay of the  $\Delta(1232)$  resonance. To further test this hypothesis we attempt to reconstruct the  $\Delta^{++}$  via its decay products —  $p\pi^+$  pairs. A similar analysis on  $\Delta^{++}$  production in central Si+Pb collisions at 14.5 A-GeV/c was done in the E814 experiment [89], where a very low statistics on  $\Delta^{++}$  yield was obtained. The E877 1995 data have about 45 million central events, it is expected to obtain much higher statistics on  $\Delta^{++}$  yield.

$\Delta^{++}$  is the most easily measured one of all  $\Delta$  decays. There is no interference from the nearby lambda decay, which could disturb  $\Delta^0$  measurements. The interference from the HBT correlated pairs is very small since the correlated  $p\pi^+$  pairs have a negative sign due to Coulomb repulsive interaction. On the other hand, the charge asymmetry of the E877 spectrometer acceptance make it best suited for like-sign pair measurements.

The invariant mass ( $M_{inv}$ ) for  $p\pi^+$  pairs was reconstructed for central collisions ( $10\%\sigma_{geo}$ ). Single proton and  $\pi^+$  tracks were selected by the standard PID cut ( $1.5\sigma_{m^2}$ ). The maximum momentum cuts are 15 GeV/c for proton and 8.0 GeV/c

for  $\pi^+$ . Fig. B.1 shows a summary of our measurement of the  $\Delta^{++}$  using  $p\pi^+$  pairs. The analysis employs the “mixed events” technique. One determines the shape of the

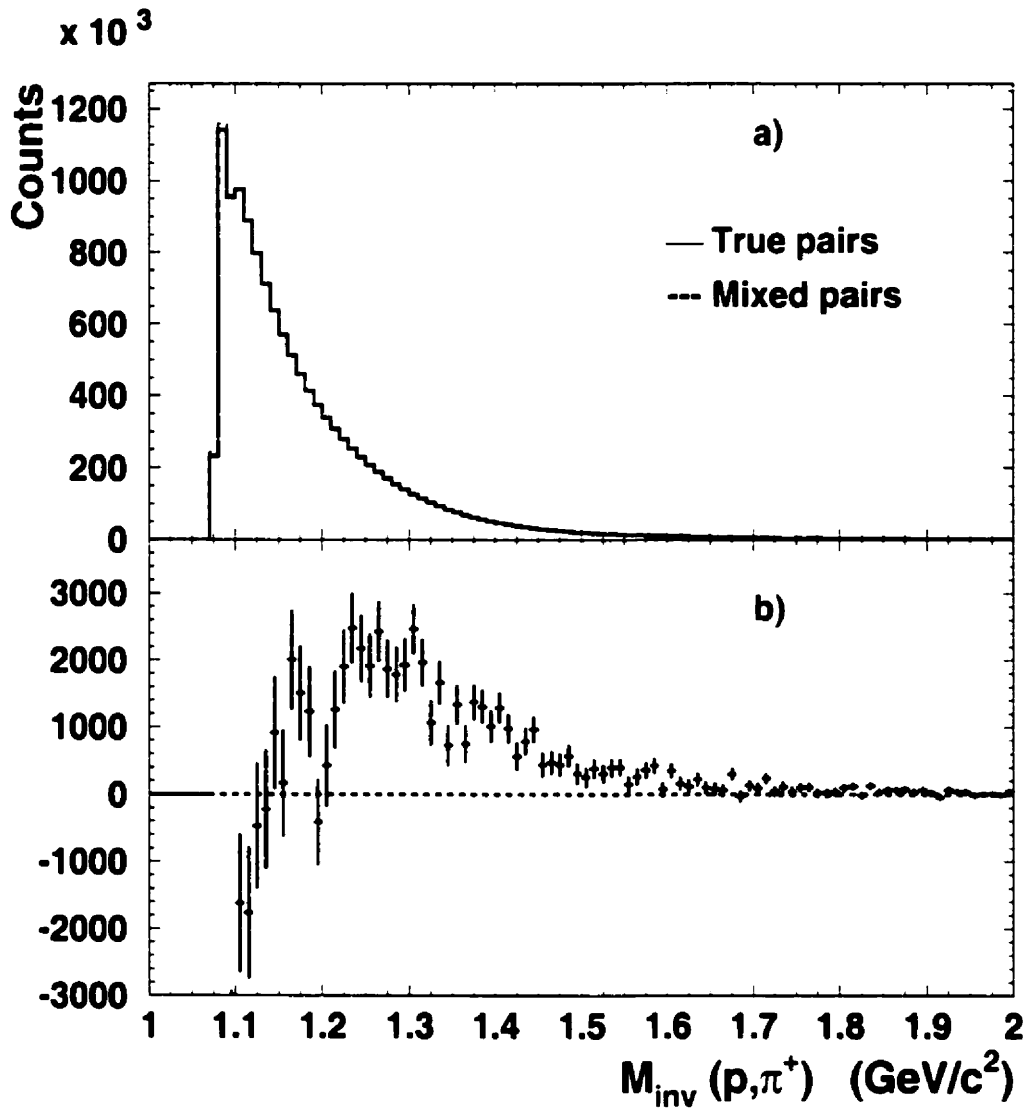


Figure B.1: Reconstruction of the  $\Delta^{++}$  resonance. a) The invariant mass spectra of  $p\pi^+$  pairs from the same event (solid histogram) and of  $p\pi^+$  pairs from mixed events (dashed histogram); b) The  $\Delta^{++}$  signal after subtracting the mixed pair spectrum from the true pair spectrum.

combinatorial background by constructing the invariant mass spectrum using protons and pions from different events. The resulting distribution is normalized to the true pair spectrum and subtraction yield the signal (see Fig. B.1(b)). The dip appearing around  $M_{inv} = 1.20 \text{ GeV}/c^2$  results from the effect of the “beam hole” in the proton and  $\pi^+$  acceptances because of the negative polarity of the magnetic field setting in the 95 data taking run. Integrating the spectrum, we obtain about 48,180  $\Delta^{++}$ s from the 18,040,331 central Au+Au events. With full 95 data statistics (45 millions central events), we can obtain roughly 100,000  $\Delta^{++}$ s. With such statistics it would be possible to do an analysis of  $\Delta^{++}$  production in the central Au+Au collisions.

# Bibliography

- [1] J. W. Harris. *Proceedings of Lake Louise Winter Institute: Quantum Chromodynamics, Lake Louise, Alberta, Canada, February 15-21, 1998.*
- [2] J. C. Collins and M. J. Perry, *Phys. Rev. Lett.* **34**, 1353 (1975).
- [3] L. P. Csernai. *Introduction to Relativistic Heavy Ion Collisions* , John Wiley & Sons. 1994.
- [4] T. D. Lee and G. C. Wick, *Phys. Rev.* **D9**, 2291 (1974);  
T. D. Lee, *Rev. Mod. Phys.* **47**, 267 (1975).
- [5] E. Shuryak, *The QCD Vacuum, hadrons and the superdense matter* , World Scientific, Singapore, 1988.
- [6] E. Laermann. *Nucl. Phys.* **A610**, 1c (1996).
- [7] C. Y. Wong, *Introduction to High-Energy Heavy-Ion Collisions* , World Scientific, Singapore, 1994.
- [8] B. Müller, *Rep. Prog. Phys.* **58**, 611 (1995); nucl-th/9410005.
- [9] J. W. Harris and B. Müller, *Ann. Rev. Nucl. Part. Sci.*, **46**, 71 (1996).
- [10] *Proceedings of the Quark Matter International Conferences on Ultra- Relativistic Nucleus-Nucleus Collisions:*

- Quark Matter '83, Nucl. Phys. **A418**, (1984).  
Quark Matter '86, Nucl. Phys. **A461**, (1987).  
Quark Matter '87, Z. Phys. **C38**, (1988).  
Quark Matter '88, Nucl. Phys. **A498**, (1989).  
Quark Matter '90, Nucl. Phys. **A525**, (1991).  
Quark Matter '91, Nucl. Phys. **A544**, (1992).  
Quark Matter '93, Nucl. Phys. **A566**, (1994).  
Quark Matter '95, Nucl. Phys. **A590**, (1995).  
Quark Matter '96, Nucl. Phys. **A610**, (1996).  
Quark Matter '97, Nucl. Phys. **A638**, (1998).  
Quark Matter '99, to be published in Nucl. Phys. A (1999).
- [11] M. C. Abreu *et al.*, NA50 Collaboration, Phys. Lett. **B450**, 456 (1999).
- [12] J. Barrette *et al.*, E814/E817 collaboration, Phys. Rev. Lett. **70**, 2996 (1993).
- [13] T. Alber *et al.*, NA49 collaboration, Phys. Rev. Lett. **75**, 3814 (1995).
- [14] L. Ahle *et al.*, the E866 collaboration, Phys. Rev. **C57**, R466 (1998);  
L. Ahle *et al.*, the E866 collaboration, Phys. Rev. **C57**, 1461 (1998);
- [15] H. Appelshauser *et al.*, NA49 collaboration, Phys. Rev. Lett. **82**, 2471 (1999);  
nucl-ex/9810014.
- [16] P. Braun-Munzinger, J. Stachel, J. Wessels and N. Xu, Phys. Lett. **B344**, 43  
(1995); Phys. Lett. **B365**, 1 (1996).
- [17] J. Stachel, Nucl. Phys. **A610**, 509c (1996).
- [18] J. Rafelski, Phys. Rep. **88**, 331 (1982);  
B. Muller, R. Koch and J. Rafelski, Phys. Rep. **142**, 167 (1986).

- [19] W. Reisdorf and H. G. Ritter, *Annu. Rev. Nucl. Sci.*, **47**, 663(1997).
- [20] Y. Zhang, PhD thesis, SUNY, Stony Brook, 1995.  
S. Voloshin and Y. Zhang, *Z. Phys.* **C70**, 665 (1996).
- [21] Y. Dai, PhD thesis, McGill University, 1998.
- [22] H. Filimonov, PhD thesis, McGill University, 1999.
- [23] H. R. Schmidt, J. Schukraft, *J. Phys. G: Nucl. Part. Phys.* **19**, 1705 (1993).
- [24] L. Landau, *Izvestia Akademii Nauk SSSR. Ser. Fiz.* **17**, 51 (1953).
- [25] J. Bjorken, *Phys. Rev.* **D27**, 140 (1983).
- [26] P. Braun-Munzinger *et al.*, nucl-ex/9803015.
- [27] R. Lacasse for the E877 Collaboration, *Nucl. Phys.*, **A610**, 153c (1996);
- [28] R. Lacasse, PhD thesis, McGill University, 1998.
- [29] J. Stachel, nucl-ex/9903007.
- [30] J. Barrette *et al.*, E877 collaboration, *Phys. Rev.*, **C50**, 3047 (1994).
- [31] T. Abbott *et al.*, E802 collaboration, *Phys. Rev.*, **C50**, 1024 (1994).
- [32] S. V. Afanasiev *et al.*, NA49 Collaboration, *Nucl. Phys.*, **A610**, 188c (1996);
- [33] G. D. Westfall *et al.*, *Phys. Rev. Lett.*, **37**, 1202 (1976);  
J. Gosset *et al.*, *Phys. Rev.*, **C18**, 844 (1978).
- [34] M. L. Lisa *et al.*, EOS Collaboration, *Phys. Rev. Lett.*, **75**, 2662(1995).
- [35] M. Petrovic *et al.*, FOPI Collaboration, *Phys. Rev. Lett.*, **74**, 5001(1995).

- [36] E. Schnedermann, J. Sollfrank and U. Heinz, Phys. Rev. **C48**, 2462 (1993);  
E. Schnedermann and U. Heinz, Phys. Rev. **C50**, 1675 (1993).
- [37] P. Danielewicz and G. Odyniec, Phys. Lett., **B157**, 146 (1985).
- [38] P. J. Siemens and J. O. Rasmussen, Phys. Rev. Lett., **42**, 880 (1979).
- [39] Nu Xu for the NA44 Collaboration, Nucl. Phys., **A610**, 175c (1996);  
I. G. Bearden *et al.*, NA44 collaboration, Phys. Rev. Lett., **78**, 2080 (1997).
- [40] H. Sorge, Phys. Rev. Lett. **78**, 2309 (1997);
- [41] P. Danielewicz *et al.*, Phys. Rev., **C38**, 120 (1988).
- [42] J. Barrette *et al.*, E877 collaboration, Phys. Rev., **C56**, 3254 (1997).
- [43] H. Sorge, Phys. Rev. **C52**, 3291 (1995);
- [44] G. Q. Li *et al.*, Phys. Rev. Lett. **74**, 235 (1995);  
G. Q. Li *et al.*, Nucl. Phys. **A594**, 460 (1995);
- [45] G. Q. Li and C. M. Ko, Phys. Rev. **C54**, 1897 (1996); nucl-th/9608049.
- [46] M. Justice *et al.*, EOS collaboration, Phys. Lett. **B440**, 12 (1998); nucl-ex/9708005.
- [47] J. L. Ritman *et al.*, FOPI collaboration, Z. Phys. **A352**, 355 (1995); nucl-ex/9506002.
- [48] G. Q. Li and G. E. Brown, Nucl. Phys. **A636**, 487 (1998);
- [49] J. Barrette for the E877 Collaboration. Quark Matter '99, to be published in Nucl. Phys. A (1999).

- [50] K. Filimonov for the E877 Collaboration, Quark Matter '99, to be published in Nucl. Phys. A (1999).
- [51] P. Braun-Munzinger *et al.*, nucl-th/9903010.
- [52] G. Odyniec. Nucl. Phys. **A638**, 135c (1998).
- [53] P. Senger and H. Strobele. nucl-ex/9810007.
- [54] P. Senger for the KaoS collaboration. nucl-ex/9901008.
- [55] L. Ahle *et al.*, E866 collaboration, Phys. Rev. **C58**, 3523 (1998):
- [56] C. A. Ogilvie for E802 and E917 collaborations, Nucl. Phys. **A630**, 571c (1998);  
C. A. Ogilvie for E866 and E917 collaborations, Nucl. Phys. **A638**, 57c (1998);  
nucl-ex/9802004.
- [57] R. Ganz *et al.*, E917 collaboration, J. Phys. **G25**, 247 (1999); nucl-ex/9808007.
- [58] P. Seyboth *et al.*, N49 collaboration, J. Phys. **G23**, 1787 (1997);
- [59] C. Bormann *et al.*, N49 collaboration, J. Phys. **G23**, 1817 (1997);
- [60] B. Hong, PhD thesis, SUNY, Stony Brook, 1995.
- [61] R. Lacasse *et al.*, Nucl. Instr. and Meth., **A408**, 408 (1998).
- [62] L. S. Waters, Ph.D. thesis, SUNY, Stony Brook, 1990.
- [63] J. Simon-Gillo *et al.*, Nucl. Instr. and Meth., **A309**, 427 (1991).
- [64] D. Fox *et al.*, Nucl. Instr. and Meth., **A317**, 474 (1992).
- [65] Z. Zhang *et al.*, Nucl. Instr. and Meth. **A343**, 610 (1994).
- [66] T. Vongpaseuth, PhD thesis, SUNY, Stony Brook, 1999.

- [67] W. J. Llope. PhD thesis. SUNY, Stony Brook, 1992.
- [68] M. Fatyga *et al.*. Nucl. Instr. and Meth., **A184**, 322 (1989).
- [69] R. Bersch, MSc thesis. SUNY, Stony Brook, 1995.
- [70] S. V. Greene *et al.*. Nucl. Phys. **A525**, 609c (1991).
- [71] W. E. Cleland *et al.*. E877 Note#PITT-95-002(February 8, 1995).
- [72] Upul Jayasiri Sonnadara. PhD thesis. University of Pittsburg, 1992.
- [73] James Dee. PhD thesis. SUNY, Stony Brook. 1995.
- [74] Timothy William Piazza. PhD thesis. SUNY at Stony Brook, 1997.
- [75] HBOOK Reference Manual. Version 4.21. CERN.
- [76] M. Pollack. PhD thesis. SUNY, Stony Brook, 1997.
- [77] Particle Data Group. Eur. Phys. J., **C3**, 1-794 (1998).
- [78] D. Miśkowiec. Momentum Resolution of the E877 Spectrometer - Calculation. 1996.
- [79] H. A. Bethe and J. Askin. in *Experimental Nuclear Physics*, edited by E. Segre (Jon Wiley & Sons. New York, 1953), Vol. 1.
- [80] K. Shigaki. Ph.D. thesis. University of Tokyo. 1995.
- [81] Y. Kwon. PhD thesis. SUNY, Stony Brook, 1997.
- [82] S. C. Johnson. PhD thesis. SUNY, Stony Brook, 1997.
- [83] S. Voloshin. Occupancy correction. E877 Note #HD-96/08/15 and #HD-96/08/27.

- [84] W. Chang, PhD thesis, SUNY, Stony Brook, 1997.
- [85] GEANT Detector Description and Simulation Tool , Version 3.2.1, CERN.
- [86] M. Justice, Nucl. Instr. and Meth., **A400**, 463 (1997).
- [87] J. Podolanski and R. Armenteros, Phil. Mag. **45**, 13 (1954).
- [88] D. H. Boal, C. K. Gelbke and B. K. Jennings, Rev. Mod. Phys. **62**, 553 (1990).
- [89] J. Barrette *et al.*, E877 collaboration, Phys. Lett., **B351**, 93 (1995).
- [90] S. Ahmad *et al.*, E891 collaboration. Phys. Lett., **B382**, 35 (1996);  
S. Ahmad *et al.*, E891 collaboration, Nucl. Phys., **A636**, 507 (1998);
- [91] Z. S. Wang *et al.*, Nucl. Phys., **A645**, 177 (1999).